Biomimetic emulsions to probe the mechanics of tissues

Iaroslava Golovkova

École doctorale 564 : Physique en Île de France

Thèse de Doctorat

présentée par

Iaroslava Golovkova

pour obtenir le grade de

Docteur de Sorbonne Université

Biomimetic emulsions to probe the mechanics of tissues

Thèse soutenue le 26/05/2021 devant le jury composé de :

Hélène Delanoë-Ayari	Rapportrice
Eric Weeks	Rapporteur
Olivia Du Roure	Examinatrice
René-Marc Mège	Examinateur
Laura Casanellas-Vilageliu	Examinatrice
Alexis Prevost	Directeur de thèse
Léa-Laetitia Pontani	Co-encadrante

Laboratoire Jean Perrin
UMR 8237 (SU/CNRS)
Institut de Biologie Paris-Seine
Sorbonne Université

Abstract

In my PhD work, I used tissue-mimetic systems to understand the physical basis of collective remodeling in biological tissues. In particular, I focused on the interplay between adhesion and mechanical forces and how it controls the emergence of tissue architecture during morphogenesis. Indeed, during morphogenesis, a cell aggregate is subjected to large successive elongations and folds that give rise to the highly organized 3D structures found in the embryo. To study the mechanical pathways of tissue remodeling, we used both an *in vitro* bottom-up approach, using a minimal set of ingredients to reproduce biomimetic tissues, and an *in vivo* study aiming at measuring forces inside developing tissues. In both cases, we used biomimetic emulsions that were shown to reproduce the minimal mechanical and adhesive properties of cells in biological tissues. These emulsions are stabilized with phospholipids and can be functionalized with binders to induce specific interactions between the droplets.

The first aspect of my project was to study the elasto-plastic behavior of adhesive emulsions under mechanical perturbations, by flowing them in microfluidic constrictions with controlled geometries. Adhesion between the droplets was introduced either through non-specific depletion forces, or through specific binding between biomimetic droplets. Image analysis allowed us to distinguish between an elastic response, in which the droplets deformed and kept their neighbors, and a plastic response, in which droplets rearranged their positions irreversibly. We found that while the presence of adhesion does not affect the global topology of rearrangements of the droplets, it slows down the local dynamics of individual rearrangements. As a result, droplets exhibit larger deformations and are globally aligned with the direction of tissue elongation. That could be the signature of an adhesion-induced polarization process in elongating tissues.

The second aspect of my project was done in collaboration with Marie Breau (LBD-IBPS). It consisted in using oil droplets as force sensors in developing zebrafish embryos. In particular, the injection of biocompatible oil droplets in their olfactory placode allowed us to measure the presence of anteroposterior compressive forces that can contribute to axone elongation of the olfactory neurons. Further studies will be conducted in order to obtain the full force map in the placode and decipher the origin of the forces driving axonal growth.

These complementary approaches both paved the way to a better understanding of the role of forces and adhesion during morphogenesis.

Résumé

J'utilise une approche biomimétique pour comprendre les mécanismes physiques qui sous-tendent le remodelage des tissus biologiques. J'étudie en particulier le rôle des interactions entre adhésion et forces mécaniques dans la morphogénèse, processus lors duquel les tissus sont soumis à des élongations et repliements successifs qui modèlent la forme des embryons. Ce sont ces aspects mécaniques que nous étudions par deux approches complémentaires *in vitro* et *in vivo* dans un cadre simplifié. En particulier, nous utilisons des émulsions biomimétiques constituées dont les propriétés mécaniques et adhésives miment celles des cellules d'un tissu. Ces émulsions biomimétiques sont stablisées par des phospholipides et peuvent être fonctionnalisées par des ligands spécifiques.

Le premier aspect de mon projet consiste à étudier in vitro le comportement mécanique de d'émulsions adhésives soumises à des perturbations mécaniques, en les injectant dans des constrictions microfluidiques de géométrie contrôlée. L'adhesion entre les gouttes est créée soit par des forces de déplétion non-specifiques, soit par des liens spécifiques mimant l'adhésion cellulaire. Par analyse d'image, nous différencions la réponses élastique, dans laquelle les gouttes se déforment à voisinage constant, de la réponse plastique, lors de laquelle les gouttes se réarrangent irréversiblement. Nous avons montré que la présence d'adhésion n'affectait pas la topologie globale des réarrangements, mais pouvait les ralentir localement. En conséquence, les gouttes présentent des déformations plus grandes et s'alignent avec la direction de l'élongation des tissus. Cela pourrait être la signature d'un processus de polarisation induit par l'adhésion dans les tissus en élongation.

Le second aspect de mon projet, en collaboration avec Marie Breau, consiste à utiliser des émulsions biocompatibles comme senseurs de forces in vivo. En particulier, nous avons injecté des gouttes la placode olfactive d'embryons de poissons zèbres pour mesurer les forces associées à l'élongation des axones dans ce tissu. Les résultats obtenus suggèrent la présence de forces compressives qui pourraient contribuer à la croissance axonale. Des études plus approfondies seront menées afin de conclure sur l'origine et rôle de ces forces dans le développement de la placode olfactive.

Les deux approches complémentaires utilisées pendant ma thèse permettent de lever le voile sur le rôle central des forces et de l'adhésion cellulaire dans la morphogénèse.

Acknowledgements - Remerciements

This part of my manuscript is as important for me as the scientific ones. It would be difficult to overestimate all the gratitude that I have for people that were near me during my PhD. Being aware of the limitations in space and language, I will try to express in the following the feelings that fill my heart.

First of all, I would like to express my deepest gratitude to my supervisors, Léa-Laetitia Pontani and Alexis Prevost. I could not have found better people to start my scientific career with! From the very beginning and every day during these almost 4 years I felt your support. You are wonderful scientific advisors, but you were much more for me than that. You always took care about me in my daily life as if I had been your daughter. No words can express the gratitude I feel for you! Thank you!

Next, I am thankful to Eric Weeks and Hélène Delanoë-Ayari for taking time to read and evaluate my manuscript. Thank you for your suggestions and positive feedback! I extend my gratitude to Olivia du Roure, René-Marc Mège and Laura Casanellas-Vilageliu for accepting the invitation to participate in my jury and for coming to Paris to attend my defence face-to-face.

I must thank Thibault Bertrand, Marie Breau, Girish Gangatharan and Pauline Monnot for the fruitful and interesting collaborations. Furthermore, I would like to thank Léa Pinon, Adèle Dramé-Maigné, Jacques Fattaccioli, Yannick Rondelez and Jasna Brujic for letting me use their equipment.

My doctoral school "Physique en Ile-de-France" financed my studies and stay in France during my PhD. I express my gratitude towards it as well.

A very special thank to CRI and my Master program. When I came there for Master 1, I knew absolutely nothing about research and how modern science works. During the two years spent in CRI, the whole scientific world had grown around me, and each day a new building-topic appeared from the fog. My dear teachers and classmates, thank you for these immense horizons!

Lorraine, Elie, Nicolas, Manon, Jean-Baptiste, Pierre - our MEBS team. My partners in crime! Thank you very much for working with me! Always supportive, in good mood - you were not my colleagues, but my friends.

I would like also to thank the PhD students in our lab, who were always here to help me. Tones of administrative work, complicated softwares, phone calls in French.. I wouldn't have done it without all of you!

The city, Paris, takes a special place in my heart. All its little streets and parks, incredible density of people and cars per square meter, luxurious "hôtels particuliers" and filthy alleys, delicious restaurants, museums, fabulous concerts and of course People. Thank you Paris for that unique atmosphere you were creating during these years!

And if I already started to speak about places, I would like to mention another one, which is very dear for me - our colocation! Thank you Sofia, Iris, Manon, Loïc, Polina, our chickens Brigitte and Bernadette and the cats Ali and Salem for all the moments we spent together! It was very cheerful life!

Many-many thanks to my awesome friends, in France and in Ukraine. Masha, Ellie, Valentin, Ania K., Chetan, Clovis, Matthieu P. and Matthieu G., Marina, Sasha Malyj, Katia V. and Katia

K., Alyona, Julie, Pierre, Yann, Georgiy, Yulia, Sasha V, Harley, Teja, Ella... It would not be enough place to list what I am thankful for. These years with you brought me a lot of unforgettable moments, that I appreciate so much!

I would like to thank my family, who means so much for me. My mom and dad, who inspire me and support whatever I do. My brothers and sisters - Sasha, Dasha, Iegor, Aliosha and Kyryl - you bring so many colors to my life! My two grandmas - Valia and Tata - all of that would not be possible without you. And of course all the other members of my huge family! Спасибо вам, семья! Дякую! Відчуваю вашу підтримку кожної миті! Знаю, що поки ви поруч, я можу все. І всі мої перемоги - ваші перемоги.

A special thanks to Sylvain. You were both my friend and family. Thank you for your support and your patience; for the world of classical music and mathematics. For dinners, when I was too lazy to cook. For the readiness to share any of my crazy ideas. Finally, for organising my buffet. :)

I would like to finish my acknowledgments by telling thank you to LJP. You are fantastic lab and fantastic people! Not a single day I was sad or desperate being in the lab. I'm so thankful for that!

List of Abbreviations

AFM	Atomic force microscopy
AP	Anteroposterior
CAM	Cell-adhesion molecules
CE	Convergent extension
CMC	Critical micellar concentration
DAH	Differential adhesion hypothesis
DSPE	1,2-distearoyl-*sn*-glycero-3-phosphoethanolamine
DMSO	Dimethyl sulfoxide
DPM	Deformable particle model
ECM	Extracellular matrix
EPC	Egg-L-α-phosphatidylcholine
HCP	Hexagonal close packing
hpf	Hours post fertilisation
LSCM	Laser scanning confocal microscopy
ML	Mediolateral
OB	Olfactory bulb
OE	Olfactory epithelium
OP	Olfactory placode
OSN	Olfactory sensory neurons
PC	Phosphatidylcholine
PDMS	Polydimethylsiloxane
PEG	Polyethylene glicol
PMMA	Poly(methyl methacrylate)
PSM	Presomitic mesoderm
RCP	Random close packing
SDCM	Spinning disk confocal microscopy
SDS	Sodium dodecyl sulfate
SM	Sphingomyelin
SPG	Shirasu Porus Glass

Contents

Introduction

Creation of a new life and its development from conception to birth have always been an alluring mystery to researchers. During the development, the cells of the embryo grow and divide multiple times. Cells that were initially almost identical thus differentiate into distinct tissues, through a complex shaping process called morphogenesis. This is the process that gives rise to various organs of different shapes and functions and allows the embryo to eventually develop into a fully formed organism. Certainly, such a complicated process requires a precise regulation and must avoid any detrimental mistake. Up to now, two main pathways have been considered as those governing the development of an embryo: biochemical and biomechanical pathways. While the first one has been widely studied, it has only been recently that scientists started to explore the mechanisms of the second pathway. One of the challenges that make it complicated to study the role of biomechanical pathways in morphogenesis, is the difficulty to disentangle the effects of mechanical and chemical signals.

This difficulty can be overcome by using soft matter analogues of biological tissues. Indeed, several studies have demonstrated that divided matter, such as foams or emulsions, allow to mimic certain mechanical properties of biological tissues. In this context, the use of biomimetic emulsions is particularly promising. These systems consist of adhesive oil droplets that were shown to reproduce the minimal mechanical and adhesive properties of both individual cells and tissues.

In my PhD work, I used such biomimetic emulsions to study the role of mechanical pathways during morphogenesis. In particular, we tackled this question through two complementary approaches: *in vitro* and *in vivo*. Our first approach aimed at revealing the role of adhesion in tissue remodeling processes under force (i.e. the global reorganization of tissues through which they acquire their final shapes). To this end, we applied mechanical perturbations on biomimetic emulsions and study their microscopic response as a function of interdroplet adhesion. With two different experimental systems, we probed the effect of both non-specific and specific adhesion. Our second approach consisted of studying the role of mechanical forces in the formation of the olfactory circuit in zebrafish embryos. This study was done in collaboration with Marie Breau and her team from Laboratoire de Biologie du Développement in Institut de Biologie Paris Seine. In a recent work she demonstrated that the formation of the olfactory system and, in particular, its region called the olfactory placode, is governed by mechanical forces exerted by the surrounding tissues. In order to map out these forces, we used oil droplets as biocompatible *in vivo* force sensors. To this end, we injected droplets into the placode of zebrafish embryos, and studied their

deformation resulting from the exerted forces.

This PhD manuscript is organized around 5 chapters.

Chapters 1 to 3 are dedicated to the *in vitro* approach that tackles the role of adhesion on the mechanical behavior of tissues during morphogenesis. In Chapter 1, I explain the basics of morphogenesis and describe biological tissues from a mechanical point of view. I finish the chapter by presenting Soft Matter models of biological tissues and, in particular, biomimetic emulsions.

In Chapter 2, I describe in detail the experimental methods that we used to study the behavior of biomimetic emulsions under mechanical perturbations.

Finally, in Chapter 3, I present two experimental systems that were developed during my PhD in order to study the role of adhesion in tissue remodeling processes. I explain in details the obtained results and link them to other findings reported in the field.

Chapter 4 is dedicated to the second axis of my work - mapping out the mechanical forces during the olfactory placode development in zebrafish embryos *in vivo*. Here, I briefly describe the state of the art related to the role of mechanical forces in the development of the olfactive system in zebrafish, and show our first results in mapping out the compressive forces generated during this process.

In Chapter 5, I summarize the work that was done during my PhD and describe the future developments of the projects. In addition, I present the preliminary results of a current study, in which we explore the role of adhesion on the structure of emulsions static packings.

Chapter 1

Morphogenesis and tissue remodelling

1.1 Cellular basis of morphogenesis

1.1.1 Morphogenesis in Nature

Tissue remodelling is the process of structural reorganization of living tissues. While tissue remodelling plays an important role in many physiological and pathological processes occurring in the organism, I will concentrate on its role in morphogenesis. During morphogenesis, tissues differentiate, deform, and move in an orchestrated manner to generate various organs with different shapes and functions. For example, during gastrulation, the Drosophila embryo folds onto itself to produce the ventral furrow that eventually becomes the first tubular shape of the embryo, thus defining the inside-outside geometry of the future organism [36] (Fig. 1.1). Another example of tissue remodelling is convergent extension (CE) [158]. This is the process by which the tissue of an embryo is restructured to converge (narrow) along one axis and extend (elongate) perpendicularly to this axis. This process involves collective migration of cells, as well as their rearrangements (intercalation). CE plays a crucial role in shaping the body plan during embryogenesis and is observed in both vertebrate and invertebrate embryos.

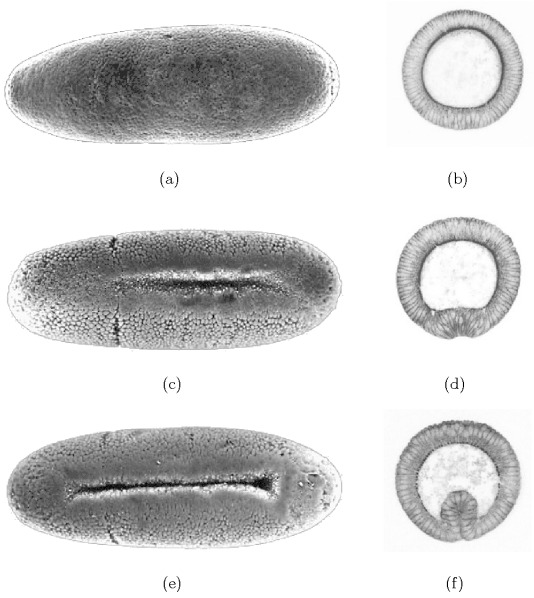

Figure 1.1 | **Example of tissue remodelling in nature.** Experimental images of ventral furrow invagination of the Drosophila embryo. The length of the embryo is around 500 μm. The ventral furrow is formed over a period of approximately 20 minutes, and appears as a shallow deepening hollow. Adapted from [35].

Tissue remodelling is controlled by both biochemical and biomechanical processes. On the one hand, it is controlled by secreted signaling molecules, which are called morphogens. Morphogens diffuse away from the sources of the secretion generating spatiotemporal concentration gradients. These gradients induce concentration-related biochemical responses and changes in gene expression in distant cells, thus driving tissue patterning [167, 118, 98]. On the other hand, tissue remodelling

is also controlled by forces generated within the cytoskeleton of the cells and transmitted across transmembrane receptors to neighboring cells and to the surrounding extracellular matrix [73, 38, 109, 174]. These forces induce mechanotransduction processes: mechanoreceptors on the surface of the cells are activated in response to the exerted forces, which provides regulatory signals within the cells (Fig. 1.2). These signals are equally as important as those conveyed by chemicals and genes [40, 48]. The force propagation in turn is enabled by the mechanical coupling between the cells, and thus depends on cellular adhesion. Therefore, the behavior of tissues during morphogenesis is strongly determined by the mechanical and adhesive properties of the cells [96, 49, 174, 17].

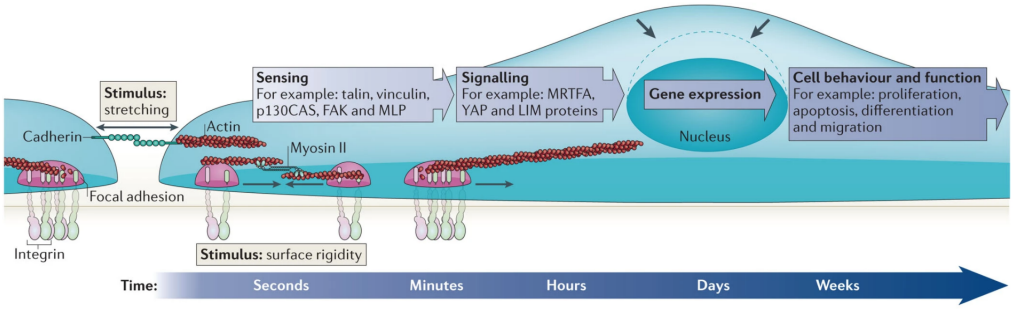

Figure 1.2 | **Mechanotransduction scheme.** Mechanotransduction converts mechanical stimuli — such as substrate rigidity, stretching or shear stress — into chemical signals to regulate cell behavior and function. Typically, the pathway involves receptors at focal adhesions or cell–cell contacts, mechanosensors and nuclear signalling factors to change gene and protein expression profiles. The timescale of these events ranges from milliseconds to seconds for the stretching of mechanosensors, hours for altered gene expression, days for changes in cell behavior and function, and weeks for tissue development. Adapted from [79].

1.1.2 Cellular basis of tissue remodelling

The cytoskeleton: a source of mechanical forces in cells

Mechanical properties of the cells and forces generated within the cells are controlled by their cytoskeleton. The cytoskeleton is a complex, dynamic network of interlinking protein filaments present in the cytoplasm of all cells. It is composed of three types of polymers: actin, microtubules and intermediate filaments.

Actin is the most abundant intracellular protein in most eukaryotic cells. It exists in two forms: as a globular monomer, called G-actin, and as a filament F-actin, which is a polymer of G-actin subunits with a diameter of about 8-9 nm. The formation of actin filaments is a treadmilling process: the filaments assemble at one edge and disassemble simultaneously at the other edge. In a cell, actin filaments are organized in bundles and networks, which are stabilized and crosslinked by different proteins. The filaments are constantly shrinking or growing in length, and their bundles and meshworks are continually forming and dissolving. Actin filaments usually interact with myosins, which are molecular motors that create internal stresses in actin networks. Changes

in the organization of actin filaments generate forces that modulate the shape of a cell and produce several types of cell movement.

Microtubules are polymers of globular tubulin subunits, which are arranged in cylindrical tubes measuring about 25 nm in diameter. Like the other filaments of the cytoskeleton, microtubules are highly organized inside a cell: they radiate from the centrosome, which is the primary microtubule-organizing center in animal cells. Together with actin, microtubules play an important role in cell migration during morphogenesis. In particular, they provide intracellular transport of signaling molecules and secretory vesicles and contribute to the generation of pushing forces [61]. The role of microtubules is also critical in moving chromosomes and the mitotic spindle during mitosis [120], as well as in enabling cellular motility through the beating of cilia and flagella.

Intermediate filaments are about 10 nm in diameter and are assembled from a large family of proteins. The composition of intermediate filaments depends on the type of tissue. Similarly to actin filaments, intermediate filaments are also organized in a network that stretches from the nuclear envelope to the plasma membrane. Together with actin filaments, they are usually attached to the plasma membrane and form a skeleton that helps supporting it. However, unlike actin and microtubules, intermediate filaments do not contribute to cell motility.

Such a complex organization of its cytoskeleton allows a cell to control its shape and mechanical properties. In particular, the elasticity of the cell is defined by a thin layer of actin called actin cortex (of width $\sim 200 - 500$ nm). It is located under the membrane of the cell and is responsible for a cortical tension, $\gamma_c \sim 10^{-3} N/m$, analogous to a surface tension in liquids [34]. Moreover, by regulating the cytoskeletal dynamics, a cell can generate forces, that then are transmitted to neighboring cells and the extracellular matrix. This allows a cell to mechanically interact with its surrounding environment and determines the global behavior of the whole tissue.

Cell-cell adhesion provides mechanical coupling between cells in tissues

Cells are connected to each other through specialized integral membrane proteins called cell-adhesion molecules (CAMs). Specifically, in soft tissues, cell-cell adhesion is mediated by proteins of the cadherin family [161, 128]. The cadherin family is subdivided into several subfamilies including the "classical" cadherins which are most widely expressed, particularly during the early development [68]. Each classical cadherin contains a single transmembrane domain, a relatively short intracellular domain, and five extracellular domains (Fig. 1.3). The formation of cell–cell adhesions entails two types of molecular interactions: lateral association of cadherins on the membrane of the cell and transversal binding of cadherins oligomers between two adjacent cells. These two types of interactions are called *cis* and *trans* interactions respectively. In this way, cadherins form clusters of a tight intercellular adhesion called adherence junctions [117], with the binding energy between two cadherins of $\approx 9 - 11kT$ [88]. The intracellular domain of cadherin is linked to the actin cytoskeleton by various adapter proteins, such as $\alpha-$ and $\beta-$catenins (Fig. 1.3). This interaction of cadherins with the cytoskeleton inside the cells actively regulates the strength of cell-cell adhesion [116, 161, 33].

Cadherins are essential to maintain cohesion in developing tissues [71]. In addition, these proteins have been shown to play a central role in diverse cellular processes, such as motility and signalling, tissue growth, cancer dissemination and development [149, 86, 159, 66]. For instance, the reorganization of tissues during morphogenesis is often accompanied by the conversion of nonmotile epithelial cells into motile precursor cells for other tissues (mesenchymal cells). Such epithelial-to-mesenchymal transitions are associated with a reduction in the expression of E-cadherin, the epithelial cadherin that is highly expressed in the early stages of development [68]. The conversion of the pigment-producing cells known as melanocytes into cancerous melanoma cells is also marked by a loss of E-cadherin activity [81]. The resulting decrease in cell–cell adhesion allows melanoma cells to invade the underlying tissue and spread throughout the body.

Apart from intercellular adhesion, cells in animal tissues also adhere indirectly through the binding of adhesion receptors in the plasma membrane, called integrins, to the surrounding extracellular matrix.

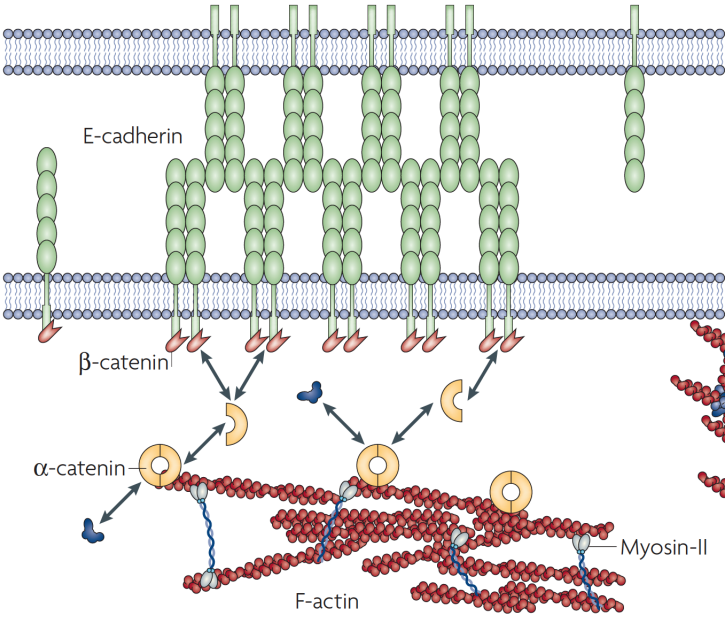

Figure 1.3 | **Molecular interplay between cortical tension and adhesion.** Intercellular adhesion is mediated by cadherin molecules (green). The intracellular domains of cadherins are bound to β-catenins (orange). Cadherin complexes are stabilized by cortical actin filaments (red) through α-catenin (yellow), which shuttles between β-catenin and F-actin. Adapted from [102].

The extracellular matrix

The extracellular matrix (ECM) is a non-cellular component which is present within all tissues. Its composition and topology are unique for each tissue and tailored to its functions [57]. However, three types of molecules are abundant in the ECM of all tissues:

- Fibrous proteins, which provide the mechanical strength and resilience of the ECM;

- Proteoglycans, a group of glycoproteins that cushion cells and bind a wide variety of extracellular molecules;
- Multiadhesive matrix proteins, which bind to and cross-link cell-surface adhesion receptors and other ECM components.

The main fibrous proteins of ECM are collagens, elastins, and laminins. These proteins are mainly synthesized by cells called fibroblasts, and once released, they assemble into long fibres forming different meshed structures. Fibre proteins are entangled and cross-linked with proteoglycans. Proteoglycans fill the majority of the extracellular interstitial space within the tissue in the form of a hydrated gel. The ECM is directly connected to the surface of the cells by proteins called fibronectin. Fibronectin molecules bind to the components of the ECM, particularly to fibrous collagens, and to the integrins, which are embedded in the plasma membrane of the cells.

Because of its connection to cells, the ECM serves several important functions. In particular, the ECM provides a lattice through or on which cells can move in the early stages of tissue assembly. It was also shown that cell-matrix adhesion participates in the mechanical coupling between the cells, which regulates the formation of muscle segments in the development of the zebrafish [162]. The matrix also serves as a reservoir for many extracellular signalling molecules that control cell growth and differentiation.

Therefore, cell–cell adhesion and cell–matrix adhesion, in combination with the mechanical properties of the cells, play a critical role during morphogenesis.

1.2 Mechanical properties of tissues

1.2.1 The concept of surface tension in biological tissues

The mechanical properties of tissues depend on those of the individual cells, but also on the adhesion energy between cells and between the cells and the extracellular matrix. When two cells are in contact, the size of their area of contact will be determined by the competition between the cortical tension and the intercellular adhesion (Fig.1.4). On the one hand, the membrane and the underlying cortical cytoskeletal components generate contractile forces, which tend to reduce the contact area. On the other hand, the E-cadherin mediated adhesion creates an adhesive force that tends to increase the contact area [80] and microscopically flatten the plasma membrane of the cells. This gives rise to an interfacial tension between the cells, that can be considered as analogous to a surface tension in liquids.

In liquids, surface tension drives surface minimization. As a result, a liquid droplet, such as an oil droplet in water, is spherical; with this shape, it minimizes its interfacial area and, therefore, minimizes its surface energy. Increasing the surface area of the drop requires an energy dE, which is proportional to the area increment $d\mathrm{S}$, such that $dE = \gamma d\mathrm{S}$, in which γ is the surface tension of

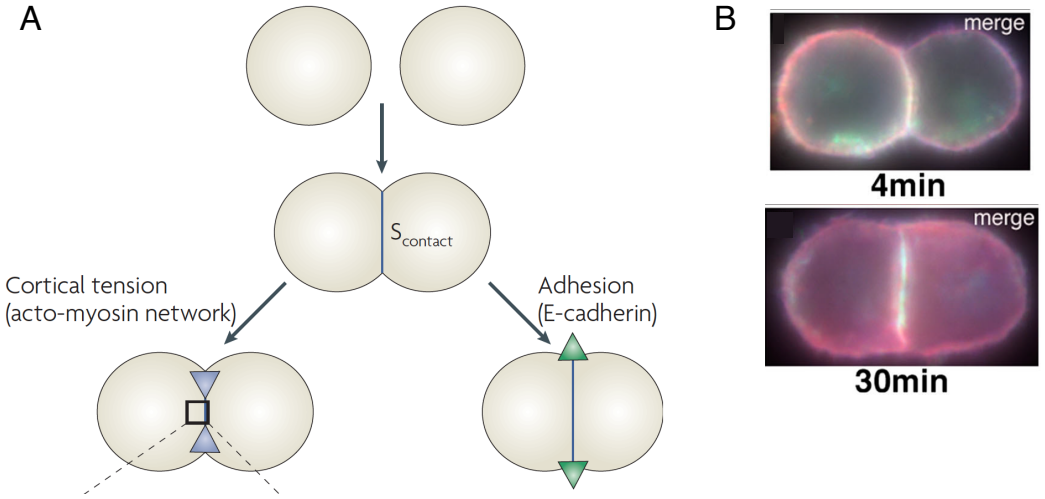

Figure 1.4 | **Control of cell shape by adhesion and cortical tension.** (A) When two single cells are brought into contact, the length of their surface of contact $S_{contact}$ changes according to intercellular surface tension. This surface tension results from the opposite effects of cortical tension that reduces the surface of contact, and of adhesion that increases the surface of contact. Adapted from [102]. (B) The evolution of contact area between two E-cadherin-expressing cells. Adapted from [33].

the liquid. In many regards, tissues behave similarly to fluids. Indeed, cells tend to aggregate in clusters in which the surface area of contact with the surrounding environment is minimized [151]. When two cell aggregates of the same cell line are brought into contact, they fuse to yield a larger, spherical aggregate thus minimizing the total surface energy (Fig. 1.5). Moreover, different cell populations mixed together can get sorted into two phases like immiscible fluids (Fig. 1.5). The first experiments capturing such behavior (the so-called "cell sorting experiments") were conducted by Holtfreter and coworkers [163]. In these experiments, they dissociated two different tissues into single cells and mixed them. Upon aggregation, cells sorted spontaneously into separate tissues like immiscible liquids. Holtfreter *et al.* suggested that the separation happened due to "affinity", a term used by Holtfreter in reference to analogous phase-separation phenomena in chemistry, the meaning of which in the context of tissues was not specified though.

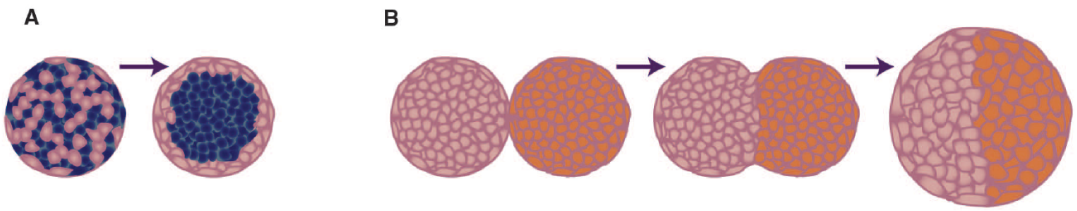

Figure 1.5 | **Wetting analogies of tissue behavior.** (A) Cell sorting. Two different cell populations (pink and blue) in a cell aggregate spontaneously sort out according to their surface and interfacial tensions. (B) Aggregate fusion. When brought into contact, two aggregates of the same cell line fuse to yield a larger spherical aggregate. Adapted from[64].

1.2.2 Tissues as fluids: the differential adhesive hypothesis as an attempt to explain cellular segregation

In order to explain the observed tissue segregation, Steinberg proposed the so-called differential adhesive hypothesis (DAH) [152]. His hypothesis proposes to consider tissues as liquids. In this framework, the DAH suggests that the final "equilibrium" configuration of segregated tissues minimizes the total surface energy and is guided by the surface tension of the tissues [55]. As a result, the tissues with higher surface tension will occupy the interior of the mixed aggregate, while the tissues with lower surface tension will be located on the surface of the aggregate. According to the DAH, the surface tension of tissues is generated from the intensity of adhesion between the cells in these tissues. Indeed, it was shown that surface tension increases linearly with the expression level of cadherin [56]. In an experiment on the role of cell adhesion in tissue surface tension, Foty and Steinberg measured the surface tension of aggregates of mouse fibroblast cells that expressed different levels of N-, P-, or E-cadherins. Independently of the cadherin type, tissue surface tension was found to be linearly proportional to the cadherin expression level. Moreover, cell sorting experiments with heterotypic aggregates of all combinations of the different cell lines systematically produced the cell organization predicted by DAH. Computational studies further confirmed DAH [62].

However, other studies of cellular segregation showed that the surface tension in tissues arises not only from the strength of adhesion between the cells, as previously described, but also from cell contractility. Krieg *et al.* [96] measured *in vitro* with atomic force microscopy (AFM) the adhesion level and cortical tension of individual cells of germ layers from gastrulating zebrafish embryos. During gastrulation, blastoderm cells rearrange to form the three primary germ layers: the ectoderm (outer layer), the mesoderm (middle layer), and the endoderm (inner layer). Krieg *et al.* found that the ectoderm cells showed significantly less cohesion compared to the other two layers, but higher cortical tension. Nevertheless, in cell sorting experiments *in vitro*, ectoderm cell clusters became surrounded by mesoderm or endoderm cells, and mesoderm cells where surrounded by endoderm cells. Such arrangements of the germ-layers correlated with their cortical tension levels, but not with their adhesion level. Shötz *et al.* performed direct measurements of the surface tension of the germ-layers and found that indeed the ectoderm had the highest surface tension, and the endoderm had the lowest [151].

These findings confirm the idea that cell aggregates tend to minimize their interfacial surface and, as liquids, sort according to their surface tension. However, tissue surface tension probably arises from the interplay between cell-cell adhesion and the cortical tension of the cytoskeleton [110, 153]. In agreement with this, Brodland and Chen proposed an interfacial tension hypothesis, where they took into account both the contribution of the mechanical properties of the cells and the level of adhesion between them [23]. This extended version of the DAH is now widely accepted.

1.2.3 Characterization of the mechanical properties of tissues

In order to be able to quantitatively describe tissues, their mechanical parameters, such as surface tension or elasticity, have to be measured. There are available techniques to measure some of the mechanical parameters on the single cell level, such as AFM to measure the cortical tension of a cell [97]. However, such measurements are usually done on time scales of seconds, while the relevant time scale for tissue reorganization is on the order of hours [64]. Therefore, it is important to measure the mechanical parameters at the tissue level. Different techniques were developed in order to characterize the mechanical properties of tissues [64, 157, 138, 144]. Some of them are summarized in Fig. 1.6 and are described below.

One of the first techniques proposed to measure tissue surface tension consisted in using cellular aggregate centrifugation [134]. When an aggregate is centrifuged for a sufficiently long time, it deforms and flattens. The level of deformation inversely correlates with the tissue surface tension. In addition, by following the evolution of the aggregate shape in the centrifugal field or its shape relaxation after centrifugation is stopped, this technique could in principle be used to evaluate the elastic modulus and viscosity of the tissue [64].

Parallel-plate compression, a technique proposed by Steinberg and co-workers [52, 53, 54] and further developed by [121], is one of the most widely used nowadays. In this method, an aggregate is compressed between two nonadhering parallel plates to a fixed deformation. The measurement of the evolution of the compression force as a function of time allows to measure the viscoelastic properties of the aggregate [111, 153], such as Young's modulus E, and dynamic viscosity η. The aggregate eventually reaches an equilibrium shape, analogous to the shape of a liquid drop compressed between two plates. Knowing the equilibrium shape of the aggregate and the corresponding applied force F, the aggregate surface tension can be obtained from the following equation:

$$\gamma = \left(\frac{1}{R_1} + \frac{1}{R_2}\right)^{-1} \frac{F}{\pi R_3^2} \tag{1.1}$$

where R_1, R_2 are the principal radii of curvature of the deformed aggregate and πR_3^2 is the contact area between the aggregate and either of the plates (Fig. 1.6) [53].

Another technique developed to characterize tissue rheology is micropipette aspiration [65]. In this method, an aggregate is aspirated at a constant suction pressure into a micropipette of smaller diameter than that of the aggregate, and the length of the aspirated tongue, $L(t)$, is tracked over time. After aspirating the aggregate for a long enough time to capture its long-term behavior, the pressure is released, causing the aggregate to retract out of the pipette under the action of its surface tension. This method allows to measure the aggregate's elastic modulus, its viscosity, and its surface tension by fitting the aspiration and retraction curves [65, 64].

Finally, the resistance of a tissue to stress-induced failure can be characterized by pulling apart partially fused aggregates at a constant speed and measuring the fracture energy that is needed to separate them [168].

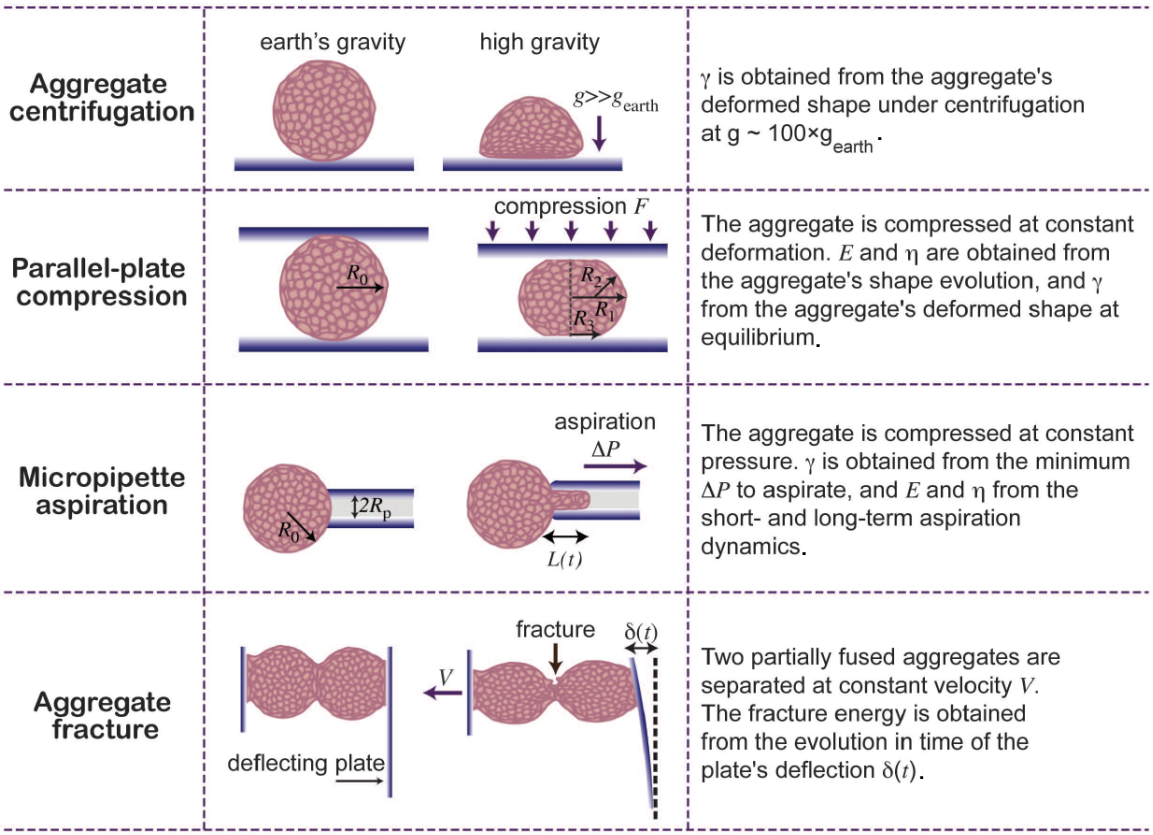

Figure 1.6 | **Experimental techniques used to quantify mechanical properties of model tissues.** Adapted from [64].

The described techniques allow to measure different mechanical parameters of biological tissues. However, the choice of the appropriate parameters depends on the physical model adopted to describe the tissue behavior. Indeed, multiple experimental studies showed that biological tissues can be described both as viscoelastic fluids and as an elasto-visco-plastic solid depending on the time scale [64]. As a matter of fact, it was shown that biological tissues can undergo a solid to liquid transition, which I am describing below.

1.2.4 "Liquid-solid" like phase transition of tissues

It was shown that the macroscopic response of biological tissues is viscoelastic: the tissue behaves as an elastic solid over short timescales and as a viscous fluid over long timescales [151]. Indeed, when cellular aggregates are compressed between parallel plates for a short time (seconds), the aggregate regains its shape right after the pressure is released. This is the behavior typical for elastic solid materials. However, if the compression is applied for a longer time (hours), the aggregate remains flat for several hours even in the absence of the compressive force. This last behavior could only take place if cells in the aggregate rearranged, thus dissipating the applied

stress, which is the typical behavior for liquids. Such change in the mechanical behavior of tissues ressembles solid-liquid transitions observed in inert granular materials. And similarly to granular materials, solid-like tissues possess a yield stress: tissues elastically resist a finite stress below the yield stress, but flow and remodel if the applied stress exceeds the yield stress.

Physical mechanisms for "liquid-solid" phase transition of tissues

The mechanisms that underlie and control such liquid to solid and solid to liquid transitions in tissues have been of great interest over the last decades. By analogy to similar transitions in inert soft matter, three main physical mechanisms were shown to drive "solidification" of tissues [100]: cellular jamming, tension-related rigidity and cellular motility. These mechanisms are summarized on a speculative cell jamming phase diagram, as depicted in Fig. 1.7, and described in details below.

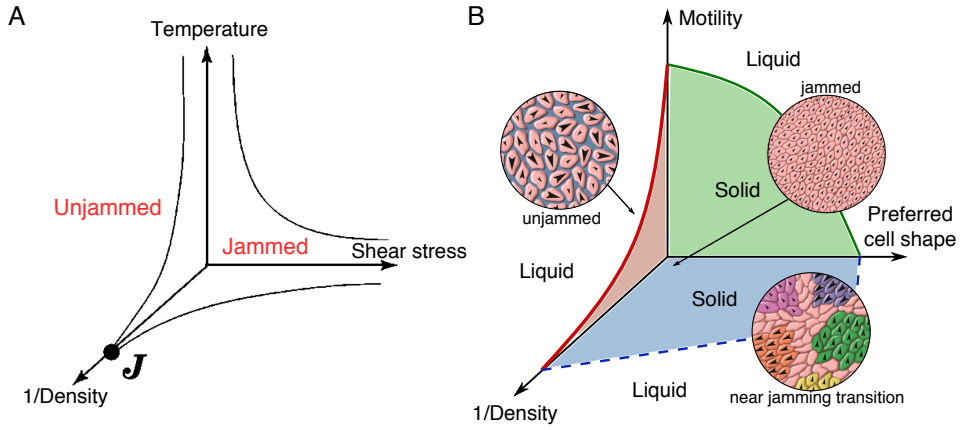

Figure 1.7 | **A speculative phase diagram for liquid-solid transitions in soft inert materials (A) and biological tissues (B).** Arrow-heads within the cell assemblies (disk regions, B) depict the migration speed and migration direction of individual cells. Colors depict cell clusters (packs) that move collectively. Cells that exist near the jamming transition, move in packs that become progressively larger and slower as the jamming transition is approached. As cell–cell junctions lose cadherin-dependent adhesion, the tissue becomes fluidized and unjammed. Adapted from [131, 146, 100].

The first possible mechanism of a liquid to solid transition is jamming. Jamming is a term introduced in Soft Matter physics and defined as "a transition from a fluid-like to a disordered solid-like state that occurs out of thermal equilibrium in the absence of Brownian motion, and that is driven by external forcing such as compression or shear" [9]. The onset of jamming is set by the jamming packing fraction ϕ_j, i.e. the fraction of available space taken up by the particles. For repulsive hard spheres, jamming starts when the packing fraction approaches the random close packing of spheres $\phi_{RCP} \approx 0.64$ - the maximal packing fraction that can be obtained when rigid monodisperse particles are packed randomly in 3D [9]. Below the jamming packing fraction ϕ_j, the system behaves as a liquid, but becomes rigid when $\phi \geqslant \phi_j$. The onset of jamming can be also defined from topological point of view by considering the packing geometry and, in particular, the contact number z, which is defined as the average number of contacts per particle. Indeed,

particles in a liquid can rearrange freely, but jammed matter is stuck by close contacts. Therefore, when the contact number is too small, the system is in a so-called floppy mode and its particles can move. However, there exists a precise minimum value of z, called the isostatic contact number z_{iso}, for which the system does not allow floppy deformations and reaches isostaticity. The value of z_{iso} can be established based on Maxwell's criterion which states that the system is isostatic when the number of constraints equals the number of the degrees of freedom of the system [115, 9]. For a system of N_p particles in d dimensions, the number of degrees of freedom is $N_{DOF} = N_p d$. However, each contact between two particles restricts their movement and thus adds a constraint to the system. Therefore, the total number of constraints $N_c = N_p z/2$, where z is an average number of contacts per particle. So if the system is isostatic, $N_{DOF} = N_c$, which leads to $z = z_{iso} = 2d$. Thus, for 3D systems, $z_{iso} = 6$, and for 2D systems, $z_{iso} = 4$. Systems with z below z_{iso} behave as liquids, but undergo the jamming transition when z exceeds z_{iso}.

In analogy to jamming transitions in Soft Matter, cellular jamming can cause such transitions in biological tissues. As cells adhere, divide and tend to form aggregates, their density increases, which can finally lead to jamming and, thus, to solidification (i.e. absence of flow). However, many biological tissues are confluent, meaning that there is no space between the cells, and their packing fraction is 1. Therefore, for such tissues, solidification due to the jamming transition does not exist.

Nevertheless, it was shown recently that confluent tissues can still undergo liquid to solid transitions. These transitions are not driven by density, but rather by the deformability of the individual cells. In 2D numerical models of tissues, this deformability is defined as $p_0 = P_0/\sqrt{A_0}$, where P_0 and A_0 are the cell's perimeter and area respectively. Bi *et al.* showed that increasing p_0 higher than a critical value leads to a solid-liquid transition in 2D [12]. In other terms, a higher cell deformability favors a liquid behavior of the tissue. This critical value of p_0 was directly related to T1 events that are the basis of fluidity in confluent tissues [160]. A T1 event is a rearrangement in a group of 4 cells (Fig. 1.8A), where two of them (cell 1 and cell 2) are initially in contact, and the other two are not (cell 3 and cell 4). The T1 event consists in breaking the existing contact between cells 1 and 2 and establishing a new contact between cells 3 and 4. Such a rearrangement has some energetic cost $\Delta\varepsilon$. Bi *et al.* demonstrated in numerical simulations that increasing p_0 (i.e. making cells more deformable) decreases this cost, thus allowing the 2D model to switch from a solid-like to a liquid-like behavior (Fig. 1.8B). In living tissues, the deformability of the cells is determined by the ratio between intercellular adhesion and cortical tension of the cells (see Fig. 1.4). Indeed, increasing adhesion leads to an increase in the perimeter of the cell, and therefore, to an increased cell deformability. On the contrary, an increase of cortical tension would decrease the perimeter of the cell and its ability to deform. Thus, an increase of intercellular adhesion favors the liquid behavior of tissues, while an increase in cortical tension results in tissue rigidification (Fig. 1.8C). The dependence of tissue rigidity on the cell deformability was also reported in experiments [133]. Moreover, recent work has demonstrated that such models can quantitatively predict cell rearrangement rates in body axis elongation in the fruit fly [166, 170], if one also takes into account cell alignment in the packing. Similar effects are predicted in 3D [119].

Finally, by analogy to the effect of temperature in physics, liquid to solid transitions in tissues

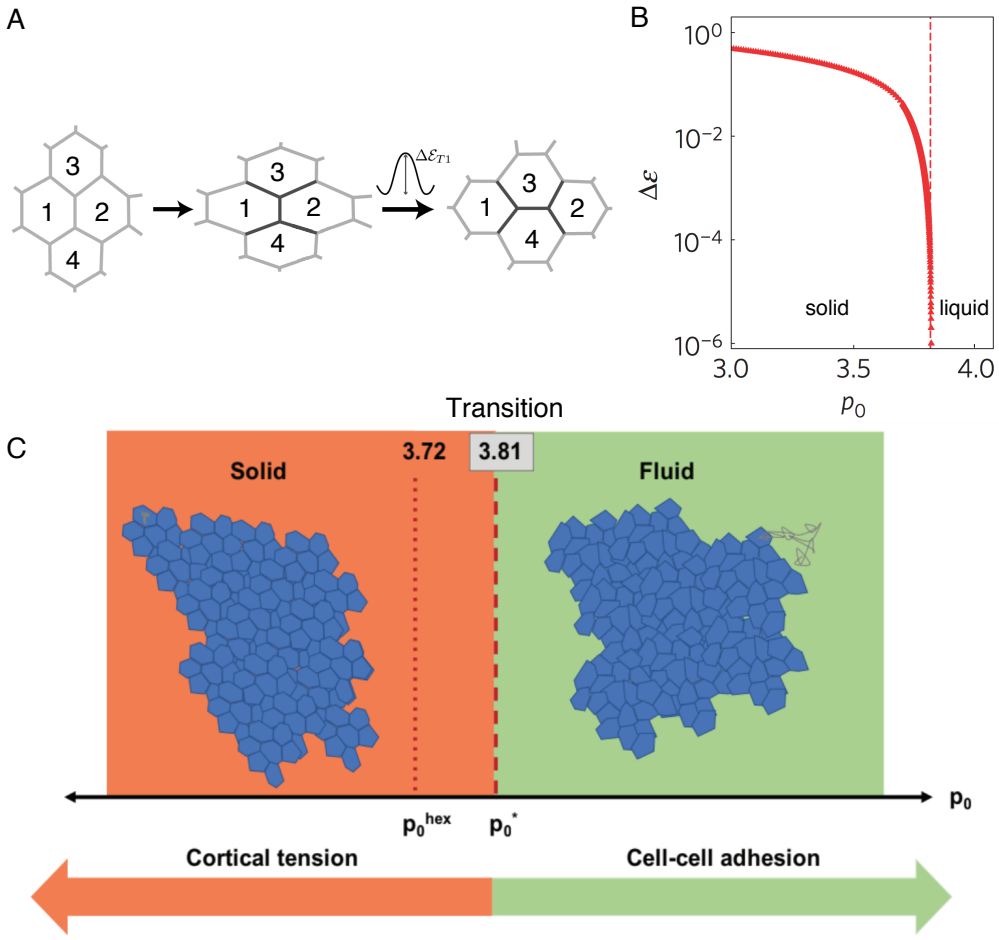

Figure 1.8 | **Energy barrier for cell rearrangements in confluent tissues.** (A) A sketch of a T1 event. Initially relaxed cells (left) flatten during the T1 event due to stress (middle). For cells to rearrange, an energy barrier $\Delta\varepsilon$ has to be overcome. After the rearrangement, the cell shapes relax by dissipating energy (right). Adapted from [111]. (B) Energy barrier for a T1 event as a function of p_0. Adapted from [12]. (C) Speculative diagram of the dependance of a solid to liquid transition on the cortical tension and adhesion. Adapted from [122].

can be mediated by cell motility. Indeed, the ability of a cell to actively move allows it to escape the constraints imposed by its neighbors, thus creating a flow. And on the contrary, theoretical tissue models showed that tissues become more solid-like with a decrease of the cell motility [74, 13].

Role of adhesion in solid-to-liquid transition

The role of adhesion is different in the case of confluent and non-confluent tissues. Computational studies showed that in non-confluent tissues, cell-cell adhesion performs a role very similar to that expected in systems with adhesive spheres: presence of adhesion generates larger intercellular spaces, which increases the fluidity of the tissue via a decrease in the packing density [164, 92]. These results were experimentally confirmed by Mongera *et al.*, by studying the effect of dis-

ruption of N-cadherin-mediated adhesion on vertebrate body axis elongation in zebrafish [127]. Similar results were found by Ilina *et al.*, who showed that deregulation of adherens junctions by downregulation of E-cadherin and p120-catenin determined unjamming transition in breast cancer invasion [78].

In confluent tissues, the role of adhesion is much more subtle and likely cell-type specific [100]. Intuitively, an increase in adhesion between cells is supposed to increase the contact area between them and, therefore, to increase the cell perimeter P_0. As it was already explained above, increasing cell perimeter leads to tissue fluidization. And indeed, two cells in contact experiments showed that increasing cadherin expression increased the surface area of a cell-cell contact [169]. However, experiments with confluent monolayers of keratinocytes demonstrated that an increase in cell contact corresponded to a knockdown of E-cadherins, i.e. lower adhesion [147]. In some ways, these subtle behaviors are not surprising, as cadherin signaling can significantly tune the mechanics of the cortical cytoskeleton [1, 107], so that increases in adhesion are often balanced by changes to cortical tension that have an opposite effect [100].

Role of cell polarity on the mechanical properties of tissues

In this context, the role of cell polarity (i.e. spatial differences in the organization of cellular components) is especially interesting. In polar cells, adhesion molecules and components of the cytoskeleton are localized asymmetrically, along interfaces with a specific orientation, generating large-scale anisotropic forces [11, 173]. Such forces can alter the mechanical properties of the tissue and cause a phase transition. For example, Duda et al. showed that tissue stretching induces polarization of actomyosin in the cells and formation of actomyosin cables across the tissue, which leads to rigidification of the tissue [43]. The mechanism underlying such rigidification is similar to rigidification of biopolymer networks under applied strain: the networks are floppy under a small strain, but become rigid when the applied strain exceeds some critical value [93, 143, 155]. The importance of cell polarisation was also demonstrated by Wang *et al.* [166]. They found that tension-driven rigidity predictions from cell deformation alone were not able to predict correctly cell rearrangements rates during convergent extension of Drosophila epithelium. However, their predictions closely matched with experimental observations when cell anisotropy were taken into account as well as their deformation.

1.3 Soft matter analogues of tissues

Due to shared similarities between tissues and inert materials, soft matter systems have been widely used as a way to study the mechanical properties of tissues [64]. In particular, specific aspects of tissue behavior have been explained by analogies with other soft materials, such as viscoelastic pastes [42], foams [70], emulsions [141] and colloids [41].

Indeed, biological tissues, soap foams and granular packings can all be described using the same

framework. For instance, from a topological point of view, they they can all be described in terms of space tessellations. It was also shown that their topology is controlled by common laws that determine the neighborhood of each cell as a function of cell size and polydispersity in the packing [129, 103]. Those similarities, both from this topological, but also dynamical and mechanical stand points, led to the use of foams and emulsions as soft matter models of biological tissues [64].

Among different soft matter analogues of biological tissues, one that first caught the attention of scientists were foams. For example, interfacial energy models derived from soap foams were shown to efficiently predict the highly organized structure of cells in organs such as the Drosophila eye [76]. These models are based on a minimization of the surface energy of the cells taking into account their membrane elasticity and the strength of adhesion. The behavior of foams have also been widely studied under mechanical constraints [29, 7]. In particular, it has revealed the importance of T1 rearrangements for yielding in those materials. Indeed, the succession of local T1 rearrangements called avalanches was associated with stress relaxations in confined foams, and thus enables their flow [85]. The nature of avalanches and their role in yielding of soft matter materials will be discussed in more details in Chapter 3.

However, there are significant differences between foams and biological tissues. First of all, air bubbles in foams can dissolve in the continuous phase, which makes them coarsen through ripening on short timescales. As a result, the average bubble size as well as the microstructure of the foam spontaneously evolve over time. Moreover, the attraction between bubbles has only been tuned through non-specific depletion forces that depend on the concentration of micelles or macromolecules in the system [5], while protein-mediated adhesion between cells in tissues is specific.

The use of emulsions (for instance, oil droplets in water) as tissue mimics overcomes these limitations. Indeed, emulsions can be stable for months if the chosen continuous and dispersed phases are insoluble in each other, and the droplets being liquid are also incompressible and exhibit typical surface tensions of 10 mN/m, which is similar to the ones of cells and aggregates [135]. In addition, different methods of emulsion production allow to control precisely the size of the droplets and their polydispersity. Moreover, as droplets are deformable and since their deformation depends on their surface tension and the applied load, emulsions can be used to directly measure the forces in the packings [82, 24], which is not accessible with hard spheres [148, 32].

Finally, the oil/water interface on the droplets is functionalizable, as described in more details in the next section. Functionalization makes it possible to introduce specific adhesion between droplets. Thus, functionalized emulsions provide a possibility to study experimentally the effect of specific adhesion on the mechanics of granular materials and tissues.

1.4 Biomimetic emulsions as a soft matter model of tissue

1.4.1 Biocompatible droplets to probe cellular forces

Up to now, droplets have been used to tackle various questions concerning biological tissues. Fattaccioli *et al.* [50] used emulsions to mimic cellular adhesion on a solid surface and to study the role of non-specific interactions between adhesive surfaces, as well as the effect of the density of specific binders on the total energy of adhesion. As it is possible to make emulsion droplets biocompatible, they have been used together with living cells or even have been introduced into biological tissues [142, 44, 127, 125]. For instance, Pinon *et al.* used oil droplets to study the formation of immunological synapses [136]. For this, they modelled a cell-cell contact as a droplet-cell contact using functionalized oil droplets. Such a system allowed them to tune precisely different parameters of the contact, such as the membrane stiffness, and to measure their effects on the synapse formation. Droplets have also been used as biomimetic cellular barriers for immune cells [125] or as force sensors in cohesive tissues [127]. The use of biomimetic droplets as force sensors in tissues will be further discussed in Chapter 4.

Beyond the use of droplets as single cells analogous, adhesive packings of dense biomimetic emulsions can actually display the same mechanical properties of biological tissues [141]. Below, I am explaining what has already been done in this regard.

1.4.2 Composition of biomimetic emulsion systems

It is only fairly recently that biomimetic emulsion systems with various functionalization pathways have been proposed to mimic biological tissues [141, 51, 140]. These systems consist of functionalized droplets interconnected with each other through specific binders. An example of such systems is sketched in Fig. 1.9A. The radius of the droplets can be tuned to match the one of cells in developing tissues. The oil-water interface of the droplets is stabilized by a fluid monolayer of phospholipids that mimics the outer leaflet of the cellular membrane. In order to mimic the intercellular adhesion mediated by homophilic cadherins in tissues, droplets can be functionalized with specific binding molecules. Moreover, the droplets surface tension can be adjusted by tuning the amount of phospholipids introduced at the interface, and by adding co-surfactants such as sodium dodecyl sulfate (SDS). Tuning the surface tension allows to control the propensity of the droplets to deform under mechanical constraints. Finally, index-matching of the continuous (water) and dispersed (oil) phases makes the emulsion transparent, which allows one to see inside the packing and image its microstructure in 3D, using confocal microscopy. When the functionalized droplets are packed, a binder on one surface diffuses until it binds to the complementary binder on the neighboring surface [20, 50, 141]. This process eventually leads to the formation of adhesive patches that are enriched in fluorescent binders as shown in Fig. 1.9B.

This system allows to probe different aspects of a specific adhesion and tune the adhesion energy

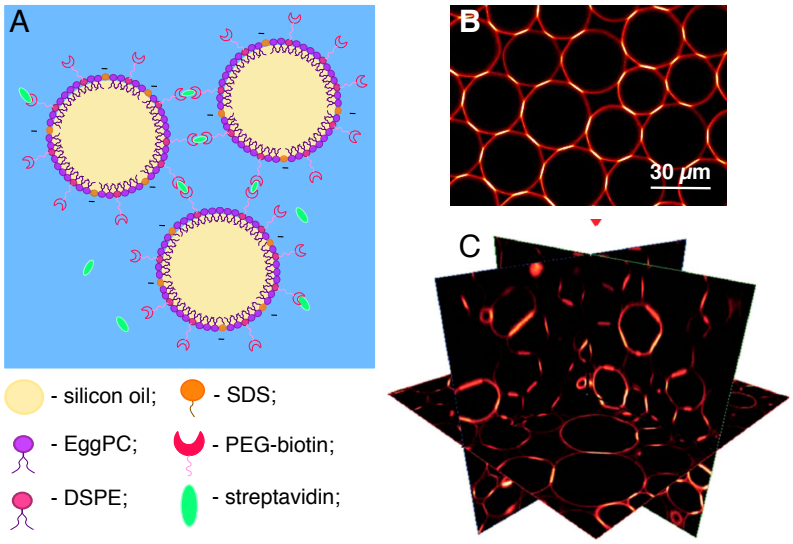

Figure 1.9 | (A) Schematic representation of functionalized emulsions. The oil–water interface is stabilized by a mixture of phospholipids and negatively charged SDS. Some of the lipids hold a PEG-biotin group that allows binding through biotin-streptavidin interactions. (B-C) Confocal images of fluorescent droplets (B) and their 3D representation (C, adapted from [141]). Adhesive patches between the droplets are the areas of brighter fluorescence.

between the droplets. This can be done by varying the type of binders on the droplets surface. In particular, droplets can be functionalized with three possible types of binders:

- First, droplets can adhere through quasi-permanent biotin-streptavidin bonds. In this case, biotinylated lipids grafted on the droplets surface bind to streptavidin molecules available in the aqueous phase. The energy associated with forming such a ligand-receptor bond is on the same order as those in cadherin mediated adhesion [132, 171].

- The second possibility is to use complementary DNA strands [67, 51, 176]. The droplets are functionalized with single DNA strands, and upon contact, the droplets adhere through the thermally reversible hybridation of complementary single strands into a stiff DNA double helix. The binding energy associated with this reaction (and hence the melting temperature of the double helix into two single strands) depends on the length of the DNA sequence, which provides specific and programmable interaction between the droplets.

- Finally, it is possible to introduce cadherin adhesion between the droplets. To do so, the droplets are grafted with the adhesive extracellular domains of E-cadherin through a histidine tag [140]. E-cadherin-E-cadherin binding is calcium dependant and was shown to form on the droplets surfaces both *trans*- and *cis*- bonds, similarly to cadherin adhesion in biological tissues.

The resulting adhesion dynamics between the droplets depend on the energy of the binders as well as the diffusion dynamics on the surface of the droplets [165, 6]. Indeed, upon contact, the

binders have to diffuse on the surface of the droplets and progressively enrich at the contact to form an adhesion patch. Choosing oils with lower/higher viscosities allows to decrease/increase the viscous drag of the phospholipids at the interface and thus ensure faster/slower diffusion of the binders [139], which should in turn accelerate/slow down the adhesion process.

1.4.3 Emulsions as models for static packings of cells in tissues

Pontani *et al.* showed that dense emulsions packed in 3D can mimic the packing of cells in tissues [141]. In order to reach homeostatic pressures that are typical for tissues ($\approx 10kPa$) [33, 69], emulsions were put under different levels of external compression through centrifugation. Specific adhesion was introduced through biotin-streptavidin-biotin bonds, and electrostatic repulsive forces between droplet surfaces were controlled by tuning the salt concentration in the aqueous phase. The use of fluorescent streptavidin together with index-matching between the droplets and the continuous phase allowed to image the 3D structure of the packings, and, therefore, to find the threshold compression force needed to overcome electrostatic repulsion and surface elasticity and establish protein-mediated adhesion.

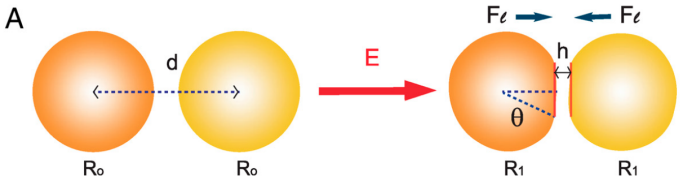

Figure 1.10 | Idealized droplet deformation under a compressive force F_l. The total energy E depends on the interdistance h and the deformation angle θ. Adapted form [141].

In order to quantitatively assess adhesion in the emulsion system, a free energy model was developed to capture the evolution of the adhesion strength with the applied pressure. This model considers various energy terms that affect the formation of the adhesive patch: the binding energy E_b of the adhesive proteins, the work W_l done by the applied external pressure to put droplets in contact, the electrostatic repulsion energy E_r between the droplet surfaces and the elastic cost of droplet deformation E_d. In this case, E_b and W_l favor the adhesion, while E_r and E_d limit the adhesive patch formation. According to the model, the size of the adhesive patch at equilibrium is therefore set by the minimization of the total free energy E of the system (with respect to the distance h between the droplet surfaces and the deformation angle θ), which can be described as

$$E = E_d + E_b + E_r + W_l \tag{1.2}$$

Data were well fitted by this model and yielded parameter values (e.g. surface tension or binder concentration in the patch) close to those measured in cells and cellular aggregates. The agreement between the predicted values and reported cell values validates the use of biomimetic emulsions as a model system for biological tissues.

Another model describing the formation of adhesive patches was developed by Feng *et al.* [51],

who worked with biomimetic droplets functionalized with complementary DNA strands (Fig. 1.11). They characterized the change in the total free energy for a system of two droplets in the unbound and bound states taking into account energy terms associated to the loss of entropy upon binding. This model, in good agreement with the experimental data, was able to capture the dependence of the adhesion strength on the number of DNA molecules on the droplet surfaces. Using the

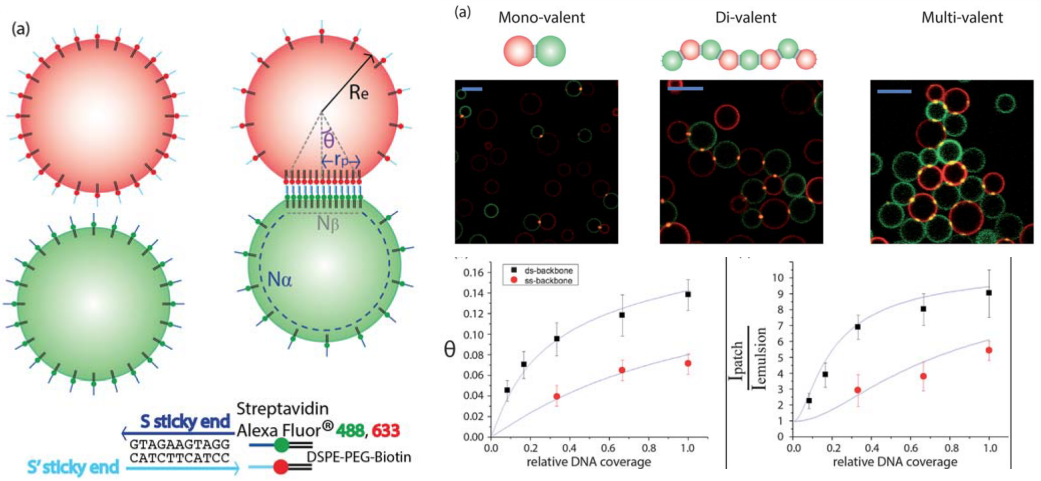

Figure 1.11 | (A) The silicone oil droplets are stabilized with phospholipids, some of which are labeled with fluorescent streptavidin that allows the grafting of S or S' DNA strands on green and red streptavidins respectively. The complementary S and S' sticky ends then bind and form adhesion patches enriched in DNA tethers between the droplets. (B) The patch angle θ and relative intensity are plotted as a function of the relative DNA coverage on the droplets. The experimental data are well fitted by the model (solid lines). (C) Monovalent doublets (left), divalent droplet chains (center) or higher valency clusters (right) are self-assembled by controlling the binders concentration. Adapted from [141].

predictions of the theoretical model and varying the number of binders and length of the DNA chain, Feng *et al.* obtained structures with different valency (e.g. the number of patches, and thus neighbors one droplet could have). They found that increasing the valence induced rigidification of the system: a valence 2 led to floppy polymers of emulsion droplets, while a valence above 4 caused rigid droplet networks (Fig. 1.11). These results confirm the importance of intercellular adhesion for the static and rheological properties of tissues, and the existance of several controlable parameters makes this system an appealing soft matter model to study it.

Finally, Pontani et al. [140] studied the 3D packings with E-cadherin-mediated-adhesion between droplets. They found that *trans* cadherin-cadherin adhesion appeared even in the absence of calcium and could stabilize looser packings [83]. When clustering agents, such as calcium, were added to the aqueous phase, the formation of lateral *cis* adhesion of the already bound cadherin pairs over the clustering of monomer cadherin on the surface was observed. Moreover, increasing the concentration of cadherin and calcium over a threshold triggered fusion of the droplets. However, the fusion did not cause full demixing of the emulsions and progressively slowed down until the system reached the steady state. Such arrest of the fusion was explained by the decrease of surface tension upon fusion. Interestingly, the replacement of cadherin by biotin-streptavidin-biotin

bonds under the same concentration of calcium led to droplet-droplet adhesion, but did not give rise to fusion. These results highlight the importance of the *cis* interactions of cadherins, in agreement with current observations in cells, where jammed adhesion rings were also observed [106, 45]. Altogether, this study showed the importance of the emulsion model system, which appropriately mimics the two-dimensional binding of stiff interfaces in cells.

1.5 Conclusion and thesis objectives

The behavior of biological tissues during morphogenesis is a complex mechano-chemical process, which is strongly dependent on a feedback loop between cellular adhesion and mechanical properties of individual cells, that are determined by their cytoskeleton. Overall, the mechanical and rheological properties of biological tissues resemble those of soft matter materials, and can be quantified using various techniques. The observed similarities between tissues and amorphous materials allow to use soft matter systems as mechanical models of biological tissues. In particular, biomimetic emulsions were shown to be a good model to study the mechanical properties of tissues. In my work, I have thus used phospholipid-stabilized emulsions to unveil the mechanical pathways of morphogenesis. My PhD project is centered on two complementary approaches: *in vitro* and *in vivo*.

The first axis of my PhD is focused on the role of interdroplet adhesion on the elasto-plastic behavior of biomimetic emulsions under mechanical perturbations by flowing them through microfluidic constrictions with controlled geometries. Image analysis allowed us to distinguish between an elastic response, in which the droplets deformed and kept their neighbors, and a plastic response, in which droplets rearranged their positions irreversibly. We compared the behavior of repulsive and adhesive emulsions, and investigated the role of non-specific and specific adhesion in their elasto-plastic response under mechanical perturbation. The results of this part are presented in Chapter 3.

The second axis of my project was done in collaboration with Marie Breau of IBPS-LBD. It consisted in injecting adhesive oil droplets into the embryo of zebrafish to study the role of mechanical forces in the neuronal development of the olfactory placode (OP). We aimed at obtaining a map of the forces generated in the OP during embryogenesis. The detailed description of this part is given in Chapter 4.

Both complementary approaches revealed the underlying regulations of adhesion and mechanical properties that take place during morphogenesis. The ongoing development of the projects, as well as future steps are described in Chapter 5.

Chapter 2

Materials and Methods

Я сверлю сто третью дырку, мне еще полдня пахать...[a]
"Конвейер", ДДТ.

[a] I am drilling the one hundred and third hole; I still have half a day to slog...
A song from DDT.

In this chapter, I will describe in depth the systems and experimental tools I developed throughout my PhD in order to produce oil in water emulsions and to image them while they are mechanically perturbed.

2.1 Emulsion production

In our experiments, we work with monodisperse and polydisperse direct oil in water emulsions. Both polydisperse and monodisperse emulsions are produced using silicon oil (viscosity 50×10^{-6} m^2/s, Sigma Aldrich) as the oil phase, and 10 mM sodium dodecyl sulfate (SDS, Sigma Aldrich) water solution as the continuous phase. There are currently three main techniques available to produce emulsions: microfluidic emulsification [89], viscoelastic shear [14, 25] and membrane emulsification [84]. Importantly, these techniques differ by the level of polydispersity of the produced droplets and the production rate. Therefore, we use several of them according to our needs, as explained below. In order to measure the polydispersity of the produced emulsions, they are imaged with a 10x objective in bright field microscopy. The acquired images are analysed using a custom made Matlab routine that allows to extract the droplets diameter. The polydispersity is then calculated as the standard deviation of the droplets diameter.

2.1.1 Monodisperse emulsions

We use microfluidics to produce monodisperse emulsions. Since an emulsion in a microfluidic device is made by precisely fabricating one drop at a time, this process results in a highly monodisperse emulsion, but has a rather low production rate. The size of the droplets is set by the width of the channels at the flow-focusing junction and by the relative flow rates of the continuous and dispersed phases.
We cast a flow-focusing microfluidic chip in polydimethylsiloxane (PDMS, Sylgard 184, Dow Corning, USA) against a mold fabricated by Adéle Dramé-Maigné (SPM team, Gulliver lab, ESPCI) using photolithography. This device consists of a simple cross junction (*see* Fig. 2.1A), where the dispersed phase (oil) is broken up into droplets by the continuous phase (water). The width of the channels is 60 μm, and it reduces down to 30 μm at the flow-focusing junction. The silicone oil and SDS solution are injected using a pressure pump (MFCS-8C Fluigent, $P_{water} \approx 300$ mbar, $P_{oil} \approx 600$ mbar). The resulting emulsions display an average droplet diameter of 45 μm and polydispersity of 3.9% (Fig. 2.1C).

2.1.2 Polydisperse emulsions

When larger volumes of emulsions are needed for the experiments, polydisperse emulsions are produced using the membrane emulsification technique. According to this method, the dispersed phase is forced through a cylindrical Shirasu Porous Glass (SPG) membrane decorated with micropores directly into the continuous phase, that is maintained under vigorous agitation (*see* Fig. 2.1B). In this way, emulsified droplets are formed and detached at the end of the pores with a drop-by-drop mechanism. The size of the droplets is controlled by the size of the pores. We use a pressure emulsifier (Internal Pressure Type, SPG Technology Co.) located in the Pôle Microfluidique laboratory of the Institut Pierre-Gilles de Gennes (IPGG). Before production, the membranes should be properly cleaned. For this, the membranes are first sonicated for 30 minutes in toluene, and then for 30 minutes in acetone. Finally, the membranes are baked overnight at 500 °C to eliminate possible organic residues. The emulsification process is the following. The oil phase is stored in a pressure-tight vessel that is connected to a compressed air inlet. The continuous phase (100ml of 10mM SDS solution) is stirred with a magnetic bar in a beaker. By applying a pressure of compressed air (P = 5000 Pa), the oil phase is pushed through an SPG membrane decorated with 10 μm pores directly into the aqueous phase, where the droplets are stabilized by the dissolved SDS. The obtained emulsion is then washed in a separating funnel with 200 ml of 10 mM SDS solution. The resulting emulsion has an average droplet diameter of 35 μm with 21% polydispersity (Fig. 2.1C). All produced emulsions are finally stored at 4°C.

2.1.3 Tuning the continuous phase

After the emulsions have been produced, we replace the continuous phase according to the experimental needs. To do so, the emulsion is washed in a separating funnel with the desired continuous phase. In particular, we use buffers with two different concentrations of SDS: 10 mM and 45 mM. In addition, to enhance the imaging of the emulsions, we use a water/glycerol mixture (60:40 in volume) that has an optical index that is closed to that of the oil phase. Indeed, without glycerol the optical indexes of oil and water are not matched, which leads to the appearance of fringes at the droplet interface when imaged in bright field (*see* Fig. 2.2A).

2.2 Lipid stabilization and functionalization

2.2.1 Lipid stabilization

In order to enable future functionalization of droplets with binding molecules, and thus make biomimetic emulsions adhesive, the polydisperse oil droplets are stabilized with phospholipids. For this, we use a mixture of two different phospholipids that serve different purposes, as it was done by Pontani *et al.* [141]. The first ones are egg L- α-phosphatidylcholine (EPC) lipids. They constitute the major interfacial component that mimics the outer leaflet of cell membranes. The

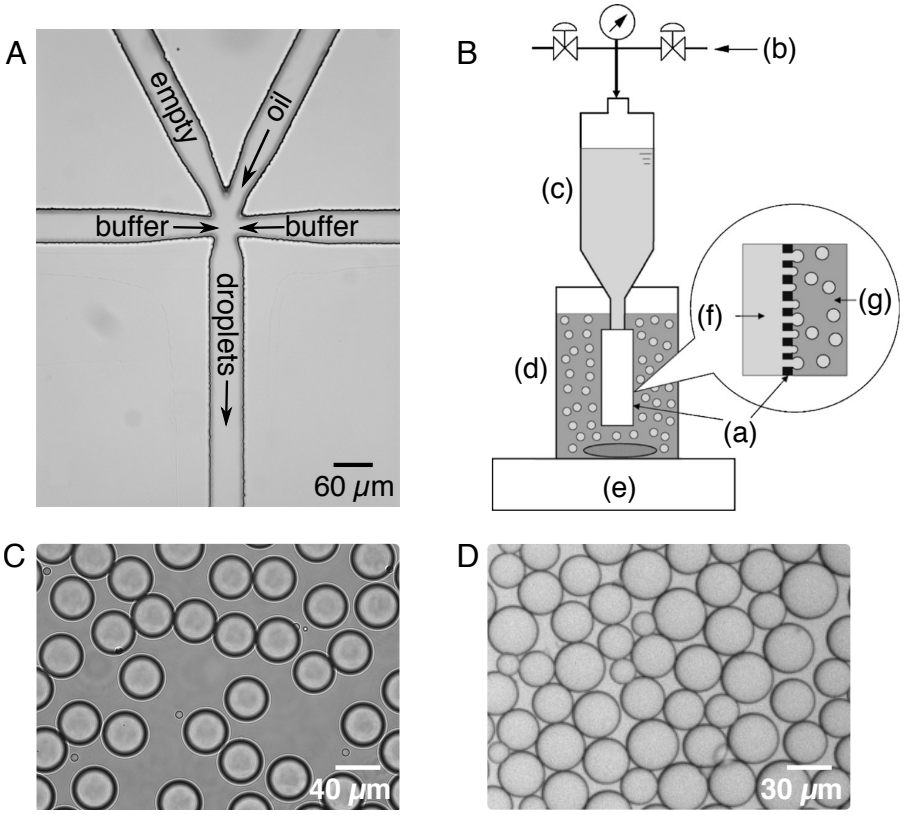

Figure 2.1 | **Methods of emulsion production** (A) Flow focusing device, top view. (B) Sketch of the experimental apparatus used for the preparation of oil/water emulsions using an SPG membrane: (a) SPG membrane module; (b) compressed air; (c) dispersed phase container; (d) continuous phase and emulsion container; (e) magnetic stirrer; (f) dispersed phase; (g) continuous phase. Adapted from [130]. (C-D) Bright field images of the produced emulsions: modisperse case (C), polydisperse case (D).

second component of the mixture is DSPE-PEG-biotinylated lipids that provide biotin ligands for the binding with streptavidin to mimic adhesion. Droplets are also co-stabilized with SDS that introduces electrostatic repulsion between the droplet surfaces [126], analogous to the charge repulsion between cell surface macromolecules [104]. The procedure of lipid stabilization is done in two steps with a gradual decrease in the concentration of SDS in the aqueous buffer. This way, we ensure the repartition of lipids at the droplets surface instead of SDS while avoiding coalescence of the emulsion.

The detailed protocol for lipid stabilization is the following. First, 9 mg of EPC lipids and 1 mg of DSPE-PEG(2000) biotinylated lipids (Avanti Polar Lipids) are dried with a nitrogen flow and dissolved in 500 μL of dimethyl sulfoxide (DMSO, Sigma Aldrich). Indeed, it was shown [137] that 10% DMSO in the buffer accelerates the repartition of lipids to the droplet surface. This mixture is then added to 5 mL of high SDS aqueous buffer (5 mM SDS, 10 mM Tris, pH=7.5). The resulting solution is sonicated for 30 minutes. We then add 2 mL of emulsion cream to the phospholipid containing buffer and leave it to incubate overnight at 4°C. After incubation the emulsion is washed with 100 mL of high SDS buffer (5 mM SDS, 10 mM Tris) in a separating

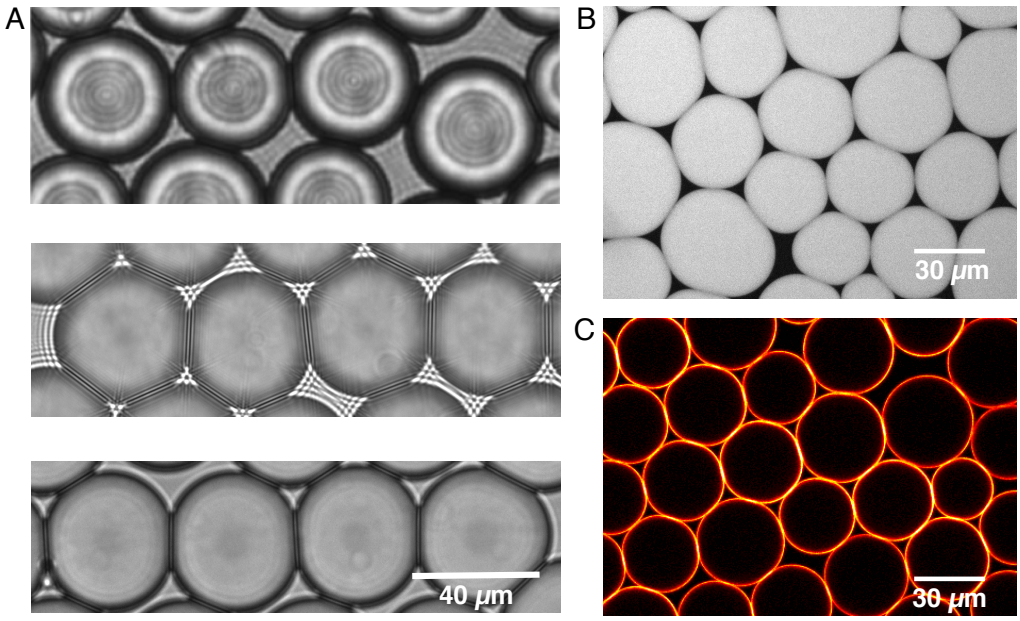

Figure 2.2 | **Imaging of the emulsion droplets.** (A) Effect of adding glycerol on the visualization of the emulsion in 10 mM SDS buffer with bright field microscopy. Without glycerol (top and middle) the optical indexes of oil and water are not matched, which leads to the appearance of fringes at the interface. Adding 40% glycerol (bottom) improves the visualization. (B) Polydisperse droplets labeled with Nile Red (10 mM SDS in 40% glycerol). (C) Polydisperse droplets functionalized with Alexa-555 conjugated streptavidin (1 mM SDS, 10mM Tris, 10 mM NaCl in 40% glycerol).

funnel and set for a second round of stabilization. The low SDS aqueous solution used for this last round contains 1 mM (instead of 5 mM) SDS while the rest of the procedure for lipid dissolution remains unchanged. After this last incubation, the emulsion is washed again in 100 mL of low SDS buffer (1 mM SDS, 10 mM Tris) in a separating funnel. The resulting droplets display an average diameter of 35 μm (with a polydispersity of 21%) and are stable over several weeks when stored at 4°C.

2.2.2 Functionalization with streptavidin

In order to make droplets adhere to each other, as well as to fluorescently label them, the droplets are functionalized with streptavidin Alexa Fluor 555-conjugated (Invitrogen), as shown in Fig. 2.2C. To this end, 200 μL of the emulsion cream is mixed with 3.6 μL of streptavidin (1 mg/mL) and 200 μL of 10 mM SDS buffer. The resulting solution is incubated for 1 hour at room temperature to allow the streptavidin to bind to the biotinylated lipids on the surface of the droplets. After that, the aqueous buffer under the emulsion cream is removed with a gel-loading pipette tip. The emulsion is then washed twice in the 800 μL of 10 mM SDS buffer in order to wash out unbound streptavidin, and once with 1 mL of a water/glycerol mixture (60:40 v:v) containing 1 mM SDS, 10 mM Tris, 10 mM NaCl and 0.05 mg/mL casein (β-casein from bovine milk, Sigma Aldrich). The salt favors adhesion by dampening electrostatic repulsion between the droplets [141], and casein

prevents the interaction between droplets and their container.

2.2.3 Fluorescent labelling with Nile Red

For some experiments, the dye Nile Red (Sigma Aldrich) is used to fluorescently label the emulsions (Fig. 2.2B). To this end, we dilute a 100 mM SDS solution saturated with Nile Red to the desired SDS concentration (10 or 45 mM). We then add 1 ml of the emulsion cream to 15 ml of the solution and let the mixture incubate overnight, allowing the dye to partition between the oil and water phases.

2.3 Experimental set-ups

2.3.1 2D static packings

We studied the role of adhesion on the static structure of 2D polydisperse droplets. To this end, we placed a 10 μL drop of the emulsion between a microscope glass slide (76 $\times$ 26 mM, Objekttrager) and a cover slip (24 $\times$ 60 mm, Knittel Glaser) separated by spacers (50 μm or 30 μm thick polymethylmethacrilate - PMMA-film, Goodfellow). In order to prevent evaporation, the samples are sealed with sticky wax (Sybron Dental Specialties, Kerr), as it is inert compared to other sealing agents, such as nail polish or glue.

2.3.2 Fabrication of microfluidic constrictions

To mechanically perturb the emulsions, we used a microfluidic constriction. The chip is composed of three sections (Fig. 2.3). First, at the inlet, the channel is wide and can accommodate several rows of droplets. It is followed by a constriction region, where the width of the channel progressively decreases until the constriction ends in a one drop-wide channel which leads to the output. In order to maintain the droplets in a monolayer, the depth of the channel was adjusted to the diameter of the droplets. The channel was made in crosslinked PDMS using a negative cast that was engineered with a micromilling machine (desktop Mini-Mill machine, Minitech Machinary Corp., USA).

In order to engineer the cast, we first design the channel using the Autodesk Fusion 360 software. This software allows to generate a G-code that encodes the instructions for the micromilling machine. The negative cast is then micromachined in a block of acrylic glass - PMMA ($50 \times 50 \times 5$ mm^3). Prior to milling, in order to ensure a constant depth of the channel, we make the surface of the block flat. For this, we remove the top 50 μm of material over a rectangular region (4x4 mm) with a 3 mm square-end mill (NS TOOL Co., LTD), then, in order to smooth out possible traces of the squared mill, we remove a layer of 1 μm deep with a 3 mm torque mill (NS TOOL Co., LTD), and finally polish the surface with Miror (Miror Formule Cuivre, Henckle).

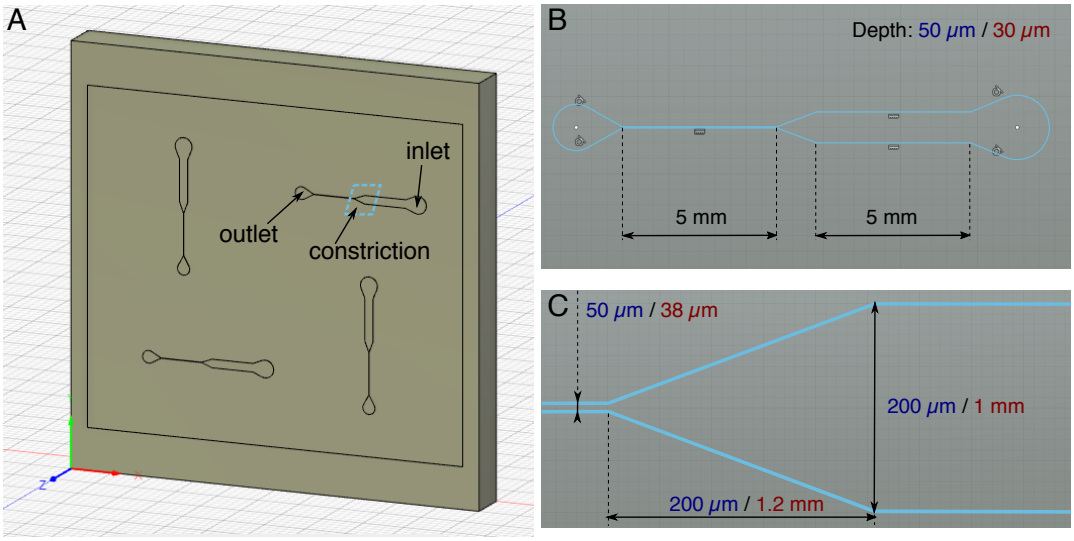

Figure 2.3 | **Schematic representation of the microfluidic channel.** (A) Microfluidic devices designed in Fusion 360. (B) A sketch of the microfluidic device that consists of a wide channel, constriction and a thin channel. The dimensions of the device are indicated in dark blue fonts for the channel used with monodisperse emulsions, and in dark red fonts for the channel used with polydisperse emulsions. (C) Zoom on the constriction area of the microfluidic device.

After that, the negative cast is milled in the surfaced block using the 3 mm square-end mill. A final cut is done along the contour of the channel with a 50 μm square-end mill (Performance Micro Tool, USA) in order to smooth out the contour of the channel. To clean the cast and get rid of all possible debris, the cast is sonicated in a soap solution three times for 10 minutes. We check the depth of the milled channel using a profilometer (M3D, Fogale Nanotech).

Using the technique described above, we prepare two different channels (*see* Fig. 2.4A). While the three sections are preserved in both channels, their dimensions are different. The first channel is designed for monodisperse emulsions. At the entrance, the channel is 200 μm wide over a 5 mm length, then at the constriction the width is reduced from 200 to 50 μm over a length of 200 μm, finally the channel is 50 μm wide over a final 5 mm length. The depth of the channel remains 50 μm through all three sections.

The second channel is prepared for polydisperse emulsions. As the average diameter of polydisperse emulsion is smaller than the diameter of monodisperse emulsion (35 μm vs 42 μm), the depth of the channel is adjusted to 35 μm. In addition, to eliminate possible boundary effect due to the channel borders, we increase the width of the channel: at the inlet, the channel is 1 mm wide over 5 mm length, then at the constriction the width is reduced from 1 mm to 38 μm wide over a length of 5 mm, and then the channel remains 38 μm over 5 mm before the outlet.

The negative cast is used to mold a channel in PDMS. First, the PDMS base is mixed with its curing agent 10:1 (w/w) ratio and centrifuged for 15 minutes in order to remove large air bubbles. Then, the liquid mix is poured into the mold and put in a vacuum desiccator to further remove air bubbles and improve transparency of the PDMS. After this, the PDMS is cured overnight in an

oven at 65 °C. The PDMS channel is cut out from the mold with a scalpel, and inlet and outlet holes are punched with a 1.5 mm puncher. Finally, the PDMS elastomer channel is sealed with a glass slide using an oxygen plasma treatment (P = 0.4 Torr, exposure time = 1 min.).

2.3.3 Flowing set-up

The inlet of the channel is connected to a pressure pump (MFCS-8C Fluigent) with a Tygon tubing (PHYMER), and the outlet of the channel is equally connected to a waste collection beaker (*see* Figure 2.4). Before running the experiment, the channel is passivated with a β-casein solution (0.05-0.25 mg/ml depending on the emulsion). That is done to avoid any interaction between droplet surfaces and the channel boundaries. To prepare the casein solution, we dissolve a powder of β-casein from bovine milk (Sigma Aldrich) in an aqueous buffer (10 mM Tris, pH = 7.5) at a concentration of 1 mg/ml. This solution is then diluted with water to reach the desired concentration. The channel is filled with this diluted solution using the pressure pump (P = 30 mbar) and left to incubate for 20-40 minutes (P = 10 mbar). Meanwhile, a reservoir containing the emulsion cream in the water/glycerol buffer is connected to the pressure pump. After incubation, the inlet is connected to the reservoir containing the emulsion. As the emulsion creams, the tube is first plunged into the buffer underneath the emulsion cream. This way, the channel is washed with the buffer for 15 minutes (P = 30 mbar). Then, we pull up the tube so that it plunges in the cream phase. Once the droplets have filled the channel, the pressure is decreased to stop the emulsion flow (P = 5 mbar) and the droplets are left to pack overnight, during which adhesion patches grow (*see* Fig. 2.4C). After the incubation phase, the emulsion is flowed in the channel under constant pressure (P = 15-60 mbar depending on adhesion). The flow of droplets at the constriction area is imaged either in bright field or through confocal microscopy with a 10X or 20X objective at a frequency of 15 frames per second (fps) for polydisperse emulsion, or 20 fps for monodisperse emulsion, and an exposure time of 20 ms. When the whole constriction region does not fit the field of view, we use a stitching procedure: the constriction is imaged in parts that are added starting with the region which is the closest to the thin channel to have the full image. Typically, each region is mapped with 1000 images (Fig. 2.4A).

2.3.4 Imaging

We use a Nikon Eclipse 80*i* microscope (Qimaging RETIGA R3 camera) equipped with a spinning disk confocal microscopy module (Spinning Disc Crest Xlight V2, Gataca systems). Compared to epifluorescent microscopy, confocal microscopy enhance the imaging by rejecting the out-of-focus light with the use of conjugated pinholes. This results in a greater resolution, a greater contrast and a reduced noise. As opposed to laser scanning confocal microscopy (LSCM), which uses a single pinhole, a spinning disk confocal microscopy (SDCM) has hundreds of pinholes arranged in spirals on an opaque disk, which rotates at high speeds. When spun, the lazer beam scans through the pinholes across the sample in rows, building up an image. Using a spinning disk thus improves the speed of image acquisition (allowing for imaging fast dynamic processes and live specimens),

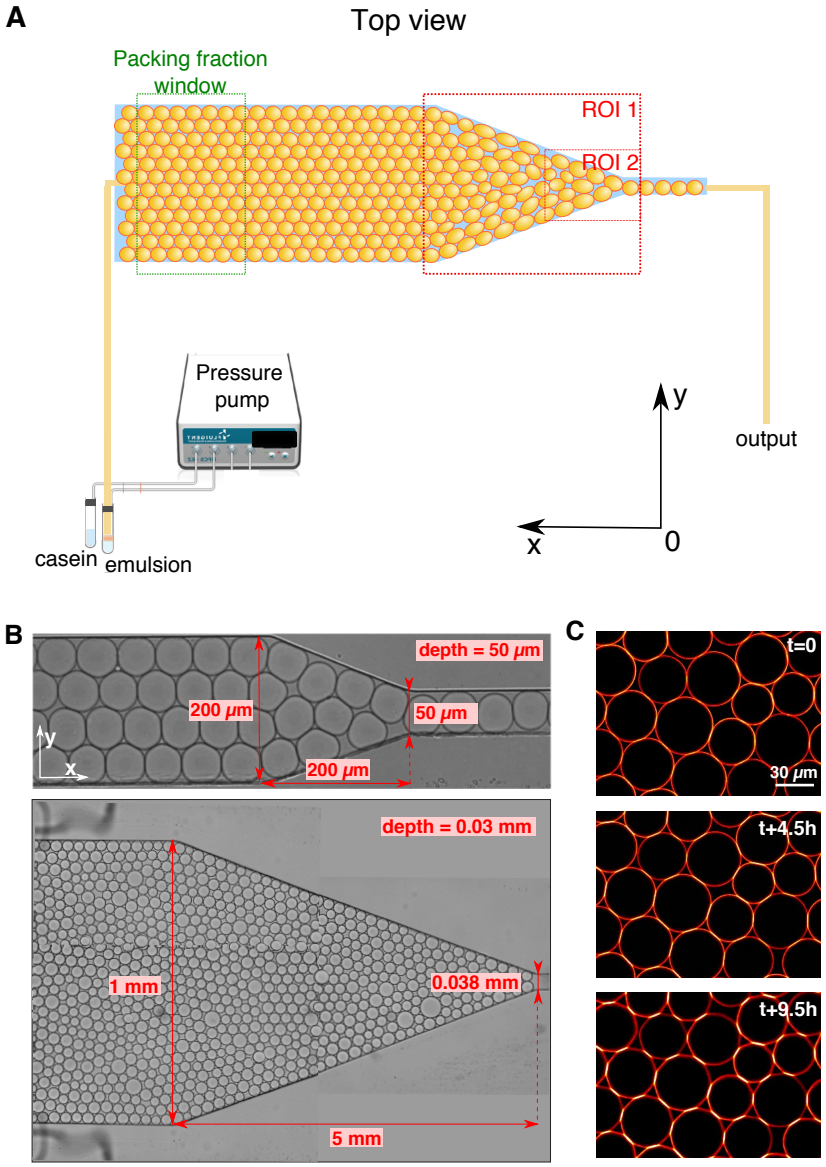

Figure 2.4 | **Experimental set-up** (A) The oil in water emulsion is pushed using a pressure pump through the microfluidic channel that consists of three parts: a wide channel, a constriction, and a thinner channel. We film the emulsion flow either in the constriction region, or in the area of the constriction located right before the beginning of the thin channel (*see* red dashed squares for region of interest). The packing fraction of the emulsion is determined within the window of 200x200 μm located before the constriction area (green dashed rectangle). (B) Bright field images of the constriction area for monodisperse (top) and polydisperse (bottom) emulsions. (C) Progressive formation of adhesive patches over time. The top confocal image shows that Alexa-555 streptavidin fluorescence is more homogeneously distributed over the surface of the droplets at the beginning of the experiment. Over time, biotin-streptavidin-biotin bonds form at the droplet-droplet contacts (middle row) until they enrich into clear adhesive patches with an increased fluorescence signal, allowing to isolate them through image analysis (bottom row). Note that the formation of the patches depletes the fluorescence level on the free edge of the droplets making it appear more red over time.

and considerably reduces photo damage. For our experiments, we use two laser configurations: red (excitation wavelength 555 nm, emission wavelength 594 nm) and green (excitation wavelength 470 nm, emission wavelength 488 nm). We use three objectives: 10X (Nikon CFI Plan Fluor), 20X and 60X (both Nikon CFI PLAN APO LBDA).

2.4 Image analysis

The general steps of the image analysis that we perform are the following. First, the images are segmented to find the center and contour of each droplet in the channel. From this data, a surface Voronoi tessellation is then performed. Voronoi tessellation is a partition of a plane into regions around a given set of objects (droplets in our case), such that any point inside the region is closer to the inclosed object than to any other. This allows to attribute a cell to each droplet, thus defining its neighbors. Then, we measure the deformation of each droplet, as well as their local or global packing fractions. Finally, we track droplets over time to analyze the rearrangements topology and local dynamics of the droplets. Below, I describe the image analysis in details.

2.4.1 Segmentation and Voronoi tesselation

Raw images are either segmented using Ilastic [10] or a custommade Matlab (MathWorks, USA) routine.

In the first case, background and foreground pixels are determined using the pixel classification feature of Ilastik. To this end, the droplet border is detected on fluorescent images by manually identifying background and foreground until Ilastik can successfully detect the contour of droplets. The obtained binarized images are then processed in Fiji to skeletonize the contour (*see* Fig. 2.5E). Using the module Analyze Particles, we identify all the droplets and exclude those touching the borders of the channel. The binarized images obtained from Ilastik are additionally processed in Fiji to perform a surface Voronoi tessellation. First, we generate binary masks of the identified droplets. A surface Voronoi tessellation is then performed on these masks to identify the Voronoi cells corresponding to each droplet (*see* Fig. 2.5F). Voronoi cells are finally matched to their corresponding droplets based on the coordinates of their centres.

Alternatively, using the Matlab routine, the images are first thresholded based on their intensity histograms. After thresholded images are cleaned up using morphological operations, droplet centres taken as their centroids are found using the Matlab "regionprops" function (*see* Fig. 2.5A-C). We then find edges of each droplet and smooth them with a Savitzky-Golay sliding polynomial filter (*see* Fig. 2.6A). To attribute a cell to each droplet, we perform a watershed tessellation (a transformation in image analysis analogous to Voronoi tessellation, that allows to divide adjacent "basins" into separate regions).

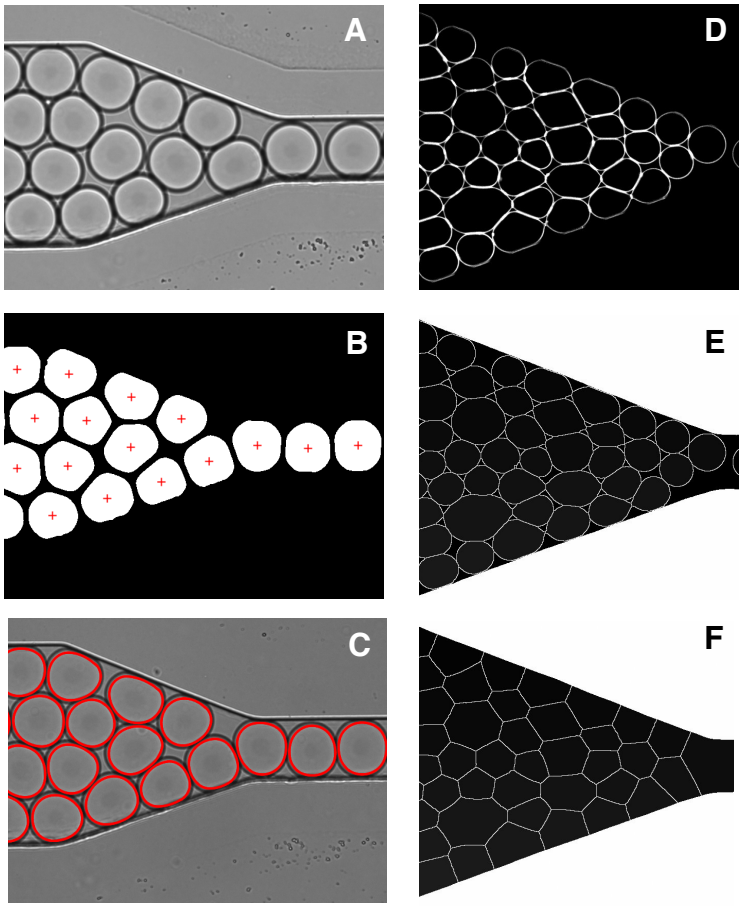

Figure 2.5 | **Image analysis** (A) Typical bright field image of monodisperse droplets in the constriction area. (B) Segmented image of (A) with the detected centres of the droplets (red crosses). (C) Detected contours of the droplets. (D) Typical fluorescent image of polydisperse droplets in the constriction area. (E) Detected droplets from (C). (F) Voronoi cells of the droplets on (C).

2.4.2 Droplet neighbors identification and tracking

A table of neighboring relationships between droplets and Voronoi cells is generated using the Region Adjacency Graphs of the Python Scikit-image package. For every image, we obtain the list of neighbors for each droplet and each Voronoi cell in the constriction and measure the size of the droplet-droplet contacts as well as the length of the edge between neighboring Voronoi cells. The droplets and Voronoi cells are tracked on the labelled movie with a custom Python tracking algorithm and the FastTrack tracking software [59], and instant velocities of droplets and Voronoi cells are computed as the distance travelled between two consecutive frames acquired at a fixed frame rate.

2.4.3 Droplet deformation and packing fraction

To study droplet deformation, we consider only the droplets located in the constriction area (*see* Fig. 2.4. In addition, while analyzing the images of the bigger channel, we exclude the droplets whose corresponding Voronoi cells touch the walls of the channel. We use two different methods to measure droplet deformation.

For the first approach, we have followed Chen *et al.* [31] (*see* Fig. 2.6B). To this end, the perimeter of each droplet is interpolated and discretized using a custom Matlab routine at evenly spaced 1024 angles θ and the deformation d is calculated as a standard deviation of the radii $r(\theta)$ taken from the droplet center (see Fig. 2.6) for each of these angles divided by the mean value of r:

$$d = \frac{\sqrt{\langle r^2 \rangle - \langle r \rangle^2}}{\langle r \rangle} \tag{2.1}$$

The other way to quantify droplet deformation is to compute a shape factor $\mathcal{A} = p^2/4\pi a$, as it was done by Boromand *et al.* [18]. The shape parameter $\mathcal{A}$ equals 1 for disks and is greater than 1 for all nonspherical particles [19]. To avoid overestimating $\mathcal{A}$ because of finite image resolution (*i.e.* finite number of pixels), we fit successions of osculating arcs of circles around the droplet contours. To do so, we divide the contour in groups of 12 points. On each group, we compute the coordinates of the center and radius of the circle going through the first, sixth and twelfth points of the group, as a good approximation of the osculating circle at this part of the contour. We then model the contour of the droplet as a succession of such arcs, and compute its perimeter p and area a from the modelled contour. To check the accuracy of the fitted contours, we apply our custom fitting routine to an image of synthetic perfect circles. As shown on Fig. 2.5C, the shape parameter obtained from this model yields 1.0009 ± 0.0003, which validates our analysis on real droplets.

To complete the study of droplet deformation, we also fit each droplet with an ellipse, and use its aspect ratio and orientation of the major axis to study elongation and alignment of the droplets in the constriction.

Finally, we compute the local and global packing fractions of the droplets in the constriction area. We define the local packing fraction for each droplet as $\phi_l = a/a_c$, where a is the area of the droplet and a_c is the area of corresponding Voronoi cell. Note that to study the deformation, we only consider droplets whose local packing fraction lies in $\phi_l \in \{0.6; 1\}$, which allows us to eliminate overlapping or missing droplets resulting from segmentation mistakes. To determine the global packing fraction of the emulsion in each video frame, we calculate the ratio between the sum of all droplets area and the area of the channel within the window of 200×200 μm located before the constriction region (*see* Fig. 2.4A). Finally, frames were stored according to the emulsion packing fraction, and the distributions of droplet deformations for each packing fraction were computed.

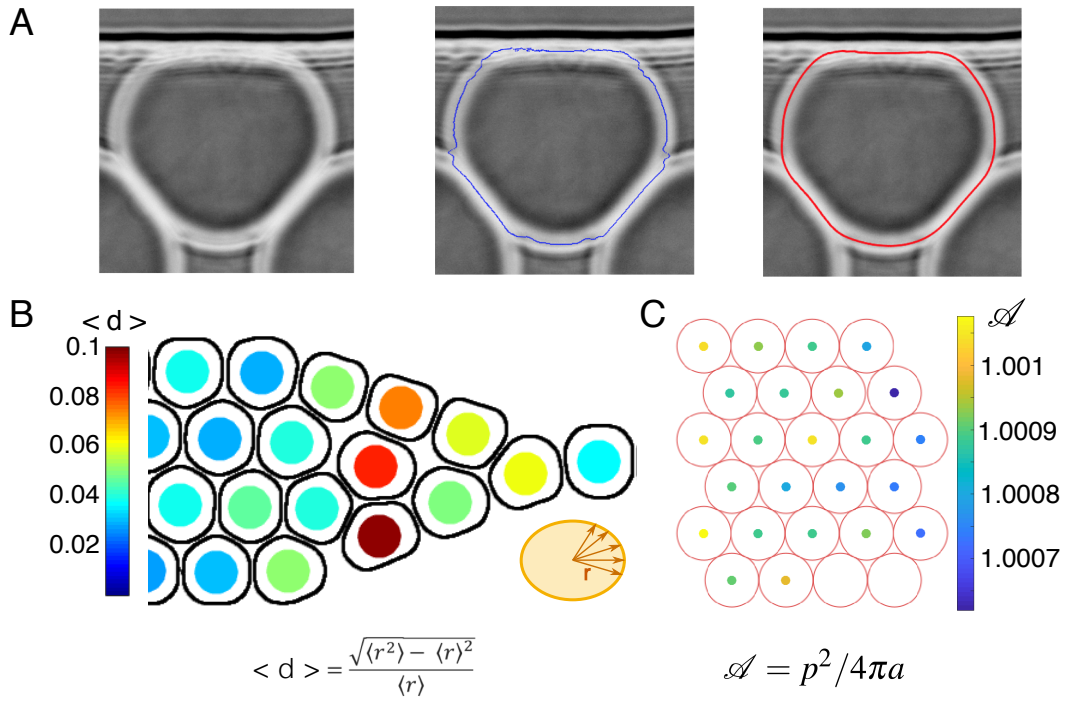

Figure 2.6 | **Droplet deformation.** (A) Detected contour of an individual droplet (left) before smoothing (middle) and after smoothing (right). (B) Still snapshot of the image analysis in the channel at a given instant for monodisperse droplets. Detected droplet contours are plotted in black, and deformation d of each droplet is shown as a colorcode. (C) Shape factor $\mathcal{A}$ (color coded) of synthetic ideal circles.

2.4.4 T1 events detection

By tracking droplets and their neighbors over time, we identify the formation or rupture of edges between Voronoi cells. This allows us to identify individual T1 events by considering the neighborhood of droplet quadruplets as shown in Fig. 2.7C. To eliminate artifacts from contacts or edges disappearing or appearing from pixel fluctuations, we take into account Voronoi cell edges that are not transient and that can thus be detected for at least 4 consecutive frames. Contacts or edges appearing or disappearing because one of the two objects enters or leaves the field of view are also discarded. A manual inspection of T1 events detected this way shows that only 2% of the detected events are not true T1 events. Of those false T1 events, half of them are caused by segmentation errors, and the other half by exotic 5-cells exchanges of neighbors.

We then examine avalanche phenomena by considering T1 events that occur during a given time window and that are connected by neighboring droplets. To do so, we define an adimensional time $t = t^* \langle V \rangle / \langle R \rangle$ with t^* the elapsed time in seconds, $\langle V \rangle$ the mean flow velocity and $\langle R \rangle$ the mean radius of droplets that are both averaged over all droplets in all frames of each movie. We define clusters of events, called avalanches, as neighboring T1 events within a specified time window $t \pm \Delta t$, where $\Delta t = 0.4$ in adimensional time (which is the time necessary for a droplet to travel 40% of its radius on average). This time window is chosen to span avalanche sizes ranging

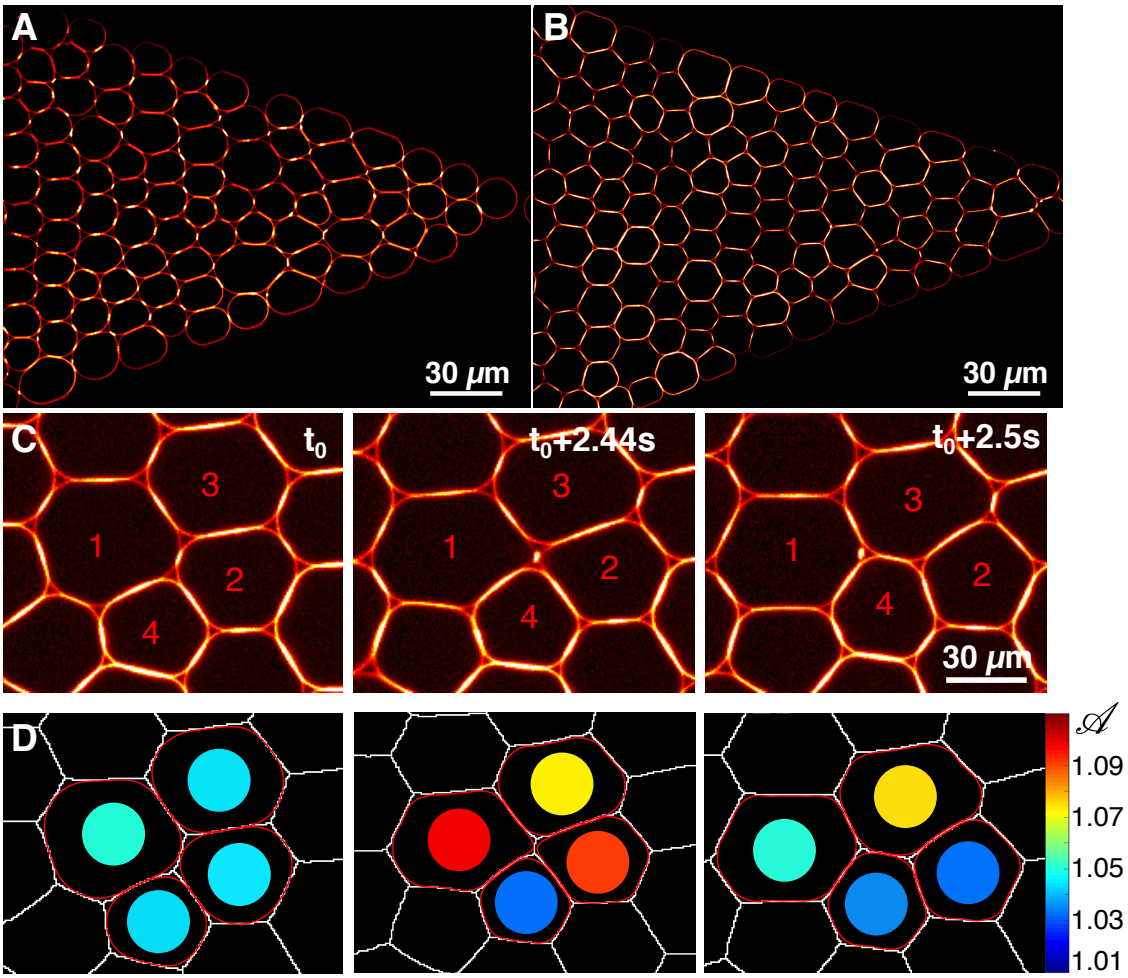

Figure 2.7 | **Confocal imaging and analysis.** (A-B) Confocal images of two different packing fractions of an adhesive emulsion in the constriction. (C) Confocal images of four adhesive droplets undergoing a T1 event. Droplets 1 and 2 are first connected through an adhesive patch (left panel), are then pulled apart (middle panel) and are not neighbors anymore (right panel). In the meantime droplets 3 and 4 gain a contact at the end of the event. (D) Result of the image analysis performed on (C). Voronoi cells are drawn in white solid lines, droplet contours are shown in red and the color of the disk inside each droplet codes for its deformation $\mathcal{A}$.

from one T1 event to all the droplets contained in the field of view, thus guaranteeing that the avalanches are not too big nor too small within that chosen window. The distribution of T1 events into separate clusters (*i.e.* avalanches) is the following. First, for each T1 event, we make the list of all the Voronoi cells that are adjacent to one of the 4 cells of the current T1 at any time point between $t - \Delta t$ and $t + \Delta t$. We then make a list of all the T1 events in which those neighboring cells are involved within the time window, and get their cluster identification number (id). If none of the T1 events is already allocated to a cluster id, then a new cluster id is created and given to all the connected T1 events. If all the T1 events have a unique common cluster id, then this id is assigned to the current T1 event. If the T1 events have more than one cluster id, the current T1 event and all connected T1 events are then assigned the smallest of the cluster ids of the list. We quantify avalanche sizes by measuring the total number of droplets participating in the same

avalanche *i.e.* with the same cluster id.

Chapter 3

The impact of adhesion on flowing biomimetic emulsions

Если долго мучиться, что-нибудь получится.[a]
Народная мудрость

[a] If at first you don't succeed try, try and try again.

In my PhD work, I did study the mechanical pathways of morphogenesis with biomimetic emulsions: droplets of oil in water stabilized with a monolayer of phospholipids that mimics the fluid cellular membrane, and functionalized with binding molecules which ensure specific adhesion between the droplets. In this chapter, I am going to describe how we study tissue remodelling under controlled mechanical perturbations *in vitro*.

As it was explained in Chapter 1, during development, tissues undergo large scale movements that shape the different organs in the embryo. To unravel the passive mechanical pathways associated with this process, we developed a simplified system where we exert a large-scale perturbation on biomimetic emulsions by forcing them to flow through microfluidic constrictions. In this way, we mimic the convergent extension that tissues undergo during morphogenesis. In order to go through the constriction, droplets have to elongate along the axis of the channel (elastic response) or rearrange their positions in order to go through the thinner channel (plastic response). We studied the interplay between the elastic and plastic responses as a function of the adhesion energy between the droplets and the packing fraction of the emulsion.

First, we performed a preliminary study as a proof of concept and probed the effect of attraction forces between the droplets. The easiest way to do so is to introduce interdroplet attraction with non-specific depletion forces. The details of this study and the obtained results are given in the first part of this chapter.

In the second part of this chapter, I present the study where we used a system that mimics biological tissues more faithfully. In this system, a specific adhesion is introduced through streptavidin-biotin-streptavidin bonds between the surfaces of the droplets, which mimics cadherin cellular adhesion.

3.1 Depletion attraction forces to introduce non-specific adhesion between the droplets

Depletion forces appear between particles or emulsion droplets that are surrounded by much smaller particles called depletants, that can be surfactant micelles, colloids or non-adsorbing polymer molecules. A schematic representation of what causes depletion attraction is shown on Fig. 3.1: when two droplets of radius R and surrounding depletion zone of thickness δ approach each other, micelles start to be expelled from the inter-droplet region into the outer continuous phase. This happens when the interdroplet distance a is smaller than $2(r_m + \delta)$, where r_m is the radius of the depletants [15]. This leads to an osmotic pressure difference between the surrounding continuous phase and the empty excluded inter-droplet region. As a result, depletion forces are exerted on the droplets to fill the excluded volume thus creating an attractive interaction between their surfaces. Depletion forces are therefore short range forces that appear only between neighboring droplets.

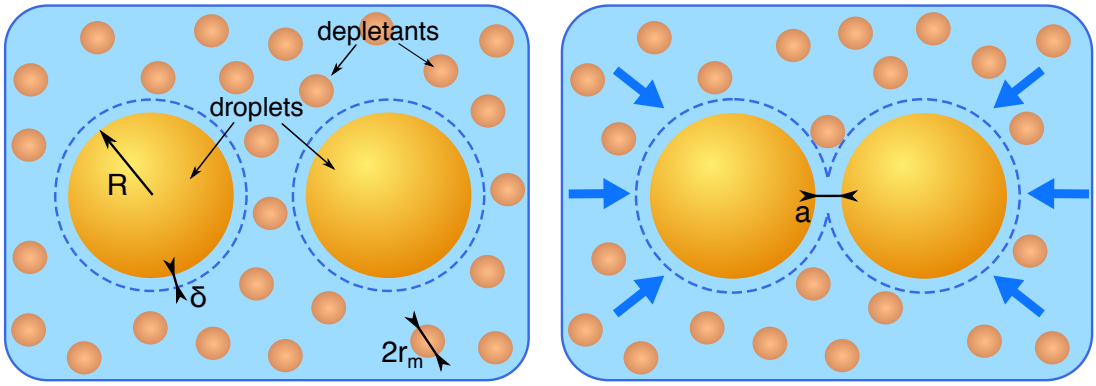

Figure 3.1 | **Schematic representation of an attractive interaction between colloidal particles induced by depletion forces.** Depletion attraction forces (blue arrows) appear when two particles with radius R and surrounding depletion zone δ approach each other such that depletants with radius $r_m < R$ start to be excluded from the inter-droplet region.

In our experiments, depletion attraction between the droplets is introduced by increasing the concentration of SDS in the continuous phase of the emulsions. When the concentration of SDS exceeds the critical micellar concentration (CMC), its molecules arrange to form micelles that act as depleting agents. Asakura *et al.* [5] showed that, above the CMC, depletion attraction forces P between two large particles of diameter R and interparticle distance a increase linearly with the number of micelles N of diameter r_m present in the continuous phase, and can be calculated as

$$P = -p_0 S, \tag{3.1}$$

where p_0 is the osmotic pressure

$$p_0 = kTN/V \tag{3.2}$$

with kT being the thermal energy (k = Boltzmann constant, T = temperature), V the total volume

of the solution and S a geometrical parameter defined as

$$S = \frac{\pi}{4}[(R + r_m)^2 - a^2] \tag{3.3}$$

In this way, increasing the concentration of SDS leads to the increase of the number of micelles, and thus to higher attraction forces between the droplets.

In our experiments, the continuous aqueous phase is supplemented with glycerol (40 % in volume of glycerol, *see* Chapter 2), which shifts the CMC of SDS from 8 mM (in pure water) to about 9 mM in our experimental conditions [145, 90]. Thus, under both SDS concentrations that we use, namely 10 mM and 45 mM, the system is still above the CMC, and the surface tension of droplets remains the same at both SDS concentrations [91]. However, the number of micelles is not necessarily linear with the SDS concentration. Indeed, the number of surfactant molecules in one micelle, which is also called the aggregation number, can grow with the concentration [16]. For SDS, this number has been reported by various authors and yields different values. We calculated the number of micelles based on the reported aggregation numbers, and estimated that attractive forces at 45 mM SDS are approximately 30 times larger then at 10 mM SDS. The details of our calculations can be found in the attached article A.

Similarly to granular materials, emulsions exhibit a jamming liquid-to-solid transition, which depends on the global packing fraction ϕ of the emulsion. And similarly to granular materials, the jamming in athermal (*i.e.* those that do not exhibit Brownian motion) repulsive monodisperse emulsions in 3D occurs at $\phi_j = \phi_{RCP} \approx 0.64$. Jammed emulsions behave as amorphous solids and possess a yield stress. They elastically (reversibly) support a finite stress below this yield stress, and deform irreversibly, *i.e.* start to flow, if the applied stress exceeds this yield stress[113]. However, in stark contrast to the repulsive emulsions, attractive emulsions can form an elastic solid even well below jamming [114]. For example, Datta *et al.* [37] showed that depletion attraction interactions between the droplets were sufficient to change the rheological properties of thermal (*i.e.* brownian) emulsions. To this end, they applied a shear stress on both repulsive and attractive emulsions and measured their viscoelastic response. They found that while repulsive emulsion possessed a yield stress only for $\phi \geqslant \phi_{RCP}$, attractive emulsions could support the stress even for $\phi < \phi_{\mathrm{RCP}}$. This result suggests that attractive interactions between the droplets lead to the formation of a connected network of droplets that can support a shear stress. In addition, Datta *et al.* showed that attractive emulsions above jamming exhibited an extra relaxation process before starting to flow; however, the microscopic nature of this process remained unclear. Therefore, even though the effect of interdroplet attraction on the rheological properties of emulsions has been macroscopically evidenced, its microscopic origin is still unknown.

The effect of attraction at a microscopic level was partially exhibited by Jorjadze *et al.* [83] on 3D packings of polydisperse athermal oil droplets stabilized with SDS. These packings were formed under gravity. As silicone oil droplets have a smaller density compared to water, they pack at the air/water interface by buoyancy (a process called creaming), and form jammed structures. By varying the concentration of SDS, Jorjadze *et al.* probed how their structural properties depended on the average amplitude $\langle F_d \rangle$ of the attractive interdroplet forces. They measured their packing

fraction ϕ, as well as the average contact number $\langle z \rangle$ (the number of contacts a particle has), and found that depletion attraction stabilized the packings below the isostatic limit, *i.e.* $\phi < \phi_{RCP}$ and $\langle z \rangle < 6$ (*see* Fig. 3.2).

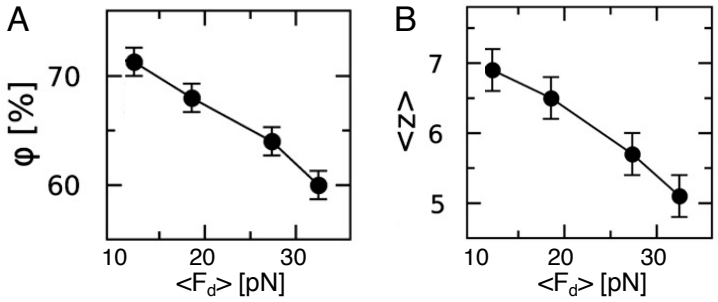

Figure 3.2 | **Effect of depletion attraction on the structural properties of emulsions.** Packing fraction ϕ (A) and average coordination number $\langle z \rangle$ (B) decay as a function of $\langle F_d \rangle$ below the isostatic value. Adapted from [83].

To further investigate the effect of attractive forces between the droplets on the structural properties of emulsion packings, we study the behaviour of compressed attractive and repulsive emulsions in 2D in both static and dynamic conditions.

3.1.1 Effect of depletion attraction on 2D static packings

Several experimental studies on compressed foams and repulsive emulsions [39, 87] revealed that their structural and mechanical properties, such as the shear modulus or the contact number, displayed a power-law scaling with the distance to the jamming onset expressed in terms of packing fraction as $(\phi - \phi_j)$. Boromand *et al.* [19, 18] performed computational studies of jammed packings of soft frictionless particles undergoing an isotropic compression. They developed a numerical model to study the structural and mechanical properties of 2D bubbles and emulsions, including at high compression. This model will be described in detail in the Section 3.2.3. Using this model, Boromand *et al.* developed a theoretical framework for the evolution of the shape factor $\mathcal{A}$ of the particles as a function of local packing fraction close to the jamming onset. They defined the shape factor $\mathcal{A}$ as

$$\mathcal{A} = \frac{p^2}{4\pi a} \tag{3.4}$$

where p and a are the droplet perimeter and area respectively. The shape factor $\mathcal{A}$ is a direct measure of asphericity of the droplets. Indeed, it is equal to 1 for a perfect disk and is greater than 1 for any non-spherical particle. Boromand *et al.* predicted that for polydisperse disordered packings, the distance to the jamming onset $\phi - \phi_j$ scaled with $\mathcal{A} - 1$ as

$$\phi_l - \phi_j = \alpha(\mathcal{A} - 1)^{\omega} \tag{3.5}$$

with $\omega \approx 0.3$ (*see* Fig. 3.4A).

We checked if attractive interactions induced by depletion affected this power law scaling.

Following Boromand *et al.* we measured the asphericity $\mathcal{A}$ and the local packing fraction ϕ_l of each droplet in several images of 2D monodisperse and polydisperse packings for both 10 and 45 mM SDS concentrations (*see* Chapter 2). Examples of such monodisperse and polydisperse packings are shown in Fig. 3.3.

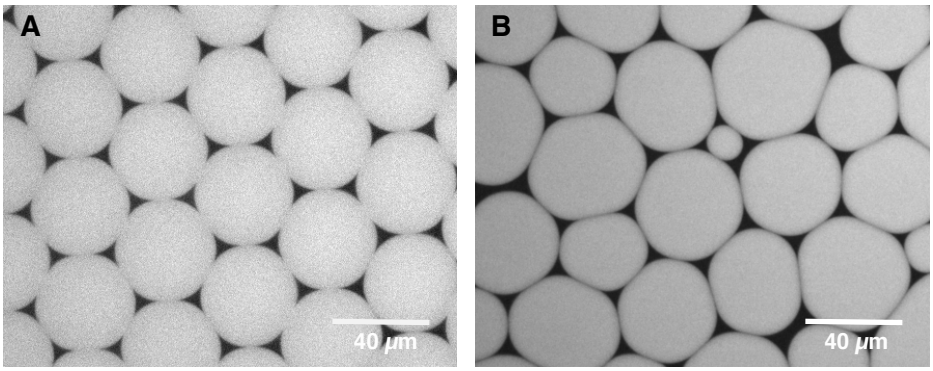

Figure 3.3 | **Examples of a monodisperse (A) and a polydisperse (B) emulsion packing.** Droplets are labeled with Nile Red. ([SDS] = 10 mM)

Fixing $\omega = 0.33$ and $\phi_j = 0.842$ (random close packing of disks in 2D), we found that indeed our data of polydisperse repulsive emulsions are well-fitted by Eq. 3.5 (*see* Fig 3.4B). If we fix only the prefactor α letting ω and ϕ_j free, we still found similar values for $\omega = 0.36$ and $\phi_j = 0.848$. All performed fits are summarized in Table. 3.1.

[SDS]	Fixed parameters	Free parameters
10mM	$\omega = 0.33$ $\phi_j = 0.842$	$\alpha = 0.26$
	$\alpha = 0.26$	$\omega = 0.36 \pm 0.1$ $\phi_j = 0.848 \pm 0.02$
	$\omega = 0.33$	$\alpha = 0.23 \pm 0.06$ $\phi_j = 0.846 \pm 0.012$
	$\phi_j = 0.842$	$\omega = 0.29 \pm 0.09$ $\alpha = 0.21 \pm 0.09$
45mM	$\omega = 0.33$ $\phi_j = 0.842$	$\alpha = 0.28$
	$\alpha = 0.28$	$\omega = 0.37 \pm 0.08$ $\phi_j = 0.85 \pm 0.013$
	$\omega = 0.33$	$\alpha = 0.24 \pm 0.05$ $\phi_j = 0.849 \pm 0.01$
	$\phi_j = 0.842$	$\omega = 0.28 \pm 0.06$ $\alpha = 0.21 \pm 0.06$

Table 3.1 | List of all fitting parameters obtained for various fixed parameters applied to the deformable particle model equation 3.5.

Moreover, even though the model was developped for polydisperse disordered packings, we also found that the change in the local packing fraction as a function of the droplet deformation in monodisperse repulsive emulsions is well described by the power law scaling of Eq.3.5. In this case a scaling exponent $\omega \approx 0.25$ and a critical volume fraction $\phi_j = 0.91$ are found. The higher

value for ϕ_j can be explained by a high degree of crystallization, as seen on Fig. 3.3A. Indeed, the obtained value of ϕ_j corresponds to the one of hexagonal close packings $\phi_{\mathrm{HCP}} = 0.91$. The results of these scalings are shown on a log-log scale in Fig. 3.4.

Surprisingly, we find that the data for the repulsive ([SDS] = 10mM) and the attractive ([SDS] = 45mM) emulsions overlap and are captured by the same scaling function in the case of both polydisperse and monodisperse emulsions. Therefore, our experiments indicate that depletion interactions between the droplets do not affect significantly the scaling of $\phi_l - \phi_j$ *vs* $\mathcal{A} - 1$, *i.e.* changing the SDS concentration does not induce any measurable modification in the static packings of droplets.

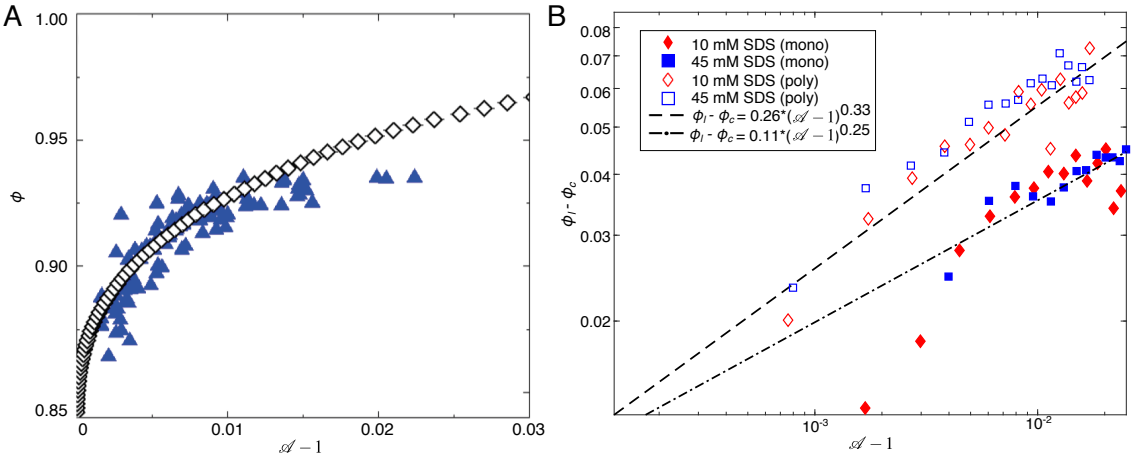

Figure 3.4 | **Analysis of static 2D packings.** (A) Local packing fraction ϕ versus $\mathcal{A} - 1$ for the DP model (open diamonds) and emulsions droplets (filled triangles). Adapted from [18]. (B) Log-log plot of $\phi_l - \phi_c$ versus $\mathcal{A} - 1$ for monodisperse and polydisperse emulsions for both SDS concentrations.

In contrast to the results of Datta *et al.* [37] and Jorjadze *et al.* [83], who found that depletion attraction stabilizes looser 3D packings, we do not observe any significant change in ϕ_j for 2D static packings with depletion interactions. In our SDS stabilized emulsions, the droplets are essentially frictionless and are thus free to move. In addition, as we explore packing fractions above jamming, the droplets are compressed. In such a system, the slightest amount of compression will thus lead to a rearrangement of the structure without noticeable deformation of the droplets until their repulsive jamming packing fraction is reached. This intuition is confirmed by the measured values of ϕ_j which correspond to random close packing $\phi_{\mathrm{RCP}} \approx 0.842$ for the polydisperse (disordered) emulsions and to hexagonal close packing $\phi_{\mathrm{HCP}} = 0.91$ for the monodisperse emulsions.

However, despite the fact that static packings cannot be distinguished as a function of depletion forces, these forces still can have an effect on the mechanical properties of the emulsion. We reveal in what follows that significantly distinct behaviors can be evidenced in the context of a dynamic flow.

3.1.2 Emulsion flow in a constriction

In order to study the effect of depletion attraction on the emulsion response to a mechanical perturbation, monodisperse emulsions were flowed in microfluidic channels exhibiting a single physical constriction (*see* Chapter 2, Fig. 2.4A). Here, we used monodisperse droplets whose diameter is comparable to the channel height, constraining the system to a 2D monolayer of droplets. We chose to flow monodisperse emulsions, because their packing and flow is ordered (the details will be explained later), and one could expect that the effect of the attraction forces would be best seen with the order breaking. We focused our analysis on the area of the constriction in which droplets have to rearrange and deform in order to go from a large channel into a narrower one. The width of the narrow channel was chosen such that it only allows for the passage of one droplet at a time (Fig. 2.4A) in order to maximize the number of rearrangements.

Even though the emulsions are frictionless, we observed some interactions (probably of wetting nature) between the droplets and the surface of the channel. Passivation of the channel with a β-casein solution prior to the emulsion flow (*see* Chapter 2) minimized all the interactions between the droplets and the channel thus establishing a smooth flow.

A typical experiment was carried out in two phases. The channel is first filled with the emulsion using a pressure pump. After a waiting time (*see* Chapter 2), the pressure is increased again so that the packed emulsion can flow in the channel. We usually require a typical pressure of the order of 30 mbar to establish a steady flow. For each experiment, we recorded images of the droplets upstream, in order to measure their packing fraction, as well as inside the constriction, where we study droplet deformation and rearrangements (Fig. 3.5).

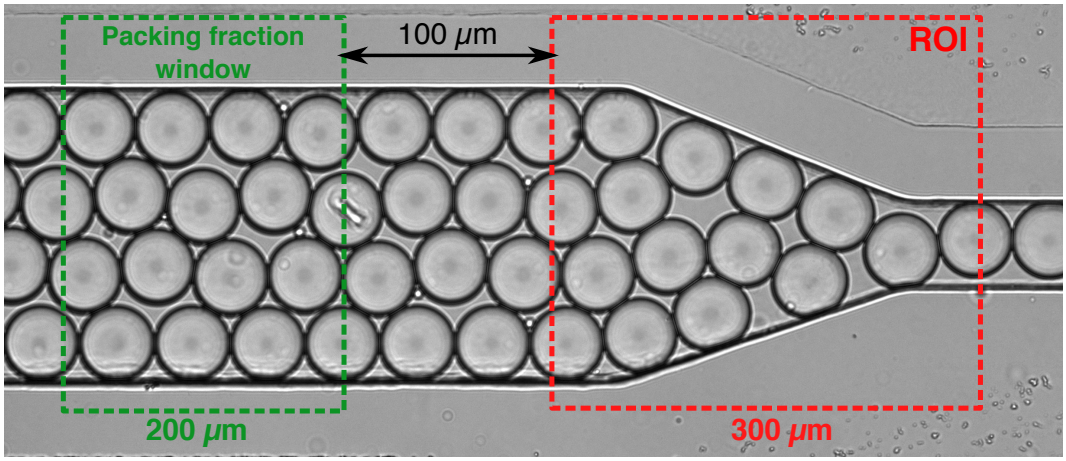

Figure 3.5 | **Emulsion flowing in the constriction.** Droplet deformation is studied inside the constriction (red window), while packing fraction is measured in the green window upstream of the constriction ([SDS] = 45 mM).

3.1.3 Global packing fraction

We measured the global packing fraction of the emulsion for each frame in a window located upstream of the constriction (*see* Chapter 2 and Fig. 3.5). We found that the packing fraction varied over the course of one experiment. It happened due to temporal irregularities of the flow, which could be caused by partial plugs at the inlet of the channel. Therefore, to check the effect of packing fraction on droplet deformation, we break each experimental video into separated images, and measure the packing fraction for each image. We sorted our experiments into seven bins with the average packing fractions span from 95.5% to 97.0%. We then pool together the images corresponding to the same packing fraction throughout all performed experiments, for each concentration. For all of the following measurements we keep this sorting of our data based on packing fractions.

3.1.4 Effect of the depletion attraction on droplet deformation

We first studied the effect of attraction forces on droplet deformations. As it was explained in Chapter 2, we define the droplet deformation d as the standard deviation of the radius $r(\theta)$ following Chen et al. [31] :

$$d = \frac{\sqrt{\langle r^2 \rangle - \langle r \rangle^2}}{\langle r \rangle} \tag{3.6}$$

We chose to use d as a measurement of the droplet deformation, and not $\mathcal{A}$ as it was done for the static packings, because the calculation of d requires less computational work than the calculation of $\mathcal{A}$. Indeed, a value of the shape factor $\mathcal{A}$ relies on the precise calculation of peremeter of the droplets. To calculate the perimeter properly, one needs to find the contour and then fit it (*see* Chapter 2), which is computationally costly. As the analysis of flowing emulsions requires quantifying deformation on a much larger amount of droplets, we thus chose a parameter that is easier to compute on such a large amount of data.

We measured d for all droplets inside the constriction region (Fig. 3.5). The obtained distributions of the measured deformations for different packing fractions and for each SDS concentration are shown in Fig.3.6. At all packing fractions we investigated, the distributions peak at smaller values of the deformation for the low attractive case compared to the case of strongly attractive droplets. However, we do not see any significant differences with the packing fractions. Indeed, in the case of high attraction, the curves for different packing fractions clearly collapse on each other. In the case of low attraction, some difference in the height of the peak can be observed, with lower packing fractions having slightly higher peak values than high packing fractions (blue curves in Fig. 3.5). However, this difference remains small and prevents us from drawing any conclusions.

In order to study in more details the observed shift in the deformation distributions, we next examined the droplet deformation field along the channel. To this end, we measured deformation

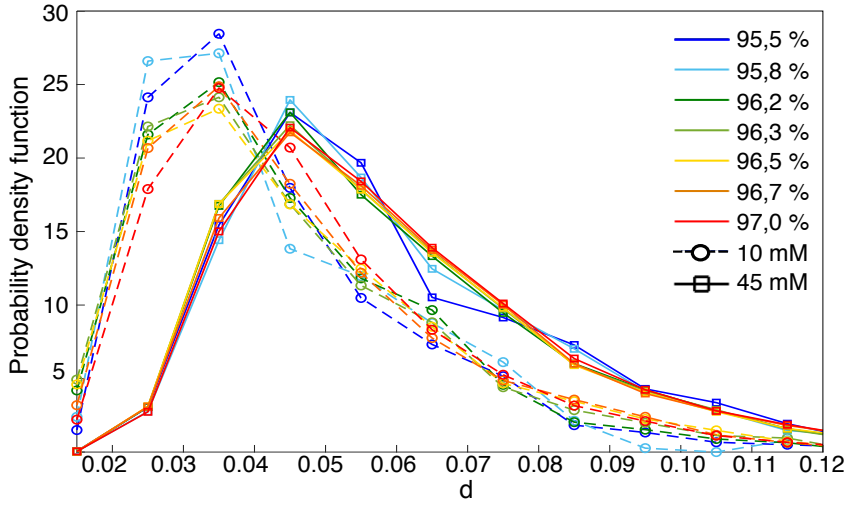

Figure 3.6 | **Statistics of deformation under steady flow.** Probability density function of the deformation d calculated in the constriction for different packing fractions in the case of low attraction forces ([SDS] = 10 mM, open circles) and high attraction forces ([SDS] = 45 mM, open squares).

d of all droplets filling the channel in the field of view. An example of such measurements is shown in Fig. 3.7A. In order to study the deformation along the x-axis of the channel, we divided the channel into bins of 25 μm wide, a width which corresponds to the average droplet radius, and measured the average droplet deformation inside the bins. The resulting curves of $\langle d \rangle$ versus x are shown in Fig. 3.7B-C. We did it for both concentrations of SDS in order to study the effect of the attractive forces. One would expect the droplets to be more deformed in the constriction region, as they are subjected to the external compression. And indeed, droplets that are in the constriction region have higher values of $\langle d \rangle$ compared to the droplets out of the constriction for both 10 mM and 45 mM SDS concentration and for all packing fractions. This validates the chosen method for measuring deformations in our system.

Although the general shape of the obtained curves is similar for both SDS concentrations, the values of deformations are higher at a 45 mM SDS concentration both in the constriction region and in the thinner channel. For both conditions (Fig. 3.7B-C), the average deformation builds up in the constriction to a first maximum, then decreases to a lower value at $x \approx 450\ \mu m$, builds up again to a second maximum and finally decreases to a lower average value.

The observed averaged deformation field inside the constriction - accumulation of the deformation followed by its release - can be a signature of a local stress release after two sequential rearrangements of the droplets (for instance, T1 events). Indeed, in soft jammed materials under strain, only a small subset of particles support most of the load, forming so-called stress networks [30, 26, 175], which leads to complex rearrangements of the particles and stress relaxation. In jammed emulsions, droplet rearrangements happen through T1 events (exchange of neighbors in a group of 4 droplets). Chen *et al.* [31] showed that in the case of a 2D repulsive emulsion flowing through a hopper shaped chamber, T1 events were immediately followed by a local decrease of

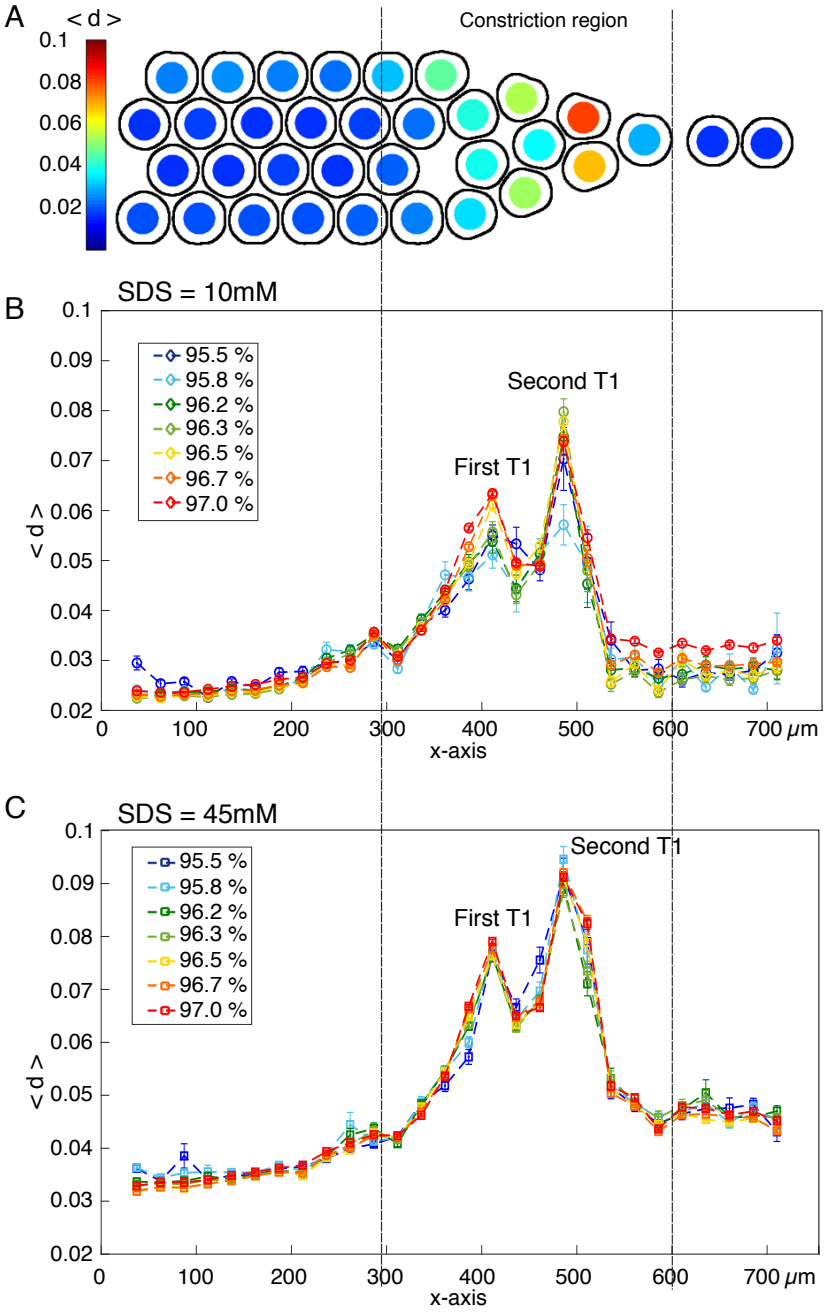

Figure 3.7 | (A) Still snapshot of the image analysis in the channel at a given instant for an attractive emulsion ([SDS]=45mM). The color of the droplets codes for their deformation d calculated for their detected contours displayed on the image. (B-C) Average deformation of the droplets along the x-axis of the channel for different packing fractions in (B) the low attraction case ([SDS]=10mM) and (C) high attraction case ([SDS]=45mM). The deformation is averaged in bins that are 25 μm wide along the x-axis, corresponding to about droplet radius. The average deformation peaks inside the area of the constriction for both conditions. The error bars correspond to the standard error of the mean for the distributions of d obtained in each bin. The total number of droplets, combining all packing fractions, is N = 27219 for 10mM SDS and N = 91391 for 45 mM SDS.

droplet deformation d inside the emulsions (d is defined in the same way as in our experiments). To study the effect of T1s on droplet deformation, Chen *et al.* computed a spatial-temporal map, which represents the relative deformation of individual droplets around the T1 event (Fig. 3.8A). The map shows that local deformations first build up prior to a T1 event (red), and then drop dramatically after the T1 event (blue). The biggest decrease in deformation after a T1 event (the blue region which splits in two), corresponds to the converging and diverging pairs of the droplets that have undergone the rearrangement (Fig. 3.8A).

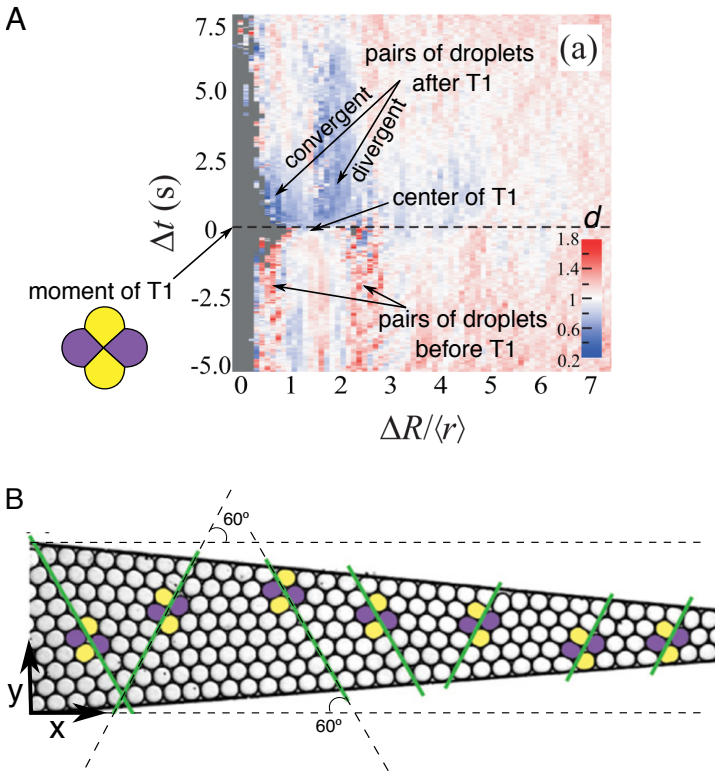

Figure 3.8 | (A) Spatial-temporal map of the local deformation d around a T1 event. $\Delta t = 0$ is the moment when the T1 event occurs, indicated by the horizontal dashed line. ΔR is the distance from the center of the T1 event ($\Delta R = 0$) normalized by the average droplet radius $\langle r \rangle$. The color indicates the mean magnitude of the deformation d of individual droplets compared to the global mean (white color). Smaller values ($d < \langle d_G \rangle$) are blue and larger values ($d > \langle d_G \rangle$) are red. Adapted from [31]. (B) Spatial distribution of dislocations and slip planes throughout the channel. The slip planes are indicated by the green lines. The dislocations and corresponding droplet pairs during T1 events are colored in yellow and purple. Adapted from [58].

Similar effects are thus probably observed in our experiments (*see* Fig. 3.7). The droplet deformation increases up to its peak value, and then it is partially releazed by a first T1 event. This first release happens in the middle of the constriction region (x $\sim$ 450μm). As the width of the constriction continues to reduce, the droplet deformation increases again, until finally it is releazed at the exit of the constriction by the second T1 event. However, while in the case of low depletion forces ([SDS] = 10 mM), droplets relax to a deformation value that is close to the initial one at the entry of the channel ($(\langle d \rangle_{out} - \langle d \rangle_{in} \approx 0.0025)$), with high depletion forces ([SDS] = 45 mM), droplets relax to a plateau at higher values of deformation than at the entry

($(\langle d \rangle_{out} - \langle d \rangle_{in} \approx 0.01)$). This impaired relaxation could be a signature of long range effects that could also explain why droplets enter the constriction with a slightly higher value of deformation in the high attraction case.

The existence of two peaks of deformation observed in the constriction region indicates that T1 events occur at precise locations. These locations are actually set by the geometry of the channel, as it was shown by Gai *et al.* [58]. Indeed, they found that for a flow of a quasi-2D packed monodisperse emulsion in a tapered microfluidic channel, T1 rearrangements happened along slip planes and zones, where the number of droplets in the y-direction decreased by 1, occurred at well-defined regions. By making an analogy to crystal plasticity during extrusion, Gai *et al.* predicted that slip planes along which T1 events occurred, should form a 60° angle with respect to the x-axis. This is what they actually measured in their experiments. They also evidenced that the slip zones were distributed periodically along the channel (Fig. 3.8B). This periodicity could be explained using a model of crystal grain boundaries and was set by the channel geometry and size of the droplets.

Since we flow monodisperse emulsions and since the dimensions of the channel are fixed, we obtain an "ordered" flow with four lines of droplets flowing in the channel ahead of the constriction, and one line of droplets in the thin channel (Fig. 3.9).

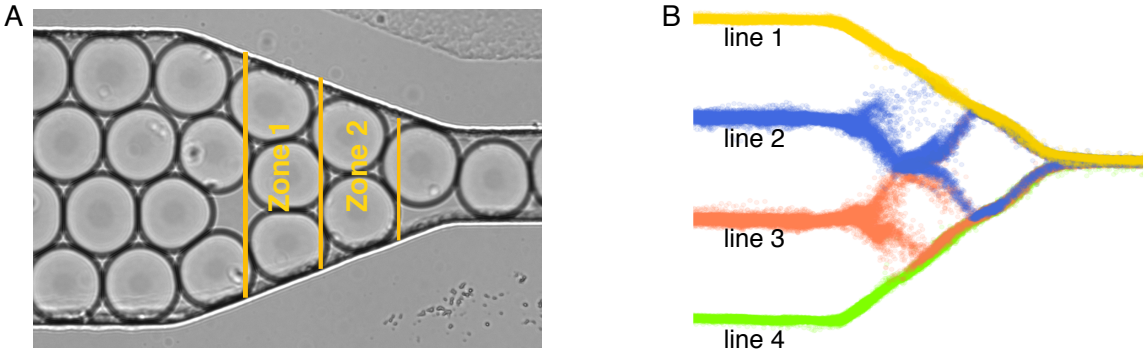

Figure 3.9 | (A) Image of droplets in the constriction ([SDS] = 10 mM). The zones where the number of droplets decreases from 4 to 3 and from 3 to 2 are indicated with yellow lines and referred to as zone 1 and 2 respectively. (B) Plotted trajectories of the droplets in lines 1-4 ([SDS] = 10 mM).

Overall, one can distinguish three locations where the number of lines of droplets decreases by one unit: from 4 to 3 droplets, from 3 to 2, and from 2 to 1 droplet at the entrance of the thin channel. In this framework, droplets should exchange neighbors to do the necessary rearrangements in given areas of the channel, that are defined by its geometry. We can thus estimate the distance Δx between two rearrangements by calculating the distance between the points where one can accommodate for 4 droplets and 3 droplets of diameter D in the constriction (Fig. 3.10). Knowing the slope of the constriction $\alpha \approx 20°$, a simple calculation leads to $\Delta x = \frac{D}{2tan(\alpha)} = 60\ \mu m$. And indeed, the distance between the two peaks observed in Fig. 3.7, $\sim 80\ \mu$m, is close to the predicted value of $\sim 60\ \mu$m.

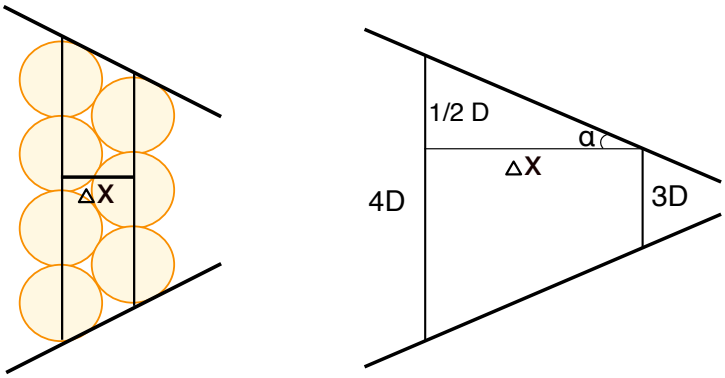

Figure 3.10 | **Distance between two T1s.** Schematic representation of a part of the channel where number of lines of droplets reduces from 4 to 3. The distance Δx between the zone of 4 droplets and the zone of 3 droplets is set by the slope of the constriction α and droplet diameter D.

We next test the hypothesis that rearrangements are impaired by the attraction between the droplets, which would in turn force the droplets to deform more to overcome the constriction.

3.1.5 Effect of depletion attraction on droplet rearrangements

While trajectories of the droplets in lines 2 and 3 are more complicated (after the rearrangement droplets can randomly go either up or down), the trajectories of droplets in lines 1 and 4 are pretty straightforward: droplets in the line 1 always go down, and droplets in line 4 always go up following the borders of the channel (*see* Fig. 3.9B). That is why we chose droplets in lines 1 and 4 to study locations of the rearrangements.

In order to determine precisely the locations of droplet rearrangement, we measured both the velocity and number of neighbors of the droplets along the channel. In the constriction, droplets are slowed down transiently until they perform a rearrangement. This effect is evidenced by local minima in their individual velocity profiles. We show in Fig. 3.11A typical velocity profiles of individual droplets in lines 1 and 4 along the channel axis for both SDS concentrations. In this example, the two local minima are separated by the expected distance between rearrangements Δx. We extract the positions of these minima for all droplets in lines 1 and 4 in two specific areas of the channel, corresponding to the zones of rearrangements, for both SDS concentrations. We compare both conditions by plotting the cumulative distributions of the minimum velocity location in each zone (Fig. 3.11B). We observe that the distributions for attractive droplets are shifted by 7 μm and 4 μm in zones 1 and 2 respectively (measured shift at 50%), indicating that rearrangements are indeed delayed in the channel compared to the low depletion case.

Furthermore, we analyzed the average number of neighbors per droplet along the constriction (Fig. 3.11C). Droplets in lines 1 and 4 enter the constriction with 4 neighbors in a hexagonal lattice, and exit with 2 neighbors like all droplets in the smaller channel. We measured the positions along the channel where droplets transition on average from 4 to 3 and from 3 to 2 neighbors respectively.

We find that, for the more attractive emulsions, the transitions from 4 to 3 and from 3 to 2 neighbors are delayed by 11 μm and 8.5 μm respectively.

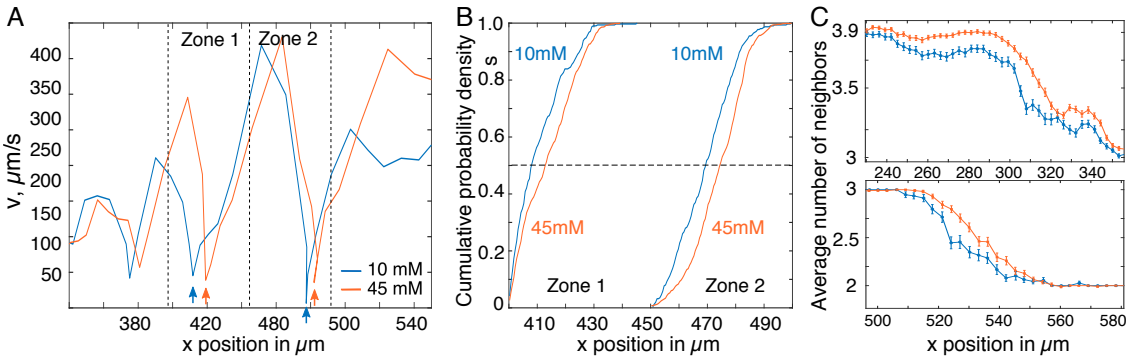

Figure 3.11 | **Analysis of droplet velocity and number of neighbors** (A) Typical velocity curves of individual droplets in lines 1 and 4 along the channel axis for 10 mM (blue) and 45 mM SDS (orange) emulsions. The velocity drops to a minimum value (indicated by an arrow) in zones 1 and 2 each time the droplets slows down before a rearrangement. For each droplet trajectory we find the location of this minimal velocity to build the cumulative probability density of panel (B). (B) Cumulative distributions of the minimum velocity location for lines 1 and 4. The 45 mM SDS droplets slow down farther into the constriction, as evidenced by the shift in distributions at 50% probability, by about 7 μm in zone 1 and 4 μm in zone 2. (C) Average number of neighbors per droplet along the channel for lines 1 and 4. For more attractive emulsions, the number of neighbors drops from 4 to 3 and then from 3 to 2 respectively 11 μm and 8.5 μm later in the constriction.

Our findings suggest that depletion attraction forces between droplets affect the topology of rearrangements by causing delays of T1 events.

3.1.6 The effect of the flow rate

Finally, we checked if the flow rate had an effect on droplet deformation. Indeed, as we use a pressure pump to flow the emulsions, we do not have a precise control over the flow rate. For this, the droplets are individually tracked in the channel in order to extract their average velocities v, that spans from 120 to 360 $\mu m/s$ (the velocities are measured in the thin channel). For a given v, we measured the average deformation of all considered droplets (Fig. 3.12A). We found that the deformation does not depend on the instantaneous droplet velocity within the investigated range for both SDS concentrations.

We also studied the effect of the flow speed on the location of the velocity minima in the specific areas in the constriction (zone 1 and zone 2). We compared the cumulative distributions of these locations for all the experiments and for the experiments with the same flow speed (80μm/s) for 10 mM and 45 mM SDS emulsions respectively (Fig. 3.12B). One can see a slight shift between the two velocity conditions, but the difference between the curves for low and high attraction is preserved. Therefore, we can conclude that the flow rate does not affect significantly the locations of the velocity minima.

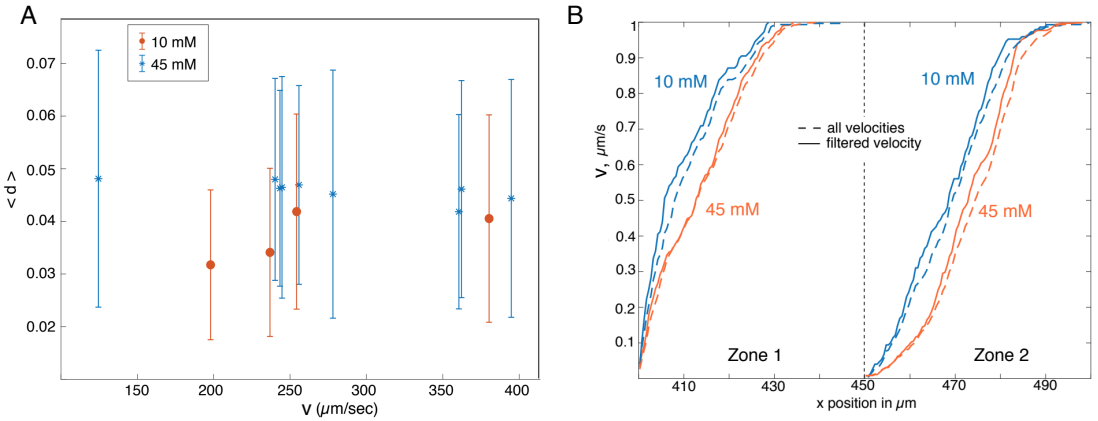

Figure 3.12 | **The effect of the flow rate on droplet deformation and rearrangements.** (A) Average deformation $\langle d \rangle$ as a function of instantaneous droplet velocity v in the small channel. (B) Cumulative distributions of the minimum velocity location as a function of flow speed in the wide channel. The minima are found for the droplets in lines 1 and 4 for 10 mM (blue) and 45 mM (orange) SDS, in zones 1 and 2. Dashed lines are obtained for all velocities (average velocity of 76 ± 10 μm/s for 10 mM SDS and 97 ± 13 μm/s for 45 mM SDS), solid lines are obtained for data that is filtered as a function of droplet velocity, in particular we only keep droplets displaying a similar average velocity of 71 ± 3 μm/s.

3.1.7 Conclusion

In this part of our work, we probed the effect of adhesion on the structural and rheological properties of emulsions by introducing non-specific attractive interactions induced by depletion between the oil droplets. We first evidenced that such attraction forces are too low to induce any measurable effect in 2D static packings of droplets. Indeed, for both attraction forces, we recovered the scaling laws predicted by [18] for purely repulsive packings, with a critical packing fraction $\phi_j \approx 0.842$. However, using ordered monodisperse emulsions, we uncovered distinct changes in their elasto-plastic response, when the droplets were flowed through a 2D physical constriction. The first manifestation of the attraction force was an increase of the average deformation of the droplets in the constriction. The second one was a delay of the topological rearrangements inside the constriction as attraction forces are increased.

It is quite remarkable that such low attraction forces are enough to modulate the elasto-plastic response of emulsions in our system. However, the effect of depletion attraction is very subtle, and it is unsure if it would have been clearly evidenced with disordered polydisperse emulsions.

After demonstrating the effect of weak non-specific attraction, we are now going to make the next step towards mimicking biological tissues by introducing specific binders on droplet surfaces. These binders will establish specific interdroplet adhesion, mimicking intercellular cadherin adhesion. In addition, this specific adhesion has a higher adhesive energy, and thus one can anticipate that it will affect in a stronger way the elasto-plastic response of emulsions compared to the depletion attraction.

3.2 Biotin-streptavidin-biotin bonds to mimic intercellular specific adhesion

For our second set of experiments, we considered a specific adhesion between the droplets using biotin-streptavidin-biotin bonds. The adhesive energy of those bonds is much higher ($\sim 10kT$ per bond) than that of the non-specific depletion attraction we have studied in the previous section, and is comparable to the one of cadherin homophilic interactions in tissues. Moreover, the fluidity of the droplets surface allows the binders to diffuse along the oil/water interface and to aggregate into adhesion patches at each droplet-droplet contact. For these experiments, we used polydisperse emulsions to prevent long range crystalization effects and to better mimic the natural size distribution of cells [129].

As it was done in the previous section, we have studied the response of this system under mechanical stress by pushing the droplets through a 2D microfluidic constriction. In order to study a bigger number of droplets, we modified the dimensions of the channel to make the constriction region larger (*see* Fig. 2.4). Now, the width of the large channel is about 30 droplet diameters, and it progressively reduces to one droplet in the thin channel (*see* Chapter 2). This geometry forces more rearrangements in the emulsions and allows us to study their elasto-plastic response away from the channel border eliminating possible boundary effect. In addition, such geometry aims to mimic the convergent extension of epithelial tissues that is essential during embryogenesis. In the mean time, pressure-driven flows mimic the forces that are imposed on tissues during morphogenesis, where they arise from the growth of neighboring tissue leading to a slow pressure buildup. Again, here, we experimentally study and compare the response of both non-adhesive and adhesive emulsions.

3.2.1 Mimicking the cellular membrane and adhesion

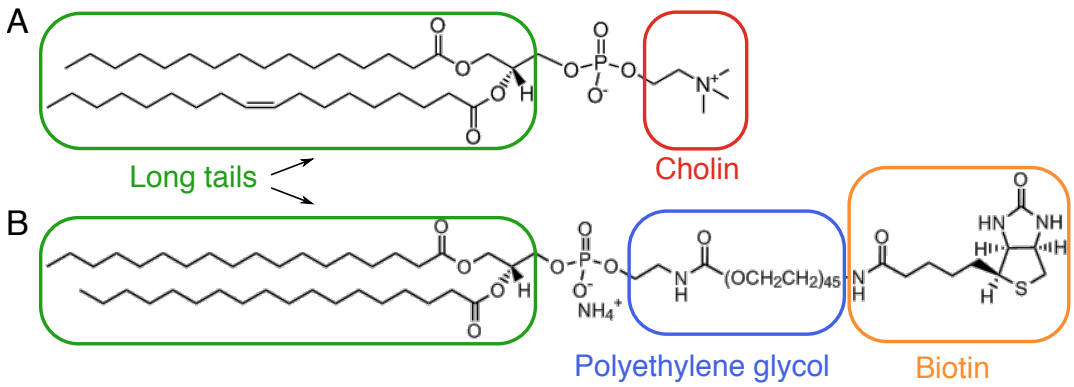

Figure 3.13 | **Structural formula of lipids that were used for droplet stabilization.** (A) Egg PC. (B) DSPE-PEG-biotin. Adapted from Avanti Polar Lipids.

Polydisperse emulsions were stabilized with a mixture of two lipids (Fig. 3.13), EPC and DSPE-PEG-biotin (mass ratio 9:1). Such a choice of lipids is dictated by the lipid membrane composition of a living cell. Indeed, while the exact lipid composition of cell membranes is different for each

cell type, cells share similar features in their lipid distribution between the external and cytosolic (internal) leaflets. In particular, the external leaflet consists mainly of phosphatidylcholine (PC) and sphingomyelin (SM). Both of these lipids have a hydrophobic tail composed of either two fatty acyl chains in the case of PC, or of a long hydrocarbon and a fatty acid chain in the case of SM. In addition, both of them have choline polar heads. Such long tails have a high tendency to aggregate, and, in combination with the large heads, they form the external leaflet of the cell membrane which is less fluid compared to the internal one.

Therefore, EPC, which belongs to the family of PC (*see* Fig. 3.13A), is our choice for droplet stabilization as a main interfacial component (90% of the membrane lipid mass). DSPE-PEG-biotin also contains a long tail, similar to that of EPC (*see* Fig. 3.13B). In addition, its hydrophylic head is grafted with a long polyethylene glycol chain, which acts as a polymer brush to induce steric repulsion between the droplets. Moreover, this PEG chain is biotinylated, which provides the ligands the ability to bind with streptavidin to mimic adhesion. One strepdavidin molecule can bind to four biotin molecules through strong non-covalent bonds. Our droplets thus adhere through biotin-streptavidin-biotin complexes between contacting surfaces.

3.2.2 Adhesive patches formation

To create and observe adhesive bonds between the droplets, we have functionalized the biotinylated lipids on the droplet surface with fluorescent streptavidin (*see* Chapter 2). When the functionalized droplets are in a tube, the equilibrium separation between the droplet surfaces exceeds the distance over which the binding proteins can interact and the fluorescence on the droplet surface remains homogeneous. However, Pontani *et al.* [141] demonstrated that compression forces make droplet surfaces come closer together thus enabling streptavidin-biotin interaction. Moreover, the presence of salt (*see* Chapter 2) in the continuous phase dampens electrostatic repulsion between the droplets, thus facilitating their mutual adhesion. With time, these bonds aggregate into adhesion patches at each droplet-droplet contact. The progressive formation of the patches is shown in Fig. 3.14.

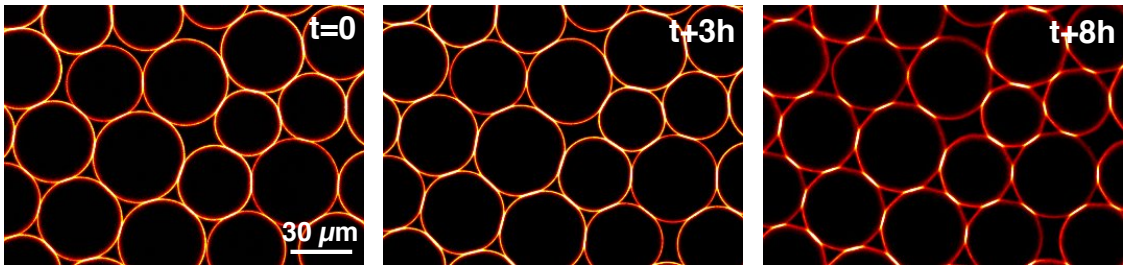

Figure 3.14 | **Progressive formation of adhesive patches over time.** At the beginning of the experiment, streptavidin fluorescence is more homogeneously distributed over the surface of the droplets (left image). Over time, biotin-streptavidin-biotin bonds form at the droplet-droplet contacts (middle image) until they enrich into clear adhesive patches with an increased fluorescence signal (right image). Note that the formation of the patches depletes the fluorescence level on the free edges of the droplets making it appear more red over time.

At the beginning of the incubation process, the streptavidin is homogeneously distributed over the whole surface of the droplets. However, over time, biotin-streptavidin-biotin bonds form at the droplet-droplet contacts leading finally to a redistribution of the streptavidin molecules into adhesive patches with an increased fluorescent signal. This effect is clearly evidenced in Fig. 3.14. With the color code used for this figure, an increasing intensity of the signal appears as a whitening of the colors, and the adhesive patches appear white. Simultaneously, the formation of the patches depletes the number of streptavidin molecules on the free edge of the droplets, making it less fluorescent and thus appearing more red over time. However, the remaining fluorescence of the free edge of the droplets indicates that unbound streptavidin molecules are still present. The reason for this is not clear. It could be due to an initial excess of streptavidin on the surface, or the system might just reached its equilibrium in streptavidin repartition with the maximum area density of streptavidin in the patch.

When droplets are adhesive, one expects their flow to be hindered, since droplets need to break their adhesive contacts in order to rearrange. Indeed, a higher pressure has to be applied for adhesive emulsions to flow in the constriction compared to non-adhesive ones. On average, in our experimental conditions, for repulsive droplets, one needs to apply about 15-20 mbar with the pressure controller, as opposed to 30-60 mbar for adhesive ones. At the macroscopic scale, these two systems therefore exhibit very distinct material properties. We show in the following sections the microscopic origin for this difference of behavior.

3.2.3 Effect of specific adhesion on the global rearrangements topology

As it was told above, highly packed emulsions behave as solids at small applied stresses, but at higher applied stresses they undergo plastic deformations and then flow. Such a behavior is also typical for various other systems, such as foams, granular materials, colloids and molecular glasses. The universal nature of such plasticity has been an important question during the last decades. While crystal plasticity is governed by the motion of dislocations (*i.e.* irregularities within a crystal structure) [123, 172], in amorphous solids, there is no order, and dislocations cannot be defined. Instead, the modern vision of plasticity in amorphous solids is based on the concept of localized plastic events in which a few particles rearrange. Such events were originally introduced by Argon [4] and have been observed to cause flow heterogeneities in many different studies. Le Bouil *et al.* [101] observed a nonhomogeneous strain that appeared as transient bands of mesoscopic size (dozens of grains) and a well-defined orientation under a homogeneous stress applied on a granular material. They associated the presence and the orientation of those bands with localized plastic reorganizations that redistribute stresses in a surrounding continuous elastic medium. Similar results were obtained by Amon *et al.* [2]. These authors studied a granular packing under shear as a model amorphous system, and observed the deformation field at the free surface of the packing. They found that during a stress drop (Fig. 3.15A), localized spots of increased plastic deformation (*i.e.* grain rearrangement) occurred progressively until the emergence of ruptures into the material (*see* Fig. 3.15B). The rate of occurrence of these localized events is linked directly to the plasticity of the system (Fig. 3.15C). Indeed, each local rearrangement of

grains modifies locally the mechanical equilibrium, causing the surrounding material to deform, and creating internal stresses. These stresses may then trigger other rearrangements, leading to a succession or avalanche of rearrangements [108, 47, 8].

In our experiment, we have access to the whole dynamics during the emulsion flow, and we thus examine the statistics of the avalanche sizes through a measure of the local plastic rearrangements, namely T1 events, and compare both adhesive and non-adhesive emulsions.

Intuitively, one could expect adhesion to give rise to long range effects leading to bigger avalanches. To check this hypothesis, we have thus measured the size of the avalanches for adhesive and repulsive emulsions. The avalanche size is defined as the number of droplets participating in spatially and temporally connected rearrangements during a given time window. Droplets are considered to be connected if their Voronoi cells share a common edge (*see* Chapter 2). In this way, T1 events whose cells are neighbors at any point within the time window are grouped in the same avalanche. We studied the avalanche size distributions and found that surprisingly for both repulsive and adhesive emulsions, the avalanches size distribution follows a power law of exponent ~ -2 (Fig. 3.16B). The value of this exponent is in agreement with those obtained by Bares *et al.* [8] for 2D sheared granular packings in numeric simulations and experiments (Fig. 3.16A).

To confirm this observation and to explore a wider range of parameters, numerical simulations were performed in collaboration with Thibault Bertrand and Franck Pan (Department of Mathematics, Imperial College, London). For this purpose, a computational toy model for adhesive emulsions has been developed based on the deformable particle model (DPM) recently introduced

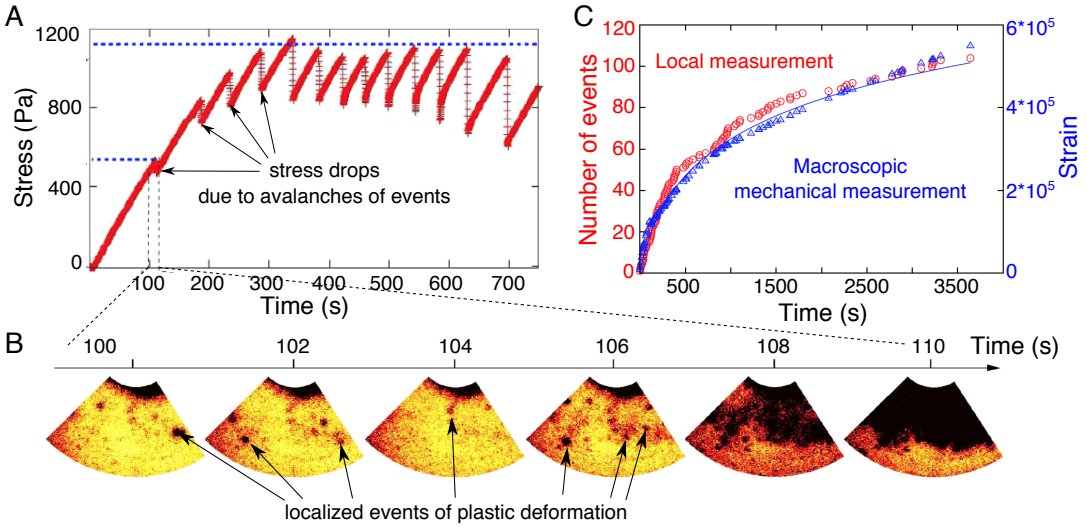

Figure 3.15 | **Local plastic deformation underlies global plasticity.** (A) Stress response for an imposed shear increases linearly with time at small times, as expected for an elastic material. Small stress drops (indicated with arrows) are observed as a consequence of the avalanches of localized events of plastic deformation. (B) Localized events of plastic deformation can be observed on correlation maps between successive images of the free packing surface during the first stress drop. (C) The temporal evolutions of the strain in a creep experiment (blue triangles) and cumulated number of local plastic deformation events (red circles) are very similar. Adapted from [2].

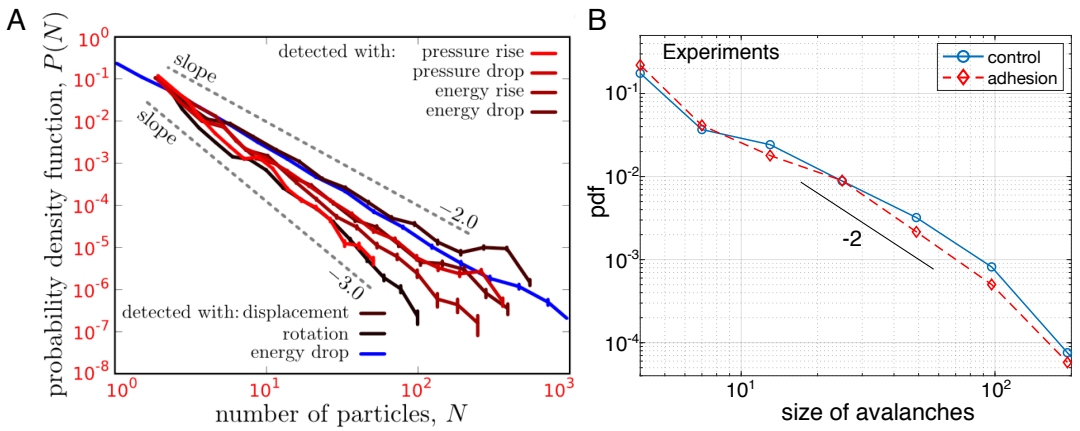

Figure 3.16 | **Avalanche statistics.** (A) Experimental data of Bares *et al.* [8]. Probability density functions $P(N)$ of the avalanche sizes measured in terms of number of particles involved in each avalanche. Adapted from [8]. (B) Experimental data from our experiments. Distributions of avalanche size for adhesive (red dashed line) and non-adhesive (blue solid line) emulsions cannot be distinguished. A line corresponding to a power law with exponent -2 was drawn as a guide to the eye.

by Boromand *et al.* [19, 18]. The principle of the model is the following.

Each of the N emulsion droplets is modeled as a deformable polygon with N_v circulo-line edges of width δ. The model relies on the minimization of the following potential energy

$$U_{DP} = \gamma \sum_{m=1}^{N} \sum_{i=1}^{N_v} l_{m,i} + \frac{k}{2} \sum_{m=1}^{N} (a_m - a_{m0})^2 + U_{int} \tag{3.7}$$

where $l_{m,i}$ is the length of the circulo-line between vertices i and $i+1$ and a_m is the area of particle m. The first term of U_{DP} is proportional to the perimeter of the droplet with a proportionality constant γ corresponding to a line tension. The second term in this potential energy is a penalization term quadratic in the distance between the area of the droplet and a target area a_{m0}, with a compressibility coefficient k. Finally, U_{int} represents the potential energy of interaction between two droplets, which is composed of the sum of a repulsive term and an attractive term (Fig. 3.17). The repulsive term prevents overlapping between interacting droplets and depends on the minimal distance $d^{\min}_{mn,ij}$ between the circulo-lines i and j respectively on droplets m and n. The adhesive term represents an attractive force between the droplets; it is proportional to a coefficient k_a and is applied only after two droplets initiate a contact.

Finally, the simulations were performed using the same constriction angle as in the experiments ($\alpha = 20°$). The emulsion is flowed through the constriction by subjecting each vertex composing the droplets to a constant force $F_g = 0.002$ in the direction of the channel. More details about the model can be found in [63].

This model has allowed us to systematically vary the adhesion energy (by changing the coefficient $k_a \in \{0, 0.01, 0.1\}$), droplet deformability (by changing the line tension $\gamma \in \{0.1, 0.25\}$) and polydispersity. Varying these parameters in the experiments would be difficult as the parameters

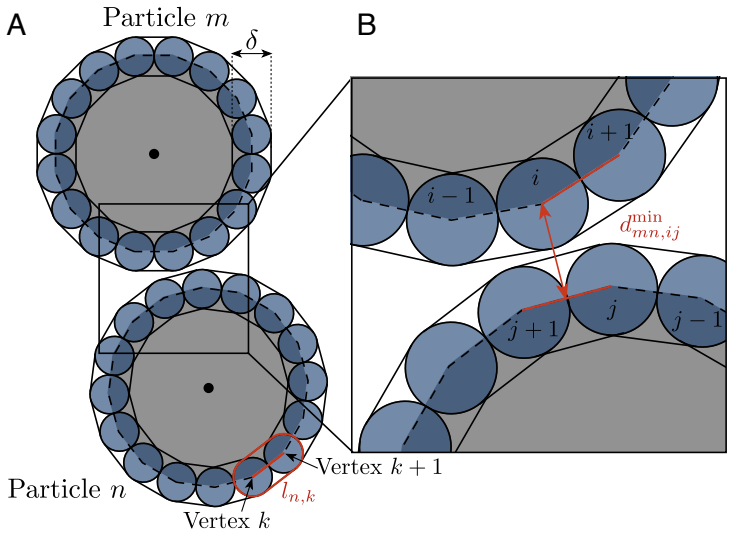

Figure 3.17 | **Schematic of the simulation model.** (A) Deformable particles m and n composed of $N_v = 16$ vertices with δ, the length of the circulo-line between vertices k and $k+1$ of particle n is denoted $l_{n,k}$. (B) Close-up on the region of interaction between the two deformable particles. The minimal distance between the circulo-line i on particle m and j on particle n is denoted $d^{\min}_{mn,ij}$.

are not independent from each other. In particular, the surface tension of the droplets (and thus their deformability) can be varied by using different lipid composition, or by adding other types of surfactants, but it would also affect the adhesion strength. And vice versa, in order to increase the adhesion in our system, one would need to increase the number of biotin-streptavidin-biotin bonds in the adhesive patch, which could be done by increasing the concentration of biotinilated lipids on the droplet surfaces. However, the addition of the extra lipids would change droplet deformability. Alternatively, we could change the system by introducing interdroplet adhesion through complementary DNA strands (*see* Chapter 1). In this case, adhesive energy can be changed by varying the length of the these strands [156]. Therefore, we chose numerical simulations to explore the effect of these parameters.

First, packings with the same polydispersity (20%) as in our biomimetic emulsions were examined. Similarly to our experimental findings, the presence of adhesion did not affect significantly the distribution of the avalanche sizes, which in both cases follows a power-law of exponent ~ -2 (Fig. 3.18A). Then, we checked the effect of adhesion on monodisperse packings. The obtained distributions also did not show any significant difference between adhesive and non-adhesive emulsions. However, our simulations revealed an effect of polydispersity on the size of avalanches. This effect can be observed for the droplets with the lowest deformability ($\gamma = 0.25$). As it is shown in Fig. 3.18B, monodisperse packings exhibit an excess of large avalanches for all adhesion energies compared to polydisperse packings. This observation is consistent with the idea that low deformability monodisperse particles, like grains, exhibit a higher crystalline order leading to large rearrangements taking place along disclination planes (planes with broken crystalline order) [172, 58].

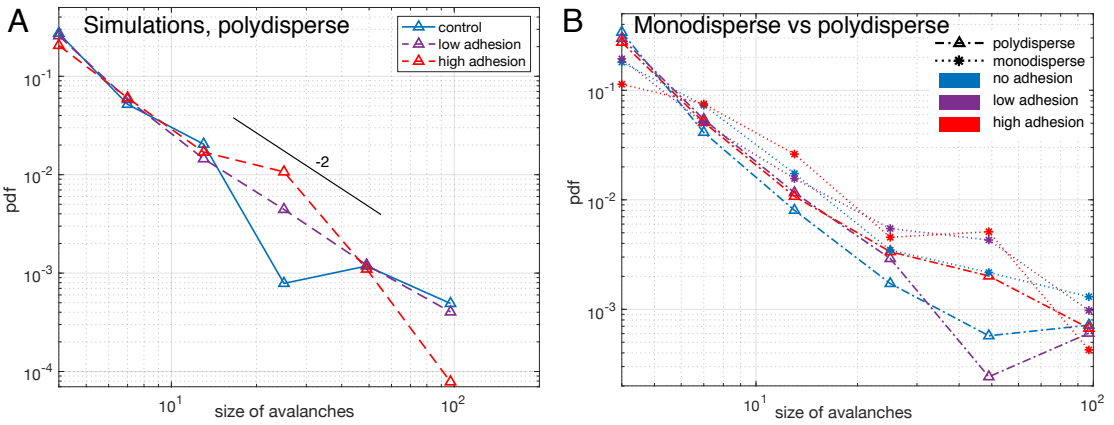

Figure 3.18 | **Avalanche statistics for simulation data** -(A) Distributions of avalanche size for polydisperse packings of highly deformable droplets (lowest γ) without adhesion (blue solid line), with low adhesion (purple dashed line) and high adhesion (red dashed line). A line corresponding to a power law with exponent -2 was drawn as a guide to the eye. (B) Probability density function (pdf) of the avalanche sizes for simulated packings of polydisperse (dash-dotted lines with triangles) and monodisperse (dotted lines with stars) droplets for three different levels of adhesion. For polydisperse droplets, the distributions of repulsive and attractive emulsions are not significantly different between each other for both experiments and simulations. In simulations, the monodisperse packings exhibit higher avalanche sizes compared to polydisperse packings for every adhesion level. All simulation curves are averaged over 5 repeats of simulations performed with the same parameters. The logarithmic binning as powers of two is used for the x-axis for all panels.

3.2.4 Local dynamics of rearrangements in the presence of adhesion

While we could not find evidence of the effect of adhesion on the statistics of the avalanche sizes, consequences of adhesion could be evidenced locally by examining the dynamics of individual rearrangements. During a T1 event, the contact edge between neigboring droplets shrinks progressively until it disappears completely, and the droplets rearrange (Fig. 3.19A). Therefore, the duration time of T1 events depends on the rate with which the contact edge shrinks. Adhesion between the droplets resists the breaking of this edge and can thus affect its rate of shrinking.

In order to study the role of adhesion on the duration of T1 events, we have first measured the speed at which contact edges between Voronoi cells were shrinking before the actual neighbor exchange (*see* Fig. 3.19A). To do so, we measured $\frac{\Delta l_e}{\Delta t}/\langle V \rangle$, where l_e is the contact length between neighboring Voronoi cells, $\Delta l_e = l_e(\text{frame } n) - l_e(\text{frame } n+1)$ and Δt the time between two consecutive frames. We measured it for all the droplets involved in a T1 event during the adimensional time window $[t_0 - 10, t_0]$, t_0 being the exact moment of neighbor exchange.

We found that the edge length shrinks more slowly for adhesive droplets for all edge lengths, as shown in Fig. 3.19B. We explain it by the fact that the presence of adhesion helps to stabilize short edges and slows down the dislocation process by adding a strong energetic barrier. Such a slowing down may lead to delays of T1 events, which were shown to strongly affect the rheological properties of tissues. Using numerical simulations, Erdemci-Tandogan *et al.* [46] demonstrated

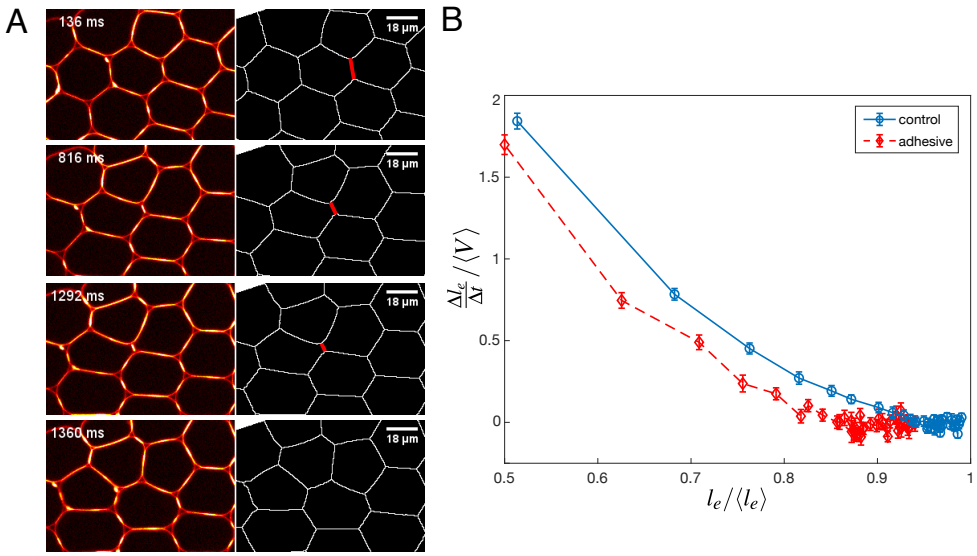

Figure 3.19 | **Local dynamics of rearrangements** (A) Shrinking contact edge between Voronoi cells during a T1 event. Confocal snapshots of adhesive droplets undergoing a T1 rearrangement (left) and their corresponding Voronoi cells (right). The shrinking contact edge between Voronoi cells is shown in red. (B) Rate of shrinking for dislocating edges of length l_e normalized by the average velocity of the flow $\langle V \rangle$ plotted as a function of l_e normalized by the global average edges length $\langle l_e \rangle$. For a given l_e, a dislocating edge length is always disappearing more slowly for adhesive emulsions.

that an increase of the duration of T1 events by 10% solidifies the tissue by increasing the tissue relaxation time.

In conclusion, avalanche size statistics in flowing emulsions are not affected by adhesion. In fact, the signature of adhesion only lies in the local dynamics of T1 events rather than in long range collective effects. However, this local dynamics of T1 events can have a strong impact on the elastic properties of the emulsions. In the next section, we study the impact of these local dynamics on droplet deformations.

3.2.5 Adhesion as a trigger of droplet deformation and alignment

As it was shown in Section 3.1, T1 rearrangements lead to the relaxation of deformations in the system [31]. Therefore, the impairment of T1 events due to adhesion, which was described above, should result in the accumulation of the droplet deformation in adhesive emulsions. Moreover, during elongation, the adhesion patches induce pulling forces on the droplets in addition to the compressive forces induced by the constriction geometry. To relate the locally slowed down rearrangements to increased deformations, we have examined the deformation of droplets involved in T1 events by measuring their shape parameter $\mathcal{A} = p^2/4\pi a$ over the course of the rearrangement. An example of such measurement is shown in Fig. 3.20: initially low, droplet deformation progressively increases reaching its maximum right before the rearrangement, and finally drops down after the T1.

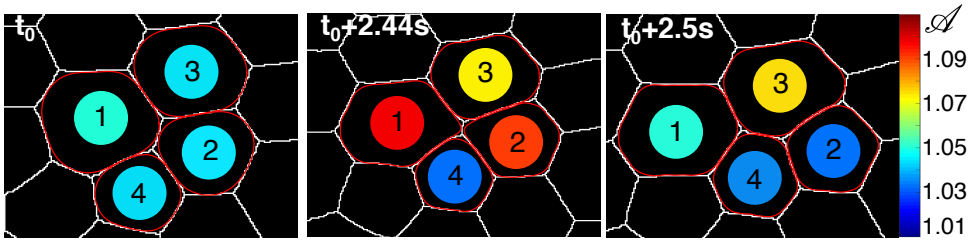

Figure 3.20 | **Droplet deformation during a T1 event.**

In order to quantify the observed "relaxation" of the deformation, we compared the deformation of contacting droplets before and after the rearrangement. For this, we calculated $\Delta\mathcal{A} = \frac{\mathcal{A}_1^{t^-}+\mathcal{A}_2^{t^-}}{2} - \frac{\mathcal{A}_3^{t^+}+\mathcal{A}_4^{t^+}}{2}$, where $\mathcal{A}_1, \mathcal{A}_2$ are droplets that were in contact before a T1 event, and $\mathcal{A}_3, \mathcal{A}_4$ are droplets that became in contact after the T1 event, and t^- and t^+ are the frames just before and after the rearrangement, respectively (Fig. 3.20). For non-adhesive emulsions, we find that the distribution of $\Delta\mathcal{A}$ is symmetric around zero, indicating that droplet deformations are identical before and after the rearrangements (*see* Fig. 3.21). In contrast, for adhesive emulsions, this distribution becomes asymmetric with a "shoulder" corresponding to positive values of $\Delta\mathcal{A}$. Such distributions demonstrate that adhesive droplets accumulate excessive deformation prior to rearrangements. However, after detachment, the droplets do not exhibit any excess in deformation and thus behave like repulsive droplets. Such behaviour of the adhesive droplets makes sense, because in our system adhesion is short range and dense adhesive patches form on the timescale of hours.

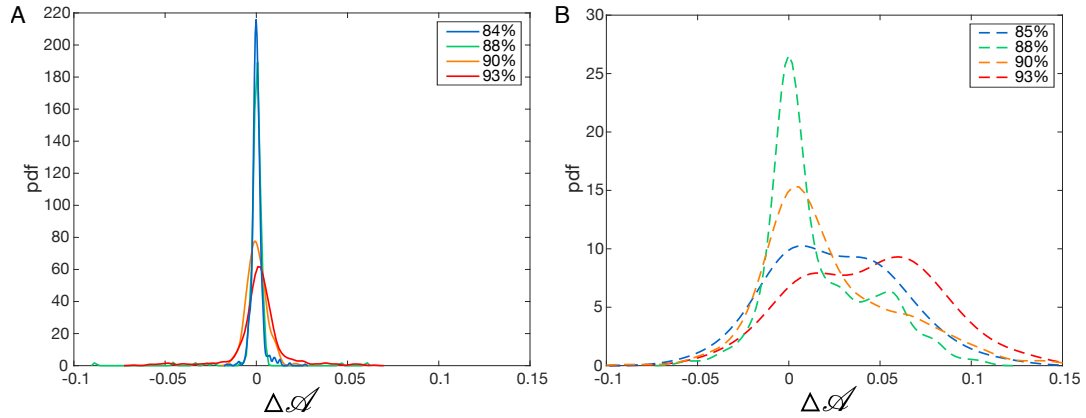

Figure 3.21 | **Relaxation of droplet deformation during T1 events.** Probability density function (pdf) of the deformation $\Delta\mathcal{A}$ calculated in the constriction for different packing fractions in the case of (A) non-adhesive and (B) adhesive emulsions. While the distributions for non-adhesive emulsions are symmetrical and centred around zero, the distributions for adhesive emulsions become asymmetrical with a shoulder corresponding to positive values of $\Delta\mathcal{A}$. This shows the accumulation of excessive deformation of adhesive droplets before T1 events, prior to a subsequent relaxation of the deformation after the T1 event.

To further investigate the role of adhesion in the accumulation of droplet deformation, we related the amount of excess deformation $\Delta\mathcal{A}$ during rearrangements to the binding energy between droplets. We can qualitatively estimate the binding energy by looking at the intensity of fluorescence of the droplet contact area. Indeed, as fluorescence of our droplets is due to strep-

tavidin molecules, and adhesion between the droplets arises from biotin-streptavidin interactions, the strength of adhesion is proportional to the level of patch fluorescence. We thus plotted $\Delta\mathcal{A}$ as a function of the streptavidin fluorescence intensity at the dislocating contact area of the droplets (Fig. 3.22). We find that a higher intensity, meaning a higher binding energy, directly correlates with the higher values of $\Delta\mathcal{A}$. These results confirm the hypothesis, that adhesion between the droplets leads to the accumulation of deformation by delaying droplet rearrangements.

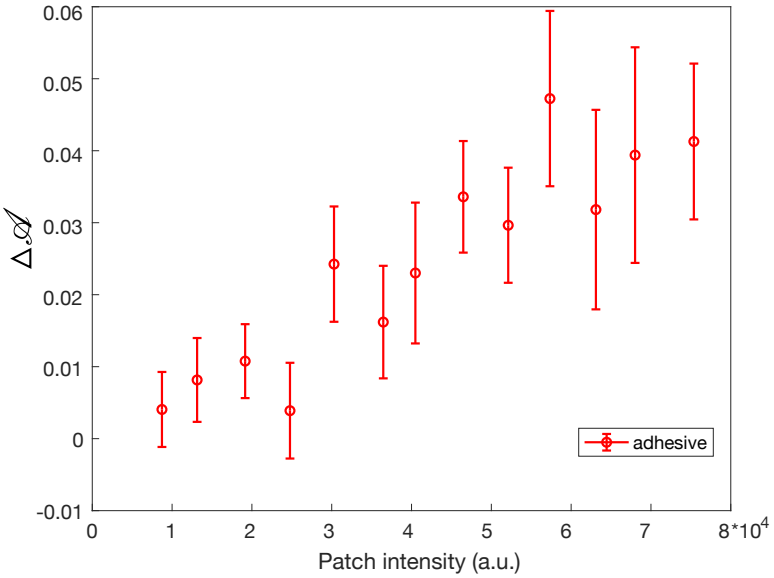

Figure 3.22 | Difference in droplet deformation $\Delta\mathcal{A}$ before and after they undergo a T1 event as a function of adhesive patch intensity. An increase of patch intensity, *i.e.* an increase in binding energy, corresponds to higher values of droplet deformation accumulated before a T1 event.

In order to check the effect of adhesion on the global level of droplet deformation in the system, we measured the shape parameter $\mathcal{A}$ for all droplets in all experiments. We then plotted the average values of $\mathcal{A}$ along the x axis of the constriction. We observe that the shape parameter of adhesive droplets is much higher compared to repulsive emulsions for all considered packing fractions (Fig. 3.23A). In addition, this high deformation does not relax back to the values measured for non adhesive emulsions even far from the outlet (*i.e.* $\approx$ 10 droplet diameters away from the entry of the small channel). This indicates that the effects of adhesion on droplet deformations are long-ranged, which suggests that forces are transmitted more efficiently through the emulsion in the presence of adhesive patches.

Finally, we checked whether adhesion affected the alignment of the droplets in the constriction. Indeed, recent works demonstrated that cell alignment plays a crucial role in defining the mechanical properties of tissues during morphogenesis [127, 166]. In order to study the alignment of droplets in our experiments, we fitted all droplets in the field of view with ellipses, as it was done in [127], and measured their aspect ratio and orientation of their major axis with respect to the horizontal x axis defined in Fig. 2.4B. As shown in the polar plot in Fig.3.23A, the aspect ratio of the droplets is significantly higher for adhesive emulsions for the whole range of orientations. Moreover, even though orientation of both adhesive and repulsive droplets is influenced by the

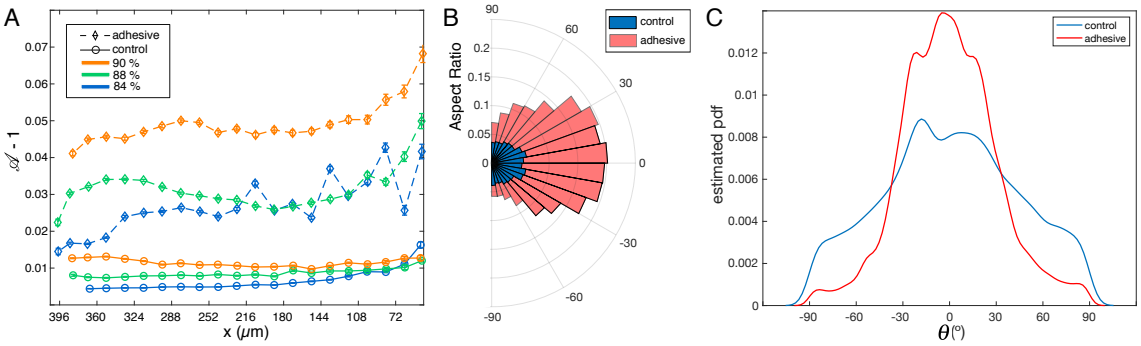

Figure 3.23 | **Analysis of droplet deformation** (A) Average deformation $\mathcal{A}$-1 of the droplets along the x axis of the channel for the adhesive (diamonds) and control (circles) emulsions at various packing fractions. The deformation is averaged in 35 μm bins along the x axis, x=0 corresponding to the entry of the thin channel. The error bars correspond to the standard error of mean for the distribution of $\mathcal{A}$ obtained in each bin. (B) and (C) Analysis of the ellipses fitted to control (blue) and adhesive (pink) droplets in packings with average $\phi_l = 88\%$. (B) Aspect ratios as a function of ellipse orientation. The aspect ratios for adhesive droplets are significantly larger for all considered angles. (C) Distributions of ellipse orientations θ with respect to the x axis in the constriction. Adhesive emulsions yield a narrower distribution than control ones.

constriction geometry and flow, the distribution of ellipse orientations is more peaked in the case of adhesive emulsions (Fig. 3.23C). These results suggest that specific adhesion between the droplets not only lead to higher droplet deformation, but also results in droplet elongation and alignment.

3.2.6 Conclusion

We developed a biomimetic system which should help us to study the role of cellular adhesion during morphogenesis in biological tissues. Our system consists of oil in water emulsions, where the adhesion between the droplets was first introduced as non-specific depletion attraction, and then as specific adhesion through biotin-streptavidin-biotin bonds, which mimics cadherin cell-cell adhesion in biological tissues. Using this system, we studied the effect of adhesion on the elasto-plastic response of emulsions to mechanical perturbations. We observed that both non-specific and specific adhesion modified the emulsion flow by favoring the elastic component of the response (*i.e.* reversible deformation of the droplets) and impairing the plastic component (irreversible droplet rearrangements). Indeed, in both cases, adhesion caused delays of T1 events, which led to the increase of droplet deformation. However, the effect of non-specific attraction was weaker compared to those of specific adhesion. In particular, depletion attraction did not affect 2D static packings of the emulsions. While we have not finished the study of the effect of specific adhesion on static packings (this will be discussed in Chapter 5), we evidenced its effect in the context of dynamic flow. The first manifestation of specific adhesion could be observed on macroscopic scales in a form of the emulsion rigidification: a higher pressure was needed to induce the flow after the formation of adhesive patches between the droplets. However, passed that threshold force, both repulsive and adhesive emulsions could flow and go through a constriction. On the microscopic level, the flow of the emulsions occurred through a cascade of local rearrangements

called avalanches. Our experiments and simulations both showed that adhesion did not affect the formation of the avalanches, and the size distributions of these avalanches were similar for both repulsive and adhesive emulsions. Meanwhile, the simulations evidenced a weak effect of the presence of a crystalline order in the spatial structure of the emulsions.

Nevertheless, specific adhesion between the droplets changed the local dynamic of those rearrangements. The presence of adhesion prevented the detachment of bound droplets, leading to the delays of T1 events. As a consequence, we observed an accumulation of excessive deformation of the droplets in the constriction region. In addition, specific adhesion triggered droplet elongation and alignment in the direction of the flow. Such droplet polarisation propagated dozen of droplets upstream from the outlet of the constriction.

Applying the obtained results in the context of biological tissues, we suggest that intercellular adhesion in combination with external compression is sufficient to cause the planar polarisation of cells. This, in turn, may trigger remodelling of the cellular cytoskeleton and an increase of actomyosin contractility at cell-cell junctions that are perpendicular to the extension axis [72, 112]. A positive feedback loop between external forces and the intracellular response could thus arise, activating the biochemical signalling inside the cells. Finally, the interplay between the biochemical and biomechanical signals would tune the progression of morphogenesis. Our hypothesis is supported by recent studies that also evidenced the importance of cell anisotropy to predict the fate of tissues and highlighted its impact for rapid morphogenetic movements such as the convergent extension of the drosophila germband [166].

Chapter 4

Mechanical forces in the olfactory placode shaping during the zebrafish morphogenesis

In this chapter, I am describing a complementary project I worked on during my PhD and that was done in collaboration with Marie Breau and her team (Developmental Biology Laboratory, Institute Biology Paris Seine). Together, we developed an approach to study *in vivo* the role of mechanical forces on the formation of the neural system in zebrafish. In particular, we studied the morphogenesis of the olfactory circuit in zebrafish embryos and one of its main component called the olfactory placode (OP).

As a matter of fact, extension of axons in the OP is only guided by extrinsic forces. In our project, we mapped out these forces using oil droplets injected into the area of interest in zebrafish embryos. These droplets serve as local force sensors without perturbing the development of the embryo. Allowing to study the mechanical properties of biological tissues *in vivo*, this project provides one more step towards the understanding of the role of biomechanical pathways during morphogenesis.

4.1 Neural circuits and their development

A neuron is the basic functional cell of the nervous system. Although neurons are different in their structure, a typical neuron consists of a cell-body (soma) and multiple protrusions, such as dendrites and axons (Fig. 4.1). Neurons communicate with each other *via* specialized contacts called synapses, where the axon terminal of one cell contacts another neuron's dendrite, soma or, less commonly, axon. A population of interconnected neurons that ensure the same function forms a neural circuit. Neural circuits are connected to one another to form large scale brain networks. For example, the human brain has some $8.6 * 10^{10}$ neurons [75], and each neuron has on average 7000 synaptic connections to other neurons. It has been estimated that the brain of a three-year-old child has about 10^{15} synapses.

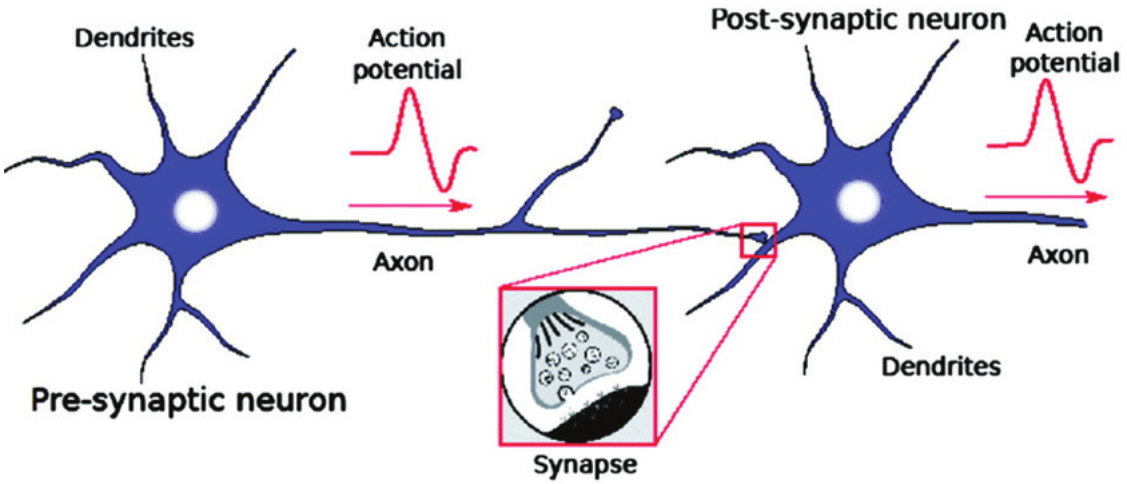

Figure 4.1 | **Schematic representation of neurons**. A typical neuron consists of a cell-body and protrusions called axon and dendrites. The axon of one neuron is connected to a dendrite of another neuron through a synapse, enabling the transmission of electrical signals (in the form of action potentials) and forming a complex neural circuit. Adapted from [77].

Each neural circuit maintains its own function and ensures the detection, transmission and processing of the information. Neural circuits are the basis of neural functions in health and disease, and the faulty assembly or disintegration of these circuits can result in disorders of the nervous system. Thus, the assembly of neural circuits, which happens through a series of developmental steps, requires a tight control and coordination [60]. First, the newborn neurons migrate to their final destination in order to correctly fit in the circuit. This is an active process which is ensured by the cytoskeleton activity of the neurons. When they have reached their destination, neurons emit multiple little protrusions through active cytoskeleton dynamics, one of which starts to grow and progressively differentiates into an axon. Once differentiated, axons elongate and navigate through pre-existing tissues to find their target cells. Simultaneously, they form additional lateral branches. Finally, only the branches that established functional synapses are selected, while the others are eliminated during the so-called pruning process. These developmental steps should occur in a well controlled and orchestrated manner in order to form the neural circuits at the right place and the

right time.

It is thought that the development of the nervous system is primarily guided by chemical cues from the surrounding tissues [154, 94]. Such guidance molecules form two classes: those that "attract" neurons, and those that "repel" them. In addition, the guidance molecules can act either on short, or over long distances. In the first case, the guidance occurs in a contact-dependent manner *via* adhesive molecules located on the surface of surrounding cells or on the ECM. In the second case, guiding molecules create chemical gradients that can be sensed by neurons *via* secreted diffusible molecules. Together, these attractive or repulsive molecules play the role of traffic signals that define the routes taken by migrating neurons and their growing projections. Simply said, guidance molecules create a "road map" for neurons that indicate the right and wrong directions (Fig. 4.2).

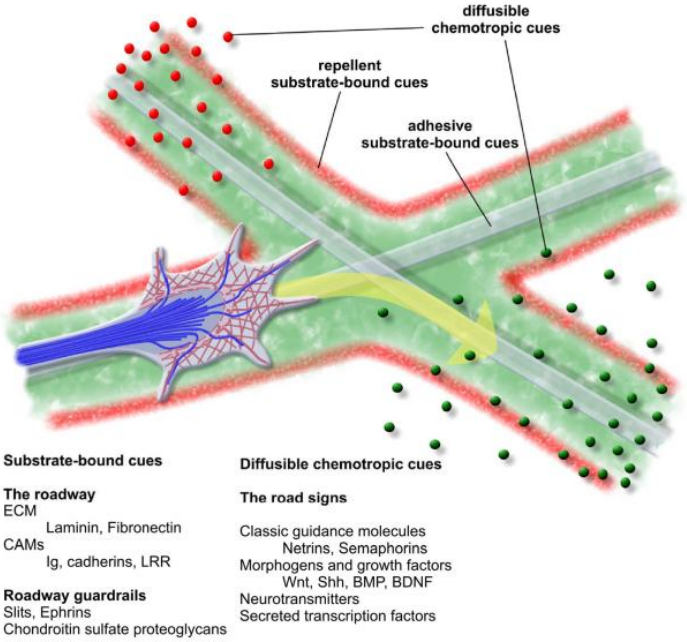

Figure 4.2 | **Chemical guidance of axon growth.** Axons travel upon a roadway, made up of adhesive molecules present on the surface of neighboring cells or in the ECM. Anti-adhesive surface-bound molecules provide the roadway 'guardrails' that determine roadway boundaries. Diffusive chemical cues additionally tune the growth of the axon over long distances. Adapted from [105].

However, in addition to well-studied chemical cues, *in vivo* neurons are also surrounded by a complex and dynamic environment exposing them to a variety of mechanical signals, including compression (pushing) or traction (pulling) forces exerted by neighboring cells or tissues. These mechanical signals are likely to influence the morphogenesis of neuronal circuits [60]. Numerous experiments *in vitro* actually showed the effect of such mechanical forces at each step of the development of neural circuits. For example, Lamoureux and colleagues showed [99] that applying an external mechanical tension stimulated the differentiation of minor extrusions into axons. The fact that axon growth can be stimulated by mechanical tension was first proved by Bray in 1984 [21], and later confirmed by numerous experiments [60]. Importantly, it was shown that mechanical

tension did not just stretch the axon, but triggered the addition of novel material on the tip and along the axon. Mechanical forces also likely participate in the pathfinding of growing axons, as shown in the recent work of Koser *et al.* [95], who studied neurons of the eye retina *in vitro* and *in vivo*. They found that the stiffness of the surrounding tissues determined the direction of axonal growth. The role of the mechanical forces was also shown to play an important role in the retraction of unfunctional lateral axon branches [3].

Despite evidences obtained from *in vitro* experiments, the role of the mechanical forces in neuronal development remains largely unexplored *in vivo* [60]. To address this question, Marie Breau and her team (Laboratory of Developmental Biology, IBPS) together with Léa-Laetitia Pontani developed an interdisciplinary project, that combines live imaging, physical approaches to measure and perturb forces *in vivo*, and molecular functional studies. In this project, they are focusing on the development of the zebrafish olfactory neural circuit.

4.2 Development of the zebrafish olfactory circuit

4.2.1 Zebrafish and its olfactory system

The zebrafish is a model animal that has been used in Neuroscience for a long time. It was first introduced into the laboratory by George Streisinger in the 1970s, and it rapidly grew as a model animal in developmental biology and genetics. Indeed, zebrafish has a rapid external development, a great genetic malleability and a high physiological and genetic homology to mammals. In addition, zebrafish is mostly transparent at the larva stage, which enables the use of optical methods such as high-speed and high-resolution microscopy, as well as new manipulative tools in the emerging field of optogenetics [150]. All these reasons make the zebrafish a unique vertebrate model organism to study neurogenesis, and, in particular, the formation of its olfactory circuit, whose superficial location makes it amenable to both live imaging and mechanical perturbation.

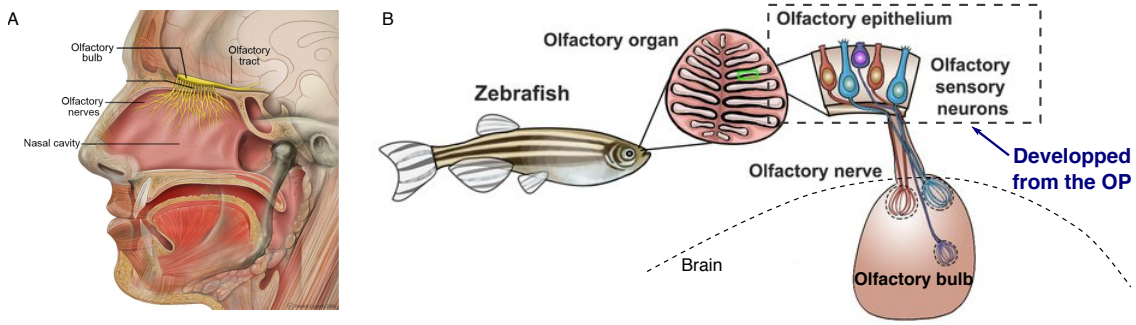

Figure 4.3 | **The olfactory circuit.** The anatomy of the olfactory circuit is similar between humans (A) and zebrafish (B). Olfactory sensory neurons from the olfactory organ (nose for humans) send their axons to the olfactory bulb which is located in the brain. Adapted from Patrick J. Lynch and [27].

The main function of the olfactory system is to sense smells. Odors are detected by olfactory sensory neurons (OSNs), which are part of the olfactory epithelium (OE) located in the nose (Fig. 4.3). Axons of the activated OSNs transmit electrical impulses to the first processing center in the brain called the olfactory bulb (OB). There, odor-evoked activity patterns are processed by a network of neurons and are eventually conveyed to higher brain areas [124]. Thus, establishing precise connections between the OE and the OB during the development is crucial for the olfactory system to function properly.

4.2.2 The role of extrinsic mechanical forces on axon extension

In zebrafish, the olfactory epithelium develops from the two cell regions near the brain, which are called the olfactory placode (OP) (Fig. 4.4A-B). Breau *et al.* [22] demonstrated that the formation of the OP occurs through a shrinking of the initial placodal field in the anteroposterior (AP) direction combined with an elongation in the mediolateral (ML) direction (Fig. 4.4B).

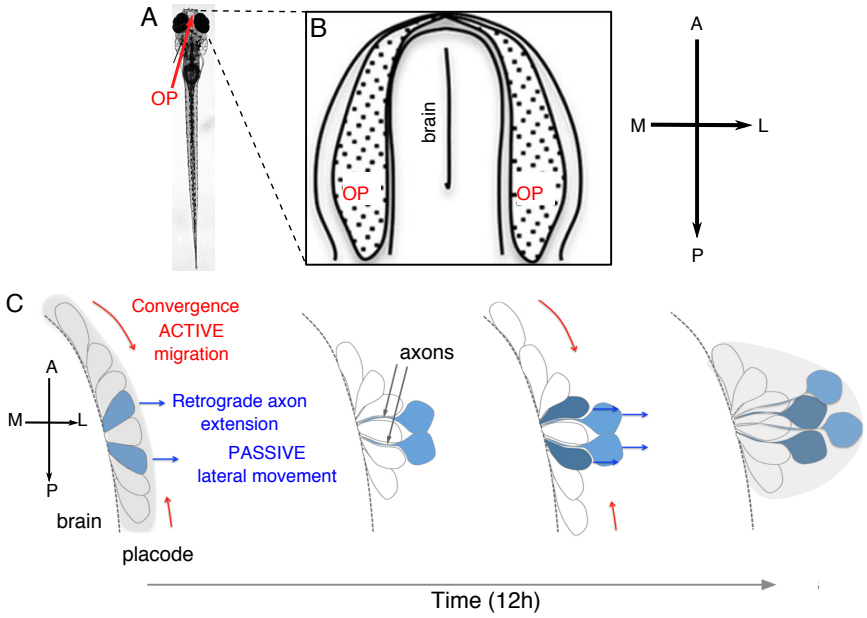

Figure 4.4 | **Formation of the olfactory circuit during the OP morphogenesis**. (A) Top view on zebrafish larva. (B) Zoomed region of the OP. (C) Proposed model for the circuit formation. Neurons from the OP extremities converge towards the center through active migration along the brain surface (red arrows), while cell bodies of central cells passively move away from the brain (blue arrows). As they move laterally, axon tips of the central neurons keep contact with the brain surface, which results in axon elongation (blue, retrograde axon extension). Adapted from [22].

Tracking of individual neuronal cells showed that two types of cell movement underlay the formation of the OP. The cells from the anterior and posterior regions of the initial placodal field first migrate along the AP axis to converge towards the central region of the placode (convergent movement), and then they move laterally, away from the brain surface (lateral movement), extending their neurons. Central cells undergo only lateral movements, without drastic displacement along the AP axis (Fig. 4.4C). This suggests that the OP morphogenesis can be driven by a com-

bination of convergence and lateral cell movements (Fig. 4.4B). Most importantly, Breau *et al.* demonstrated that the axon elongation occurred in an unusual way: the cell bodies were moving laterally while axon tips remained anchored to the brain surface. Such a retrograde extension of the axons contrasts with a canonical mechanism, where axons outgrow from the cell bodies and navigate towards their target [60, 22].

Combining live imaging and drug suppression of different key cytoskeletal components that are usually involved in cell movements, Breau *et al.* showed that while convergent movements were representative of an active cell migration process, lateral movements that provoked retrograde axon extension were passive, non-autonomous processes. The passive nature of these lateral movements suggests that axon extension is driven by extrinsic forces exerted on the central OP cell bodies, pushing or pulling them away from their anchored axon tips. In agreement with this suggestion, tension maps obtained with laser ablation of cell/cell contacts in the developing OP showed that the highest tension was located at the center of the OP, along the mediolateral (ML) axis (Fig. 4.5).

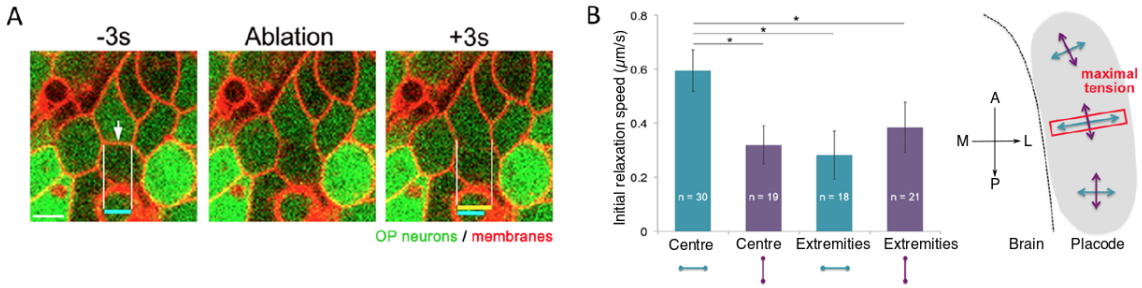

Figure 4.5 | **Tension maps in the OP.** (A) Laser ablation of cell/cell contacts was performed to map tension in the OP. The initial relaxation speed of vertices was used as a proxy for tension. Yellow and blue bars show the vertex/vertex distance before and after ablation. (B) Laser ablation was performed at an intermediate stage (16-18s), in the OP centre and extremities, on cell/cell contacts oriented parallel (purple) or perpendicular (green) to the brain surface. The highest tension was measured in the OP centre, perpendicular to the brain surface. Scale bar: 10 μm. Adapted from [22]

These results are compatible with two non-exclusive possible sources of extrinsic forces generating tension anisotropy and driving axon extension (Fig. 4.6): either an anteroposterior (AP) compression from actively converging OP cells squeezes central cell bodies away from their axon tip (compression hypothesis, Fig. 4.6A,C) - inducing passive stretching of the cell/cell contacts and thus high ML tension in the OP center - or ML traction exerted by the morphogenetic cell movements in the underlying eye tissue pulls cell bodies away from the brain (traction hypothesis, Fig. 4.6B,C).

To confirm these hypothesis, a full map of both compressive and tracking forces is needed. However, obtaining the tension map with laser ablation requires months of work for a given developmental stage, as it is possible to perform only one ablation on one embryo. Part of my work was thus to implement an alternative method to map out forces in a real time and non invasive manner and to identify the sources of these forces, i.e. the cells or tissues that exert compression and/or traction on the OP neurons.

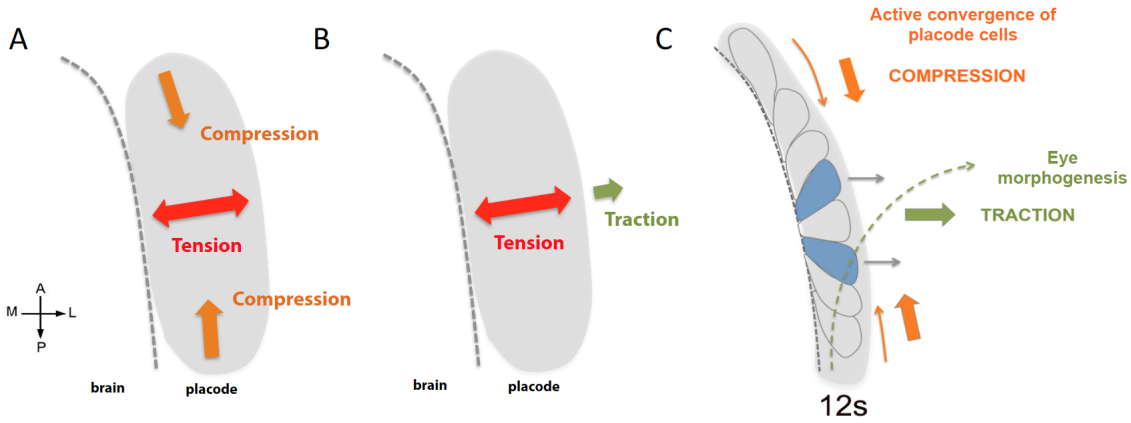

Figure 4.6 | **Working hypotheses**. Possible sources of extrinsic mechanical forces driving retrograde axon extension in the olfactory circuit: (A) compression exerted by actively converging cells from the placode extremities or (B-C) traction exerted by the adjacent eye morphogenetic movements. Adapted from [22].

4.3 Oil droplet to map out deformations and forces

The method relies on the use of oil droplets as force sensors in the OP. Indeed, when a droplet of oil is injected in the intercellular space of a living embryonic tissue, adjacent cells exert forces on it, which is possible since the mechanical properties of such droplets are close to those of cells. The applied forces cause deformation of the droplet from its equilibrium spherical shape (Fig. 4.7A). Knowing the surface tension of the droplet and analyzing its deformation, it is possible to extract the forces causing this deformation.

Proofs of concept for the feasibility of droplet injection in live tissues has already been shown by Campas and colleagues [28, 127]. They introduced fluorescent oil droplet in different regions along the anteroposterior axis of zebrafish embryo in order to establish the role of mechanical forces in body elongation (Fig. 4.7B). By fitting the droplet with an ellipse, they characterized its deformation and orientation, and extracted the stress values along the AP axis of the embryo (Fig. 4.7C). Their data indicate that extrinsic stresses can guide morphogenetic flows in the zebrafish. Therefore, injecting an oil droplet as a sensor of cellular forces has proven to be a valid method to study mechanical aspects of morphogenesis.

While detection of traction forces requires an adhesion between the droplet and the surrounding cells, compression forces can be measured with a simple passive droplet. For this reason, we started the force detection in the OP with compressive forces. To this end, we have used soybean oil droplets fluorescently labeled with Nile Red. I will now describe the details of the protocol used for the experiments.

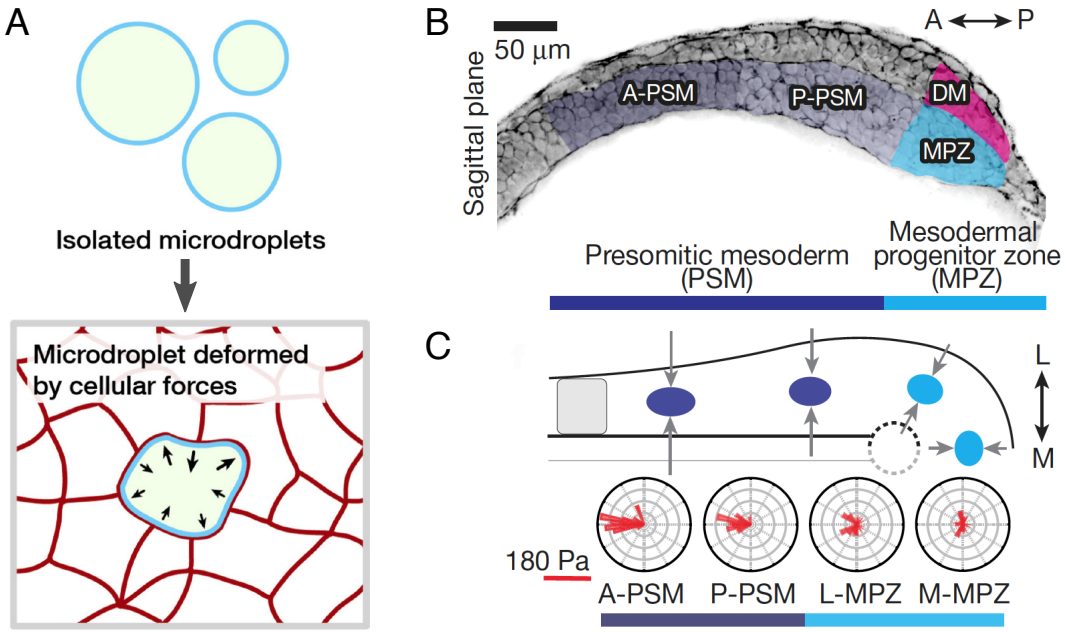

Figure 4.7 | Sketch of isolated spherical oil droplets in solution (top panel) and a droplet injected between the cells of the embryonic tissue (bottom panel); the deformation of the droplet results from the local cellular forces. Adapted from [28]. (B) Confocal sections along the anteroposterior axis of a zebrafish embryo. The PSM is divided into the anterior (A-PSM) and posterior (P-PSM) regions and the MPZ is divided into the lateral (L-MPZ) and medial (M-MPZ) regions. (C) Sketch showing the average droplet orientation along the anteroposterior axis and the posterior-to-anterior increase in mediolateral constriction (arrows) in the PSM. The polar plots give the orientation of the long axis of the droplets with respect to the anteroposterior axis. Adapted from [127].

4.3.1 Oil preparation and injection

We labeled soybean oil with Nile Red. For this, 5 ml of soybean oil (Sigma Aldrich) is mixed overnight with 300 μl of acetone saturated with Nile Red (Sigma Aldrich) under magnetic stirring at room temperature. After that, surfactant Tween 20 (Sigma Aldrich) is added to the filtered oil (Millex-SV 5.0 μm filter) with a final concentration of 2 mg/ml. Finally, Egg-PC lipids are diluted in the oil (2 mg/ml) using the technique described in Chapter 2. Addition of Tween 20 to phospholipids allows to obtain stable and well-deformable droplets. Such oil can be stored in a place protected from light for several weeks. Our collaborators, Marie Breau, Girish Gangatharan and Pauline Monnot, then inject with a microinjector a small quantity of oil that form a droplet into the OP area of zebrafish embryos at $\approx$ 17 hpf (hours post fertilisation). The diameter of the final droplet is about 15-20 μm, which is comparable to the size of cells in the OP. After that, the droplet is imaged through confocal microscopy (Fig. 4.8A). Z-stacks of the droplets are made starting 90 minutes after the oil injection and until photobleaching ($\approx 5h$). The droplet is imaged every 30 minutes. Altogether, we take around 10 z-stacks (i.e. timepoints) per experiment, which is enough to cover the formation of the OP.

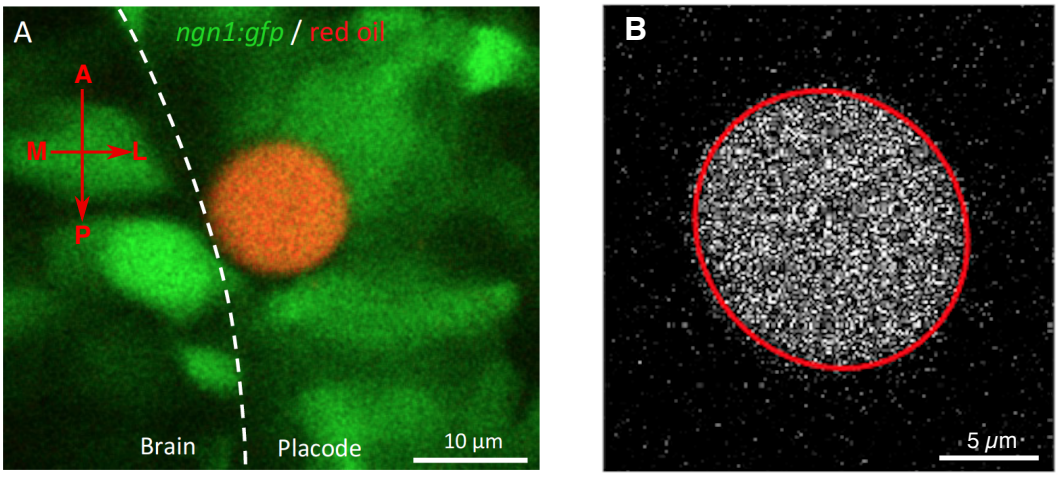

Figure 4.8 | **Oil droplet injected in the OP region of a zebrafish embryo.** (A) A 10-20 μm red fluorescent oil droplet is injected in the OP centre of a ngn1:gfp embryo, in which OP neurons express cytoplasmic GFP. Photo done by G. Gangatharan and P. Monnot. (B) Equatorial plane of the droplet fitted with an ellipse (red solid line).

We analyzed the acquired images using a custom-made Matlab routine. Images are first thresholded, and, following Mongera *et al.* [127], the droplet is fitted with an ellipse (Fig. 4.8B). To characterize the droplet deformations, we measure the eccentricity of the fitted ellipse defined as $(\frac{b-a}{b})$, where b is the major axis and a is the minor axis of the fitted ellipse. We also measure its orientation (the angle between the major axis and the mediolateral axis of a zebrafish embryo) for each time point.

4.4 Results

First, we checked if the droplet deformation evolved during the observed time interval. For this, we averaged the eccentricity and orientation of the fitted ellipses for images from the same experiment corresponding to droplet's equatorial plane. The later was selected from the z-stack based on the fitted ellipse with the largest area. As it can be seen on Fig. 4.9A, there is no clear trend observed in time neither for the eccentricity, nor for the orientation of the droplet. It suggests that compression forces do not change typically over the time of observation. We then tracked the average eccentricity and orientation of the droplet for each experiment (Fig. 4.9B). The data shows that in almost each experiment (6 out of 7) the droplet (i.e. the major axis of the fitted ellipse) is oriented along the mediolateral axis, with eccentricities between 0.032 and 0.057. Such orientation suggests that the droplets are compressed in the anteroposterior direction, which corresponds to our hypothesis that convergent neurons exert compression forces on the cells located in the central region of the OP.

We performed control experiments in which we injected a droplet of the same composition in a liquid agarose gel. After solidification of the gel, we imaged the droplet with the same confocal

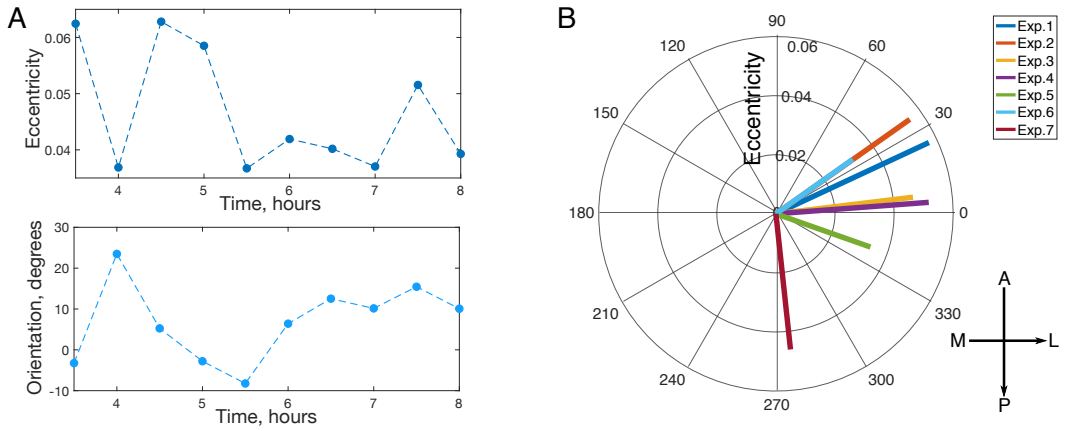

Figure 4.9 | **Eccentricity and orientation of droplets inserted in the OP region.** (A) Time evolution of the droplet eccentricity and orientation in the OP does not show any trend. (B) Most of the droplets (n = 6/7) are oriented in ML-direction, suggesting the presence of a compression along the AP axis.

microscope. In this case, there are *a priori* no external forces, and we thus expect the droplet to remain spherical, and the values of its eccentricity to be close to zero. We find that the eccentricity of the droplets injected in the agarose gel is indeed lower then those in the placode and always lies between 0.0014 to 0.03 (Fig. 4.10).

Finally, to verify how sensible our droplets are to the compression, we injected them in the presomitic mesoderm (PSM) of the zebrafish embryo - the region where the strongest compressive forces have been mapped out [127]. This time, we find that all the droplets are deformed along the anteroposterior axis in agreement with the work of Mongera *et al.* [127], with eccentricities between 0.05 and 0.1 (Fig. 4.10).

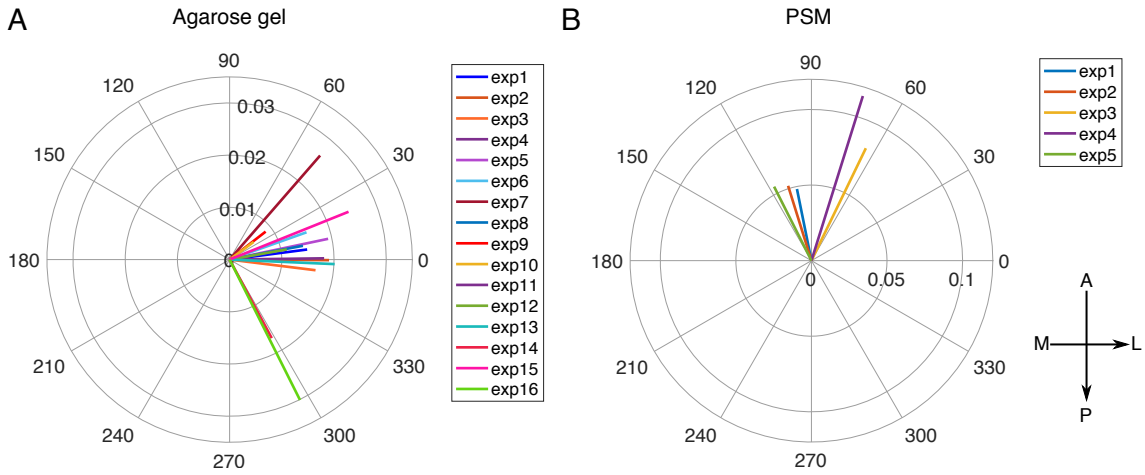

Figure 4.10 | **Negative and positive controls.** Eccentricity and orientation of the droplets injected in (A) agarose gel (negative control) and (B) PSM region (positive control).

In order to compare the eccentricity and orientation of the droplets injected in the OP, the

PSM and the agarose gel, we averaged the values of the eccentricity and orientation for each group of experiments. Results are presented in Fig. 4.11. The strongest deformation (0.067 ± 0.026) is observed for the droplets in the PSM region with an orientation in the anteroposterior direction (87.7° ± 23.5°). However, the average eccentricity in our case is one order of magnitude smaller compared to the measurements of [127] (0.067 vs 0.35), which suggests that our droplets are less deformable than those of Mongera *et al.*. The droplets injected in the OP are deformed along the mediolateral axis (the mean eccentricity equals 0.046 ± 0.01 and mean orientation is 0.5° ± 42°) corresponding to our hypothesis that compression forces are exerted in the anteroposterior direction. Finally, the droplets in agarose gel show the lowest mean eccentricity of 0.016 ± 0.007 and mean orientation of 5.5° ± 30.7°.

The difference between the eccentricity and the orientation of the droplets injected in the OP, the PSM and the agarose gel can be evidenced also on box-plots (Fig. 4.11B,C). We also checked whether the difference between these groups is significant. Statistical analysis. showed that the groups are different for the value of eccentricity. Concerning the orientation, the droplets injected in the PSM region showed significant differences from the droplets injected in OP or agarose gel. However, we found that there was no difference in orientation between the droplets in the OP and agarose gel.

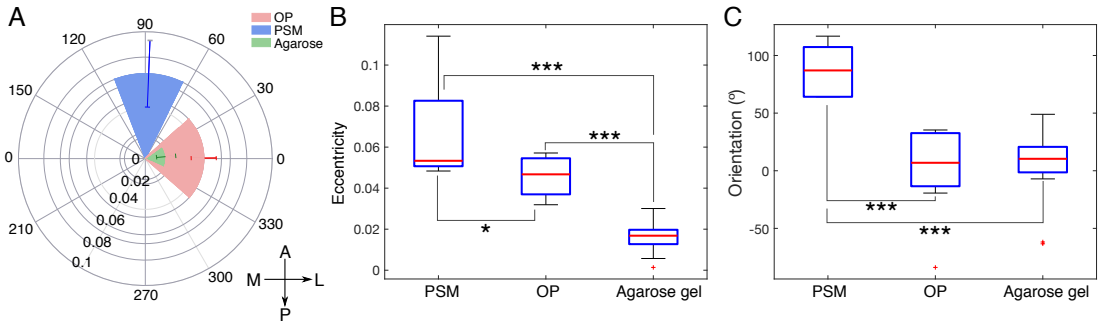

Figure 4.11 | **Comparison between droplets injected in PMC, OP and agarose gel.** (A) Polar plot showing eccentricity and orientation of droplets in OP (pink), PSM (blue) and agarose gel (green). (B-C) Box-plot shows the difference of eccentricity (B) and orientation (C) for three groups of droplets.

Our results demonstrate the existence of anisotropic compression forces exerted on neurons in the central region of the olfactory placode. However, the low values of droplet deformation in the OP compared to the ones in the PSM do not allow to conclude that the strength of the measured compression is enough to solely cause a passive retrograde axon extension.

4.5 Conclusions

In this part of my project, we implemented a method to measure *in vivo* forces arising during morphogenesis. Using oil droplets injected in zebrafish embryos, we measured compression deformations exerted in the central region of the olfactory placode during its formation. We also

performed positive and negative controls in order to verify our measurements. Overall, the obtained results prove the efficiency of the technique to sense the compressive forces in embryos. By revealing a mediolateral deformation of injected droplets in the OP, we evidenced the existence of compression forces along the anterioposterior direction. These findings are in agreement with our working hypothesis that passive retrograde axon extension in zebrafish can be caused by forces exerted by actively converging cells from the placode extremities. However, the measured values of the eccentricity of the droplet in the OP are lower compared to those measured in the PSM region, that are themselves lower than those measured by Mongera *et al.* Such low values of eccentricity in the PSM region can indicate that our droplets are less deformable than those which were used by Mongera *et al.* We are currently measuring the surface tension of the oil we used to make the droplets in order to provide an estimate of the related compressive forces. Only after that, it will be possible to conclude whether compression forces are sufficiently large to cause the retrograde axon extension. In addition, to obtain the full force map, we have to measure the traction forces as well. The first steps that were already taken in this direction, as well as future steps which will be done to finilize the study, will be described in the next chapter.

Chapter 5

Conclusion and Perspectives

In my PhD work, I demonstrated the possible role of mechanical pathways in tissue remodelling and morphogenesis. That was done with two complementary approaches:

1) *in vitro* studies of the effect of cell-cell adhesion on the elasto-plastic behavior of tissue mimicking emulsions;

2) *in vivo* measurements of cellular deformations induced by compressive forces in zebrafish embryos during the development of the olfactory neural circuit.

The first approach allowed us to address a complex biological question using Soft Matter Physics. Within this Soft Matter framework, we were able to study the sole contribution of the mechanical aspects of tissue remodelling without the biochemical pathways that necessarily overlap in biological systems. In addition, the use of biomimetic emulsions as a mechanical model of tissues enabled us to apply the developed tools and knowledge of Physics of granular materials to the biological questions.

In the mean time, the second approach provided us with a direct evaluation of the role of mechanical forces in living organisms. In long term perspective, this approach enebles one to observe a full scope of the interplay between biomechanical and biochemical pathways. Moreover, working *in vivo* can allow not only to study the mechanical properties themselves, but also to reveal the biological origins of these properties by using zebrafish mutants with cytoskeleton defects of different cells.

In the following, I would like to summarize both aspects of my PhD work and describe their possible future development.

5.1 Effect of adhesion on the elasto-plastic behavior of tissue mimicking emulsions

In order to study the mechanical properties of tissues in a simplified framework, we developed an *in vitro* synthetic system based on the use of biomimetic emulsions forced to flow through a geometrical constriction. This type of flow was aimed at reproaching in the most basic way the remodelling of biological tissues during convergent extension. With this system, we studied both the elastic and plastic responses of these emulsions under mechanical perturbations, and probed how such elasto-plastic behavior was affected by non-specific and specific adhesion between the droplets.

We first used a system where adhesion was introduced through non-specific depletion forces. We revealed that even a relatively weak attraction between the droplets was sufficient to modulate the flow of monodisperse ordered emulsions. In particular, the introduction of depletion forces resulted in higher values of the average droplet deformation. The effect of the interdroplet attraction also manifested in the topological rearrangements of the droplets: a delay in the occurance of T1 events was observed with an increase of the depletion forces. However, the impact of such non-specific

attraction remained subtle, and could be evidenced only in the context of dynamic flow. Indeed, we did not observe any significant changes in the static packings of droplets neither for monodisperse, nor for polydisperse emulsions.

The effect of adhesion became even more remarkable when we introduced specific adhesion between the droplets as a way to mimic more faithfully the intercellular adhesion. Our experiments demonstrated that while specific adhesion did not affect the global rearrangement topology, it changed the dynamics of local T1 events. In particular, the interdroplet adhesion was found to oppose the rupture of droplet-droplet contacts, and thus to delay the droplets rearrangements. Such delays resulted in an exces of deformation both in the droplets involved in the rearrangements, and in the system on the global scale. Moreover, this specific adhesion did not only cause higher deformations, but also induced an elongation of the droplets along the longitudinal axis of the constriction.

These results may shed light on the role of cell-cell adhesion in tissues during embryogenesis. In the example of biomimetic emulsions, we indeed measured droplet alignment due to adhesion along the elongation direction. In biological elongated tissues, one could expect that a similar mechanism occurs and induces polarization of the cells. Such long-range cell alignment in the direction of tissue elongation could lead to symmetry breaking in tissues, and thus induce the activation of biochemical signalling pathways during morphogenesis.

5.1.1 Perspectives

Our study was a first step towards mimicking tissue remodelling with a synthetic soft matter system and paved the path for future unraveling of other biological mechanisms, such as the role of the ECM or differential adhesion during morphogenetic processes. Yet, to adress these new questions, a finer control of the interdroplet adhesion is required. For this, other types of binders should be used, such as DNA complementary strands or even cadherin molecules. This would allow to tune continuously the adhesion strength or to create more complicated adhesion patterns between neighboring droplets.

Actually, we already started to develop emulsions in which specific adhesion is introduced with DNA complementary strands. Varying the DNA sequence and its length, we can increase or decrease the adhesion strength. As a first step, we started to probe the role of adhesion on the static packings of biomimetic emulsions. We already addressed this question in this manuscript using depletion forces, but showed that these were not sufficient to change the topology of the emulsion static packings. However, adhesion energies introduced by biotin-streptavidin-biotin bonds or complementary DNA strands are orders of magnitude higher than those due to depletion attraction, and, therefore, one can expect a clearer signature of the effect of such adhesion on the topology of the packings.

We have thus compared 2D packings of three different polydisperse emulsions: non-adhesive, adhesive and partially adhesive. Packings of non-adhesive droplets were prepared with streptavidin

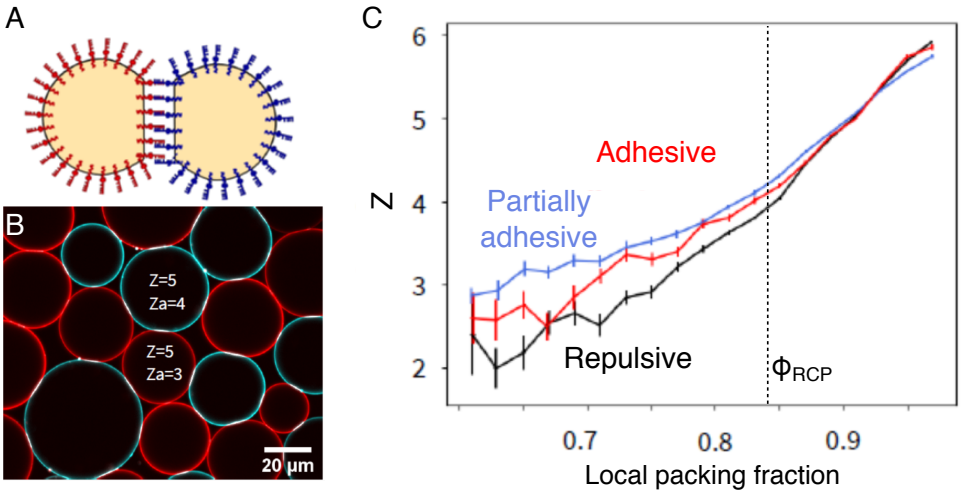

Figure 5.1 | (A) Sketch of two oil droplets coated with complementary C (blue) and D (red) DNA strands. (B) Confocal image of a 2D packing of the partially adhesive emulsion. Droplets are coated with complementary DNA strands. In this way, a contact between two droplets coated with different DNA strands (blue - red) is adhesive, while a contact between droplets of the same color is non-adhesive. (C) The total number of contacts (adhesive and non-adhesive) Z as a function of the local packing fraction plotted in log-log scale. Both adhesive and partially adhesive emulsions show an excess of contacts compared to repulsive emulsions for packing fractions below RCP. Error-bars are calculated as the standard error.

or DNA coated droplets without the salts that are needed to trigger the adhesion. Adhesive emulsions were prepared using streptavidin in the same way as it was described in this manuscript. Finally, partially adhesive packings were prepared with two sets of complementary DNA strands, that we will refer to as C and D for the sake of simplicity. Droplet coated with the C DNA can bind only to droplets coated with the D DNA, but not to those with the C DNA, and vice versa (Fig. 5.1A).

We first studied the topology of the droplet packings by examining the relationship between the local packing fraction ϕ_l and the total number of contacts Z (both adhesive and non-adhesive) each droplet has with its neighbors. As shown on Fig. 5.1C, for $\phi_l > \phi_{RCP}$ and all three types of emulsions, the curves $Z(\phi_l)$ collapse on the same master curve and are linear, as predicted in the literature [18]. However, for $\phi_l < \phi_{RCP}$, both adhesive and partially adhesive emulsions clearly exhibit, within experimental error bars, an excess of contacts compared to the repulsive case, without any significant difference between adhesive and partially adhesive cases . These observations suggest that adhesion stabilizes more contacts between the droplets for packing fractions below ϕ_{RCP} by adding an energetic cost to rupture of an adhesive contact between the droplets. Meanwhile, for packing fractions above ϕ_{RCP}, compressive forces put all neighboring droplets in contact for both adhesive and repulsive emulsions, thus eliminating the effect of the adhesion.

We also studied the deformation of the droplets as a function of local packing fraction by measuring the shape factor $\mathcal{A}$, defined in Chapters 2 and 3. Intuitively, the interdroplet adhesion should induce additional deformations, and thus higher values of $\mathcal{A}$, due to adhesion patches that

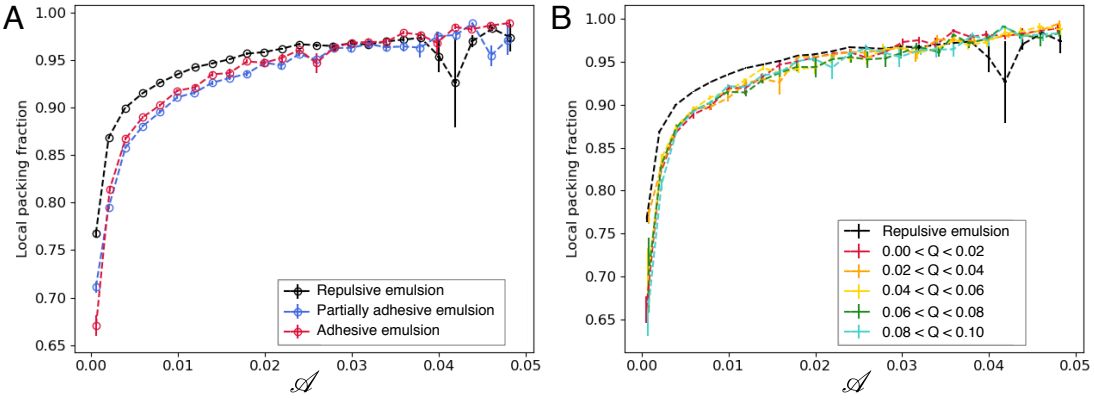

Figure 5.2 | (A) Local packing fraction ϕ_l as a function of the shape factor $\mathcal{A}$. For a given packing fraction, both adhesive and partially adhesive emulsions are characterized by higher value of $\mathcal{A}$ compared to the repulsive case. (B) Local packing fraction ϕ_l as a function of the shape factor $\mathcal{A}$ for the repulsive emulsions and partially adhesive emulsions separated based on their Q. The curves collapse for all measured values of Q.

flatten the contact area between contacting droplets. Indeed, when the local packing fraction ϕ_l is plotted against $\mathcal{A}$, we find that for almost all values of ϕ_l, $\mathcal{A}$ is higher for adhesive and partialy-adhesive emulsions compared to non-adhesive emulsions (Fig. 5.2A). However, for very high values of packing fraction ($\phi_l > 0.97$), the curves for all three emulsions do overlap. Surprisingly, there is no observed difference between adhesive and partially adhesive emulsions. To further investigate these results, we separated the droplets of the partially adhesive emulsions into groups based on the ratio Q between the number of adhesive contacts Z_a and total number of contacts Z that each droplet has, $Q = Z_a/Z$. Indeed, as it can be seen in the picture of Fig. 5.1B, in the case of partially adhesive emulsions, a droplet may have both adhesive and non-adhesive contacts with its neighbors (depending on whether they are coated with C or D DNA strands). We then plotted $\mathcal{A}$ versus the local packing fraction for these separated groups of droplets (Fig. 5.2B). We see that all curves for partially adhesive emulsions overlap independently of their value of Q. Still, the droplets of adhesive packings without almost no adhesive contacts (*i.e.* the droplets with $Q < 0.02$) can be clearly distinguished from the droplets of repulsive packings. Our findings indicate that even the presence of a partial adhesion is sufficient to affect the static packings of emulsions and stabilize them at $\phi_l < \phi_{RCP}$.

As the next step, we plan to tune further the number of adhesive contacts one droplet can make with its neighbors by mixing in different proportions droplets coated with C or D DNA. This will allow us to eventually build a phase diagram representing the change in the emulsion packings as a function of the amount of adhesion in the system.

On longer time scales, the effect of this specific adhesion will be studied in new geometries that allow to apply multiple mechanical perturbations. For example, that can be done by pushing the emulsion through a wave-shaped microfluidic channel (Fig. 5.3). In such a device, the compression in the convergent parts of the channel is alternated with relaxation in the divergent parts of the channel, which would mimic better the complex force patterns during morphogenesis. In addition,

in the emulsions that we used for the experiments described in Chapter 3, the formation of adhesive patches took hours. Therefore, the broken patch could not be reformed on the timescales of our experiments, and after a rearrangement, droplets behaved as repulsive ones. However, using complementary DNA strands and tuning a concentration of salt, it is possible to reduce the time needed for the formation of new adhesive patches down to minutes, which should enhance the effect of adhesion on the droplet behavior. Finally, one could think of extending these results to 3D.

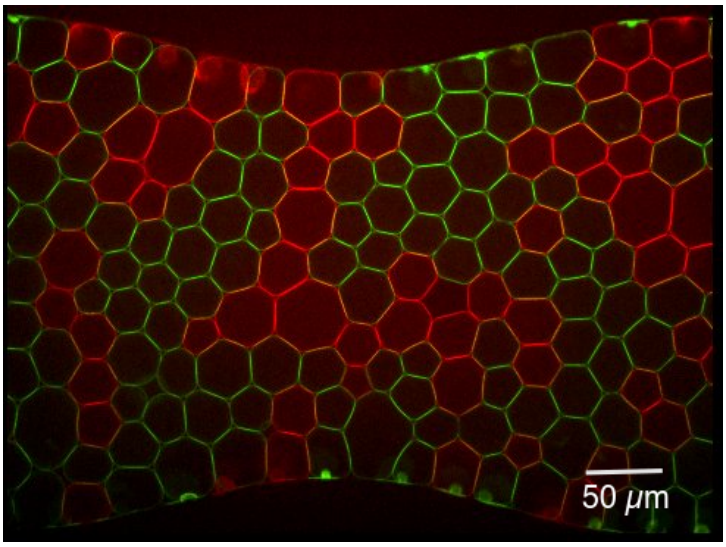

Figure 5.3 | A new design of a microfluidic device. The chosen geometry of the device allows to apply multiple mechanical perturbations on the flowing emulsion, thus alternating compression in the convergent parts of the channel with relaxation in the divergent ones. The emulsions are functionalized with the complementary C and D DNA strands, and are labelled with fluorescent streptavidin.

5.2 Measuring mechanical forces during the development of the olfactory placode in zebrafish

Eventually, the goal of this project is to use oil droplets to map compression and traction forces in the OP and to identify the sources of these forces, i.e. the cells or tissues that exert compression and/or traction on the OP neurons. We have already succeeded in obtaining a preliminary map of the deformations due to compressive forces in the OP by injecting a passive oil droplet in zebrafish embryos. Our preliminary results indicate the presence of AP compressive forces in the developing OP, which is consistent with the previously obtained tension map and compression hypothesis (Fig. 4.6). To consolidate these results, more droplet injections in wild type embryos should be performed.

In addition, for the moment we have limited ourselves to measuring only the deformations of the injected droplets, and have not yet extracted the corresponding values of compressive forces. In order to do this, we would have to make several assumptions. The most proper way to do it

would be evaluating the local stresses by measuring the deformations of the droplet surface as it was done in [28]. This method requires a precise visualization of the entire droplet surface, as well as elaborated computations. Nevertheless, the first approximation that should give an idea about the order of magnitudes of the compressive forces can be done in a simpler way. Indeed, as injected droplets have approximately the same sizes as the cells in the OP region, a droplet compressed in the embryo can be modelled as a droplet compressed between two parallel plates (analogous to a tissue aggregate compressed between parallel plates in a surface tensiometer), as it is shown in Fig. 5.4.

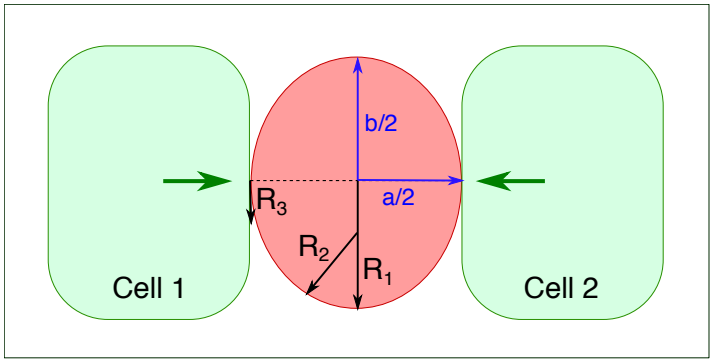

Figure 5.4 | Schematic representation of compression forces (green arrows) exerted on the oil droplet by neighboring cells in the OP of zebrafish embryo. The droplet is represented as an ellipse of major axis b and minor axis a.

In this case the ratio between surface tension and compressive forces is the same as the one used to determine the surface tension of tissue aggregates [53, 64] and is given by

$$\gamma = (\frac{1}{R_1} + \frac{1}{R_2})^{-1} \frac{F}{\pi R_3^2} \tag{5.1}$$

where R_1, R_2 are the principal radii of curvature of the deformed aggregate and πR_3^2 is the contact area between the aggregate and either of the neghboring cells. Knowing γ, one can thus estimate the compressive force as

$$F = \gamma(\frac{1}{R_1} + \frac{1}{R_2})(\pi R_3^2) \tag{5.2}$$

To first order, the droplet deformation can be approximated as the deformation of the ellipse that best fit the droplet. In this case $R_1 = b/2$, $R_2 = a/2$, and R_3 is roughly $R_1 - R_2$, where a and b are the minor and major axis of the fitted ellipse. Such calculations should provide approximate values of the compressive forces inside the zebrafish embryo. Thus, we will be able to check our measurements by comparing the obtained values for the forces in the PSM region with those reported for the same region in [127], and this should allow us to discuss about the possible role of compressive forces in the OP development.

5.2.1 Perspectives

With the technique we used so far, we measured the deformation of the droplets due to compressive forces. However, to map out the full force distribution (compression + traction) the droplets have to adhere to the surrounding cells. Indeed, if the cells around the droplets are under extension, those pulling forces will be transmitted through the cell/droplet adhesions and measured through droplet deformation. We thus need to functionalize the droplets with adhesion proteins which would bind tho the cells in the embryo. For instance, the droplets can be functionalized with cadherins or with antibodies against cadherins. However, for the moment, we have not succeeded in directly injecting oil in water emulsions or droplets in the zebrafish OP; instead we were injecting the small quantity of oil with the dissolved surfactants, that would eventually form a droplet directly in the embryo, similarly to other teams [127]. Such difficulties with the injection of droplets dispersed in a carrier liquid might be due to the density of the tissue in the OP region that cannot accommodate such dilute solutions of droplets. Therefore, in order to combine the bulk injection method with droplet functionalization, new formulations of the oil should be developed. One of the possible ways would be to dissolve directly the proteins of interest (e.g. cadherin) in the oil and let them co-stabilize at the interface with the other surface-active molecules present inside the oil (Fig. 5.5). Since cadherins in particular exhibit hydrophilic and hydrophobic parts, they should spontaneously enrich at the oil water interface once the droplet is formed in the tissue. Overall, this method should allow, after necessary calibrations, to form a functionalized droplet inside the zebrafish embryo, and thus to map out potential tracking forces.

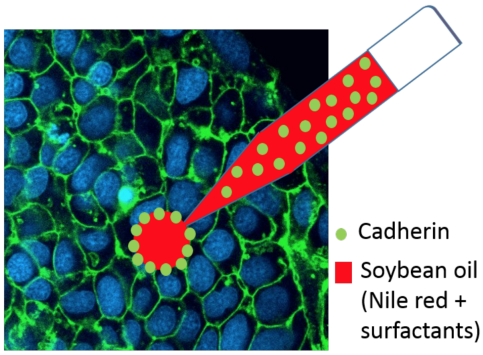

Figure 5.5 | Schematic view of droplet injection the zebrafish OP from an oil containing the cadherins (or anti-cadherin antibodies). OP cells are known to express cadherins at their surface. The properties of the oil will be tuned so that the cadherins relocate to the surface of the droplets upon injection.

Once pushing and pulling forces are determined, the next step will be to identify which cells in the OP exert these forces. For this, similar droplets should be injected in embryos where the potential sources of extrinsic forces are perturbed. For example, it can be embryos with impaired motility in the converging cells, or mutants in which the underlying eye tissue (associated to the traction hypothesis) is not present.

Appendix A

Article: Depletion attraction impairs the plasticity of emulsions flowing in a constriction.

Soft Matter

PAPER

View Article Online
View Journal | View Issue

Cite this: *Soft Matter*, 2020, **16**, 3294

Depletion attraction impairs the plasticity of emulsions flowing in a constriction†

Iaroslava Golovkova, [a] Lorraine Montel, [a] Elie Wandersman, [a] Thibault Bertrand, *[b] Alexis Michel Prevost [a] and Lea-Laetitia Pontani *[a]

Received 27th November 2019,
Accepted 5th March 2020

DOI: 10.1039/c9sm02343g

rsc.li/soft-matter-journal

We study the elasto-plastic behavior of dense attractive emulsions under a mechanical perturbation. The attraction is introduced through non-specific depletion interactions between the droplets and is controlled by changing the concentration of surfactant micelles in the continuous phase. We find that such attractive forces are not sufficient to induce any measurable modification on the scalings between the local packing fraction and the deformation of the droplets. However, when the emulsions are flowed through 2D microfluidic constrictions, we uncover a measurable effect of attraction on their elasto-plastic response. Indeed, we measure higher levels of deformation inside the constriction for attractive droplets. In addition, we show that these measurements correlate with droplet rearrangements that are spatially delayed in the constriction for higher attraction forces.

1 Introduction

The flow of particulate systems is a problem of great importance both theoretically and practically, with direct applications to the industry. It is relevant for a wide range of soft materials, from granular packings to foams and emulsions. While these materials present obvious differences, they share universal features, *e.g.* they generically undergo what is known as a jamming transition.[1,2] As the particle or droplet volume fraction ϕ increases, this rigidity transition between liquid and amorphous-solid states controls the phase behavior of these disordered solids. At a critical volume fraction ϕ_c (random close packing), the system jams and develops a yield stress.[3–6] The mechanical and rheological properties, such as the elastic modulus or the local pressure, of these systems are known to display a power law dependence with the distance to the jamming onset ($\phi - \phi_c$).[4,5,7–12]

Jammed solids are characterised by a spatially heterogeneous network of interparticle contacts, with a broad distribution of contact forces exhibiting an exponential tail[4,11,13,14] in which only a small subset of the particles sustain most of the mechanical load.[15–18] Below the yield stress, these systems respond elastically, while above it, they deform and flow plastically.[19] In these soft glassy flows, it was shown that stress and strain rates are coupled nonlocally.[6,20,21] In two-dimensional materials, the flow properties can easily be probed both at the microscopic and macroscopic scales.[22–31] As a consequence, previous experimental studies examined the microscopic rearrangements in a variety of two-dimensional model systems under stress.[32,33] This plastic flow is generically governed by local structural rearrangements which relieve stresses and dissipate energy.[6,22,23,34] Local plastic rearrangements have been connected to the fluctuating macroscopic flow in both simulations[35–39] and theoretical studies[6,20,21,40,41] of model systems. Nevertheless, the intimate link between the microscopic dynamics of an amorphous material and its macroscopic elasto-plastic response is still an open question for a broad class of more realistic materials.

In emulsions, the use of surfactants prevents the coalescence of the droplets and leads to short-range purely repulsive droplet–droplet interactions.[22,23,42] As such, dense stable emulsions are examples of jammed solids. In the last decades, a number of experimental works studied the structural, mechanical and rheological properties of purely repulsive emulsions.[12,42–47] In particular, as in other soft materials,[29,31,48–52] recent studies in quasi-2D flowing emulsions have also highlighted the importance of T1 events for local rearrangements and stress redistribution.[22,23] Monodisperse emulsions allow one to study material properties such as grain boundaries, dislocations and plasticity;[53–57] in particular, a recent study showed the existence of a spatiotemporal periodicity in the dislocation dynamics of these emulsions.[33] However, none of these studies have so far addressed the question of how interdroplet attractive forces modify the flow response of these emulsions.

Indeed, in a variety of natural settings and industrial applications, emulsion droplets do display additional attractive interactions that have been shown to change the nature of

[a] *Sorbonne Université, CNRS, Institut de Biologie Paris-Seine (IBPS), Laboratoire Jean Perrin (LJP), F-75005, Paris, France. E-mail: lea-laetitia.pontani@sorbonne-universite.fr*

[b] *Department of Mathematics, Imperial College London, South Kensington Campus, London SW7 2AZ, UK. E-mail: t.bertrand@imperial.ac.uk*

† Electronic supplementary information (ESI) available. See DOI: 10.1039/c9sm02343g

the jamming transition.[58–60] In contrast with the purely repulsive case, droplets in attractive emulsions can form bonds and thus a soft gel-like elastic structure which can sustain shear stresses below isostaticity.[45,61–63] However, the microscopic dynamics of the material, *i.e.* at the scale of the particles, was not explored. As a consequence, it is of particular importance to ask how the response to stress and in particular, the structural and mechanical properties of emulsions are modified by the presence of attractive interactions. Despite their broad applicability, our understanding of the influence of particle–particle interactions on the macroscopic properties of soft matter systems with attractive interactions is currently hindered by a crucial lack of controlled experimental settings.

In this article, we propose a first step towards completing our understanding of the microscopic origin for the macroscopic properties of adhesive emulsions. In particular, we study emulsions in which droplets interact through depletion attraction. First, we find that the static structure of 2D polydisperse emulsions remains unchanged by the introduction of depletion forces. However, the response of 2D monodisperse emulsions under mechanical constraint is impacted by the presence of depletion forces. Indeed, we flow the droplets through a microfluidic constriction in which they have to undergo elasto-plastic remodelling in order to go from a wide channel to a narrow one. In particular, we find that attractive droplets deform more inside the constriction, which we correlate to a shift in the positions of rearrangements. These findings show that depletion attraction forces are sufficient to modify the elasto-plastic response of dense emulsions under a mechanical perturbation. This attraction, even though it is not evidenced in static conditions, impairs rearrangements and in turn promotes an enhanced elastic response under flow.

2 Materials and methods

2.1 Emulsion preparation

Polydisperse emulsions are prepared using a pressure emulsifier (Internal Pressure Type, SPG Technology Co.). Silicone oil (viscosity 50 mPa s, Sigma Aldrich) is pushed through a cylindrical Shirasu Porous Glass membrane decorated with 10 μm pores, directly into a 10 mM SDS solution that is maintained under vigorous agitation. The resulting droplets display an average diameter of 42 μm (polydispersity 21%). In order to prepare the emulsion with both SDS concentrations, we use the same droplets and only replace their continuous phase. To do so, the emulsion is washed in a separating funnel in order to replace the continuous phase by solutions of 10 or 45 mM SDS in a water/glycerol mixture (60 : 40 in volume). This enhances the optical quality of the oil/water interface visualization through bright field and confocal microscopy.

For experiments in the constriction and in static packings, we use monodisperse emulsions with an average droplet diameter of 45 μm (polydispersity 3.9%). These emulsions are obtained with a custom made flow-focusing microfluidic set-up (channel size 60 μm × 60 μm, width at the flow-focusing junction 30 μm). We use the same oil and continuous phases for polydisperse and monodisperse emulsions.

2.2 Observation and image analysis of 2D static packings

When studying 2D static packings, we consider emulsions that are fluorescently labelled with Nile Red (Sigma Aldrich). To label the emulsion, we incubate it overnight in a SDS buffer (with [SDS] = 10 or 45 mM) saturated in Nile Red allowing the dye to partition between the oil and water phases over time. A 10 μL drop of emulsion is placed between a microscope glass slide (76 × 26 mm, Objekttrager) and a cover slip (24 × 60 mm, Knittel Glaser) separated by spacers (50 μm or 30 μm polymethylmethacrilate – PMMA-film, Goodfellow). Droplets are imaged through confocal microscopy (Spinning Disc Xlight V2, Gataca systems) using a 20× objective.

To study the local structure of these static packings, we use a custom Matlab (MathWorks) routine that works as follows. We first threshold the images and perform a watershed tessellation, we then measure the perimeter p and area a of each droplet as well as the area a_c of the associated watershed tesselation cell (see Fig. 1D). Following Boromand *et al.*,[64] we study the relation between the deformation of the droplets and their local packing fraction. To do so, we compute their shape factor $\mathscr{A} = p^2/4\pi a$ and determine the local packing fraction $\phi_l = a/a_c$. Note that we only consider droplets in the center of the packing, *i.e.* we exclude those that are partially cut by the edge of the image frame. The shape parameter $\mathscr{A}$ equals 1 for circular disks and is greater than 1 for all nonspherical particles.[65]

2.3 Experimental set-up for emulsion flow

We designed the constriction in a microfluidic channel composed of three main sections (Fig. 1): at the entrance, the channel is 50 μm deep and 200 μm wide over a 5 mm length, then at the constriction the width is reduced from 200 to 50 μm over a length of 200 μm, finally the channel remains 50 μm wide over a final 5 mm length. Note that the droplets are not confined in the vertical direction in this geometry since their diameter is slightly smaller than the height of the channel. The channel is made in polydimethylsiloxane using a negative cast micromachined in a block of PMMA (50 × 50 × 5 mm^3) using a desktop CNC Mini-Mill machine (Minitech Machinary Corp., USA). After passivating the channel with casein 0.05 mg mL^{-1} (β-casein from bovine milk, Sigma Aldrich) for 20 minutes, the emulsion is flowed in the device using a pressure pump (MFCS-8C Fluigent, P = 30 mbar). After droplets fill the constriction area, the pressure is decreased to stop the emulsion flow, and droplets are left to cream in the supply tube overnight, thus compressing the droplets in the microfluidic device in order to reach high values of packing fraction. After this passive compression phase, the emulsion is flowed again in the channel at a constant pressure. The flow of the droplets at the constriction is imaged in bright field microscopy with a 10× objective at a frequency of 20 frames per second (fps).

2.4 Image analysis of the emulsions flowing in the constriction

To analyse the videos of flowing emulsions, we first threshold the images to subsequently determine the center and perimeter

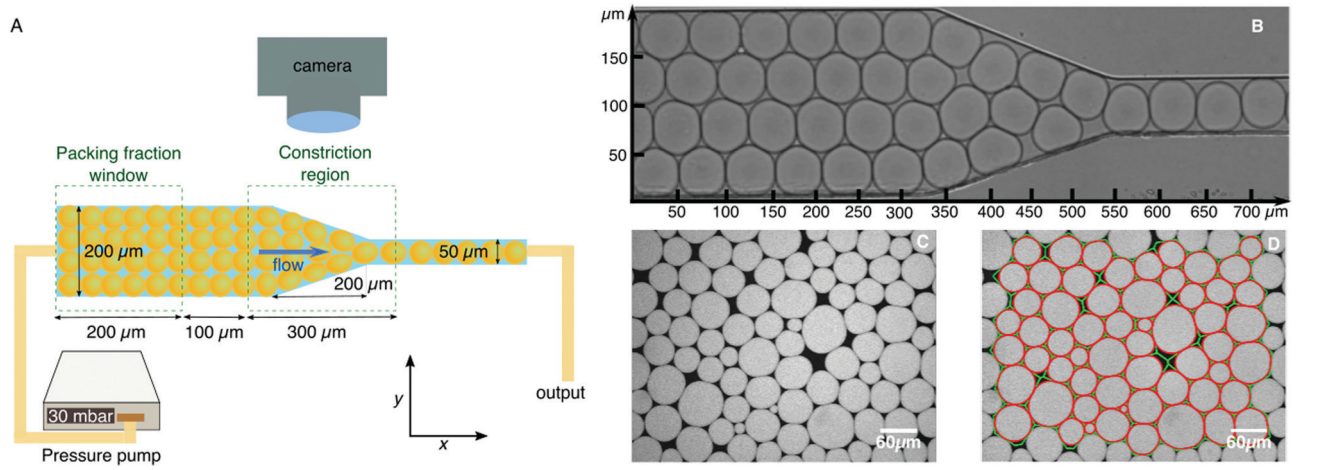

Fig. 1 Experimental set-up and image analysis – (A) the oil in water emulsion is pushed using a pressure pump (P = 30 mbar) through the microfluidic channel that consists of three parts: a 200 μm wide channel, a constriction, and a 50 μm wide channel. The depth of the channel is 50 μm over the whole length, and the diameter of the droplets is ≈45 μm. (B) Typical image of a monodisperse emulsion flowing in the constriction. In the area of the constriction, the flow of the droplets is imaged in bright field microscopy at 20 fps. The packing fraction of the emulsion is determined within the window of 200 × 200 μm located before the constriction area. (C) A typical confocal microscopy image of compressed 2D droplets at [SDS] = 10 mM. (D) Result of the image analysis performed on (C). Droplet contours are shown in red and watershed tessellation cells with the green curves. Based on these measurements, we calculate the local packing fraction ϕ_l as the ratio between the area of the droplet and that of its corresponding watershed tesselation cell, as well as the shape parameter $\mathscr{A}$.

of each droplet in the channel using a custom made Matlab routine. When studying droplet deformation, we only consider the droplets located in the constriction region. We define this area along the channel as a window that includes the 200 μm of the constriction itself, plus 50 μm before and after the constriction (Fig. 1). To quantify the deformation of each droplet, we use the approach proposed by Chen *et al.*[23] The perimeter of the droplet is interpolated and discretized at 1024 evenly spaced angles θ and the deformation d is calculated as a standard deviation of the radii $r(\theta)$ for each of these angles divided by the mean value of r:

$$d = \frac{\sqrt{\langle r^2 \rangle - \langle r \rangle^2}}{\langle r \rangle} \quad (1)$$

We also determine the global packing fraction of the emulsion in each video frame. To this end, we calculate the ratio between the sum of all droplets area and the area of the channel within the window of 200 × 200 μm located before the constriction region. Finally, frames are sorted according to the emulsion packing fraction, and the distributions of droplet deformations for each packing fraction are computed.

For rearrangements and flow analysis, the droplets were tracked using a custom Python routine and the FastTrack software (http://www.fasttrack.sh/). All droplets are sorted according to the lane they belong to in the channel ahead of the constriction. In our experiments, they are thus sorted into four lanes. The instantaneous velocity of the droplets was computed as the distance travelled between two consecutive frames acquired at a fixed frame rate $v(t) = \frac{\sqrt{(x(t+\mathrm{d}t) - x(t))^2 + (y(t+\mathrm{d}t) - y(t))^2}}{\mathrm{d}t}$. In our images the spatial resolution yields 300 nm per pixel.

3 Results

3.1 Analysis of static packings

We first study 2D static packings of monodisperse and polydisperse emulsions with two distinct depletion interactions. Using silicon oil droplets stabilized with two different concentrations of SDS (10 mM and 45 mM) allows us to change the depletion forces between the droplets. In our experiment, the continuous aqueous phase is supplemented in glycerol (40% in volume of glycerol). Note that in addition to allowing for a better imaging of the droplets, it also shifts the critical micellar concentration (CMC) of SDS. However, the CMC is only raised from 8 mM (in pure water) to about 9 mM in our experimental conditions,[66,67] which ensures that the system is still above the CMC under both SDS concentrations and that the surface tension remains the same when the concentration of SDS is increased from 10 to 45 mM. Above the CMC, depletion attraction forces increase linearly with the concentration of micelles,[68] which itself grows with increasing concentrations of SDS. Given the aggregation numbers of SDS (*i.e.* the number of SDS molecule per micelle at a given concentration) found in the literature,[69–71] we estimate that there is approximately 30 times more micelles at 45 mM SDS than at 10 mM SDS (see ESI†). Depletion forces at 45 mM SDS are thus expected to be 30 times larger than at 10 mM SDS.

To study the impact of depletion forces on static 2D packings, we first quantify the deformation of the droplets as a function of their local packing fraction in these monodisperse and polydisperse emulsions. Thus, we measure the asphericity and local packing fraction of each droplet in several images of 2D monodisperse and polydisperse packings for both 10 and 45 mM SDS concentrations (see Materials and methods).

In Fig. 2A, we first plot ϕ_l *vs.* $\mathscr{A} - 1$ for monodisperse emulsions for both SDS concentrations. Surprisingly, we find that data for both SDS concentrations are collapsing on the same master curve showing that the depletion-induced attractive interactions between the droplets have little effect on the structure of static packings.

To confirm the results we obtained for monodisperse emulsions, we also performed experiments on disordered packings (see Fig. 1C and D for an example of polydisperse emulsion). In Fig. 2B, we plot ϕ_l *vs.* $\mathscr{A} - 1$ for polydisperse emulsions for both SDS concentrations. Recent studies[64,65] developed a new numerical model to study the structural and mechanical properties of disordered 2D packings of bubbles and emulsions, including at high compressions. In the so-called deformable particle (DP) model, particles deform in response to mechanical constraints to minimize their perimeter while keeping their area fixed. This leads to a model of deformable disks with potential energies that include an energy term associated to the line tension and a penalization energy term quadratic in the change of area of the droplets, thus associated to their compressibility. Further, the deformable particles interact *via* a purely repulsive potential energy. Within the framework of this DP model and in our range of deformations, it was predicted that for disordered packings the distance to jamming onset $\phi_l - \phi_c$ scales with asphericity $\mathscr{A} - 1$ as

$$\phi_l - \phi_c = \alpha(\mathscr{A} - 1)^{\omega} \qquad (2)$$

with $\omega \approx 0.3$.

In the case of the disordered packings, we can compare our experimental data to this theoretical prediction. We find that the data for both SDS concentrations are well-fitted by eqn (2) with scaling exponent $\omega = 0.33$ and critical volume fraction $\phi_c = 0.842$, *i.e.* the scaling form obtained in the DP model. A summary of the fitting procedure and a table of all performed fits for both SDS concentrations are given in ESI.† While the results of the DP model were obtained for disordered systems, we also find that the change in local packing fraction as a function of droplet deformation in monodisperse emulsions is well described by the power law scaling in eqn (2) with, in this case, a scaling exponent $\omega \approx 0.25$ and a critical packing fraction $\phi_c = 0.91$ which can be explained by a high degree of crystallization.

These scalings are shown on a log–log scale in Fig. 2C, where we show that, in monodisperse emulsions (respectively polydisperse emulsions), data points corresponding to both depletion forces overlap and are captured by the same scaling function with $\phi_c = 0.91$ and $\omega = 0.25$ (respectively $\phi_c = 0.842$ and $\omega = 0.33$). This indicates that depletion induced attractive interactions do not affect significantly the scaling $\phi_l - \phi_c$ *versus* $\mathscr{A} - 1$, *i.e.* changing SDS concentration does not induce any measurable modification in the static packings of droplets. This might seem counterintuitive. Indeed, while it was shown that purely repulsive polydisperse emulsions become fluid-like below random close packing (*i.e.* only respond elastically above random close packing), experimental studies on the rheology of attractive emulsions showed that attractive emulsions are

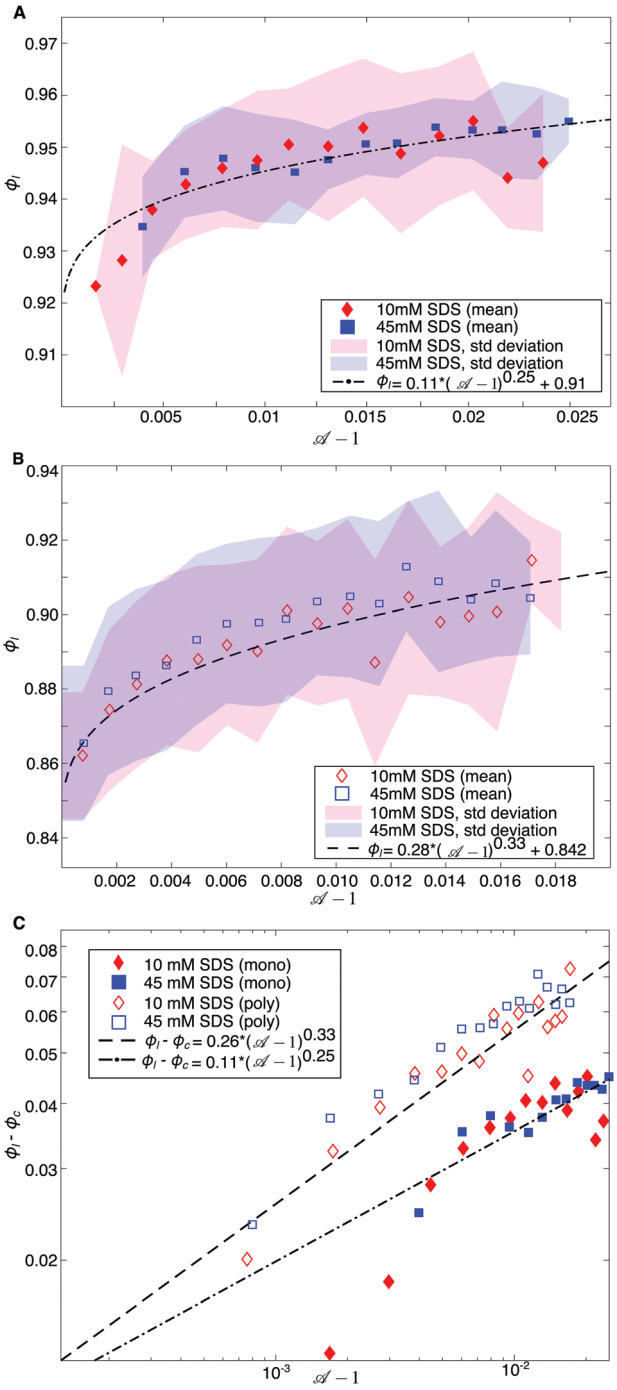

Fig. 2 Analysis of static 2D packings – local packing fraction ϕ_l *versus* $\mathscr{A} - 1$ for monodisperse (A) and polydisperse (B) emulsions. In (A), the experimental points (red diamonds for 10 mM SDS, blue squares for 45 mM SDS) are plotted together with the scaling function in eqn (2) with exponent $\omega = 0.25$ and $\phi_c = 0.91$ (black dot-dashed line). In (B), the experimental points (red open diamonds for 10 mM SDS, blue open squares for 45 mM SDS) are plotted together with the DP model, *i.e.* scaling function in eqn (2) with exponent $\omega = 1/3$ and $\phi_c = 0.842$ (black dashed line). (C) Log–log plot of $\phi_l - \phi_c$ *versus* $\mathscr{A} - 1$ for monodisperse and polydisperse emulsions for both SDS concentrations. We used $\phi_c = 0.91$ and $\phi_c = 0.842$ for mono and polydisperse packings respectively. The total number of droplets for: (1) polydisperse emulsions are $N = 1193$ and $N = 1735$ for 10 and 45 mM SDS respectively and (2) monodisperse emulsions are $N = 630$ and $N = 530$ for 10 and 45 mM SDS respectively.

elastic both below and above random close packing hinting at the fact that loose emulsions can be stabilized by attraction.[63] Here, we do not observe any significant change in ϕ_c for static packings with depletion interactions. In our SDS stabilized emulsions, the droplets are essentially frictionless and thus are free to roll. In such a system, the slightest amount of compression will lead to a rearrangement of the structure without noticeable deformation of the droplets until their purely repulsive jamming packing fraction is reached. This intuition is confirmed by the measured values of ϕ_c which correspond to random close packing $\phi_{RCP} \approx 0.842$ for the polydisperse (disordered) emulsions and to hexagonal close packing $\phi_{HCP} = 0.91$ for the monodisperse emulsions.

Despite the fact that static packings cannot be distinguished as a function of depletion forces, we reveal in what follows that significantly distinct behaviors can be evidenced in the context of a dynamic flow.

3.2 Emulsion flow in a constriction

In order to study their response under mechanical perturbations, monodisperse emulsions are flowed in microfluidic channels exhibiting a single physical constriction (Fig. 1). In particular, we use monodisperse droplets whose diameter is comparable to the channel height, constraining the system to a 2D monolayer of droplets. We focus our analysis on the area of the constriction in which droplets have to rearrange and deform in order to go from a large channel into a narrower one. The width of the narrow channel is chosen such that it only allows for the passage of one droplet diameter (Fig. 1) in order to maximize the number of rearrangements.

A typical experiment is carried out in two phases. The channel is first filled with the emulsion using a pressure pump. After a waiting time (see Materials and methods), the pressure is increased again so that this packed emulsion can flow in the channel. We usually require a typical pressure of the order of 30 mbar to establish a continuous flow. For each experiment, we image the droplets upstream, in order to evaluate their packing fraction, as well as inside the constriction to measure their deformation. We choose to quantify the deformation d of each droplet in the channel through the standard deviation of droplet radii as previously done[23] (see Materials and methods).

3.3 Deformation along the channel

We first study the deformation of the droplets inside the channel. To do so, we measure the packing fraction of the emulsion in a window located upstream of the constriction (on the left of the image) and that encompasses 200 μm of the channel length (Fig. 3A). We show in Fig. 3 the average deformation $\langle d \rangle$ along the channel for both SDS concentrations.

The obtained curves differ for the two SDS concentrations both in the constriction region and in the thinner channel. For both conditions (Fig. 3B and C) the deformation builds up in the constriction to a first maximum average deformation until it is released to a lower value of $\langle d \rangle$ at $x \approx 450$ μm. Then the deformation builds up again to a second maximum and is decreased to a lower deformation. Qualitatively, this behavior

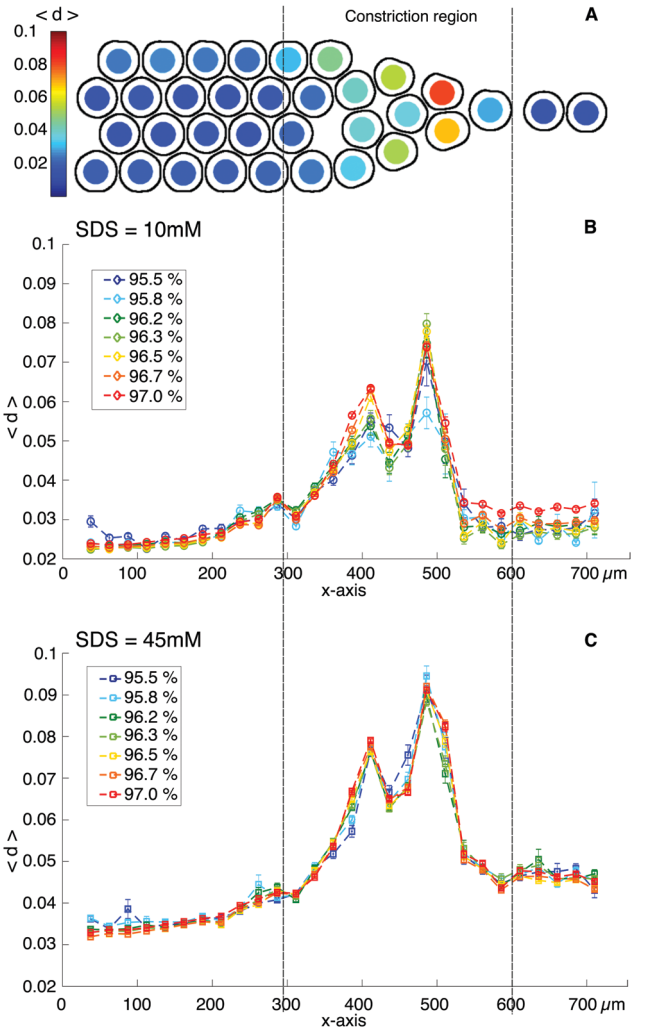

Fig. 3 Analyzing the droplet deformation in the constriction – (A) still snapshot of the image analysis in the channel at a given instant for an attractive emulsion ([SDS] = 45 mM). The color of the droplets codes for their deformation d calculated for their detected contours displayed on the image. (B and C) Average deformation of the droplets along the x-axis of the channel for different packing fractions in (B) the low attraction case ([SDS] = 10 mM) and (C) high attraction case ([SDS] = 45 mM). The deformation is averaged in bins that are 25 μm wide along the x-axis. The average deformation peaks inside the area of the constriction for both conditions. The error bars correspond to the standard error of the mean for the distributions of d obtained in each bin. The total number of droplets, combining all packing fractions, is $N = 27\,219$ for 10 mM SDS and $N = 91\,391$ for 45 mM SDS.

can be explained as the signature of a local stress release after a rearrangement. Indeed, Chen *et al.*[23] showed that in compressed emulsions, T1 events were immediately followed by a local decrease of deformation inside compressed emulsions. Here the localized peaks indicate that droplet rearrangements indeed occur at positions that are set by the topology of the packing in the channel.[33]

The other difference between the two conditions can be observed in the thinner channel region, after the constriction, where droplets enter one by one and release their deformation. In the case of low depletion forces ([SDS] = 10 mM), droplets

relax to a deformation value that is close to the initial one at the entry of the channel ($\langle d\rangle_{out} - \langle d\rangle_{in} \approx 0.0025$). However, with high depletion forces ([SDS] = 45 mM), droplets relax to a plateau at higher values of deformation than at the entry ($\langle d\rangle_{out} - \langle d\rangle_{in} \approx 0.01$). This impaired relaxation could be a signature of long range effects that could also explain why droplets enter the constriction with a slightly higher value of deformation in the high attraction case.

3.4 Deformation as a function of packing fraction

To further confirm these observations, we study the distribution of deformation of all droplets at all positions inside the constriction (taken in a window whose length spans 50 μm before and after the constriction – see Materials and methods). Since the global packing fraction can evolve over the course of one experiment, we separate each experiment into stacks according to their upstream packing fraction. We then pool together the image sequences corresponding to the same packing fraction throughout all performed experiments, for each concentration. Note that we also checked that the deformation in the constriction does not depend on the instantaneous droplet velocity within the investigated range (from 120 to 360 μm s^{-1}, see ESI†).

We compare the distributions of the deformations observed for different packing fractions and for each SDS concentration (Fig. 4). The distributions peak at smaller values of deformation in the low attraction case than in the case of strongly attractive droplets (Fig. 4A). This shift can also be clearly evidenced when plotting the cumulative distributions for each condition at various packing fractions (see Fig. 4B). As expected, for low depletion forces (10 mM SDS) we find that the distributions exhibit lower values of deformation in all conditions. When attraction is introduced between droplets, all curves are shifted to higher values of deformation.

In the previous section we showed that depletion alone was not sufficient to induce significant additional deformations in static packings of droplets. The shift observed in these deformation distributions must thus originate from differences in the local topological changes of the emulsions. Hence, we next examine the spatial location of rearrangements in the constriction as a function of SDS concentration.

3.5 Rearrangements and velocity distributions in the constriction

We here test the hypothesis that rearrangements are impaired by the attraction between the droplets, which would in turn force the droplets to deform more to overcome the constriction.

Since the size of the channel as well as the diameter of the droplets are fixed, there are always four lines of droplets flowing in the channel, ahead of the constriction, and one line after the constriction (Fig. 5A). In this framework, droplets will exchange neighbors to do the necessary rearrangements in given areas of the channel that are defined by geometry. We can thus estimate the distance Δx between two rearrangements by calculating the distance between the points where one can accommodate for 4 droplets and 3 droplets of diameter D in the

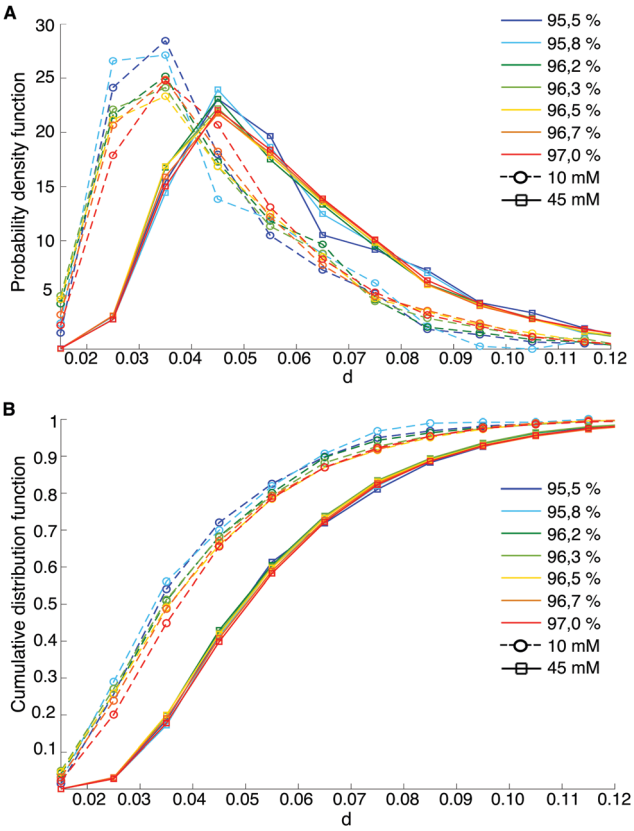

Fig. 4 Statistics of deformation under flow – (A) probability density function of the deformation d calculated in the constriction for different packing fractions in the case of low attraction forces ([SDS] = 10 mM, open circles) and high attraction forces ([SDS] = 45 mM, stars). (B) Cumulative distributions of the deformation d in the constriction for low attraction forces (open circles) and high depletion forces (open squares) for different packing fractions.

constriction. Knowing the slope of the constriction α this leads to $\Delta x = D/(2\alpha) = 60$ μm.

To study these rearrangements, we measure both the velocity and number of neighbors of the droplets along the channel. In the constriction, droplets are stalled transiently until they perform a rearrangement. This effect is evidenced by local minima in their individual velocity profiles as shown in Fig. 5B, that are separated by the expected distance between rearrangements Δx. We extract the positions of these minima in two specific areas of the channel, corresponding to zones of rearrangements, for each droplet in lines 1 and 4 for both SDS concentrations. We compare both conditions by plotting the cumulative distributions of the minimum velocity location in each zone (Fig. 5C). We observe that the distributions for attractive droplets are shifted by 7 μm and 4 μm in zones 1 and 2 respectively (measured shift at 50%), indicating that rearrangements are indeed delayed in the channel compared to the low depletion case. Similarly to the deformation, this shift does not seem to depend on the flow speed in the channel (see ESI†).

Furthermore, we analyzed the average number of neighbors per droplet along the constriction (Fig. 5D). Droplets in lines 1

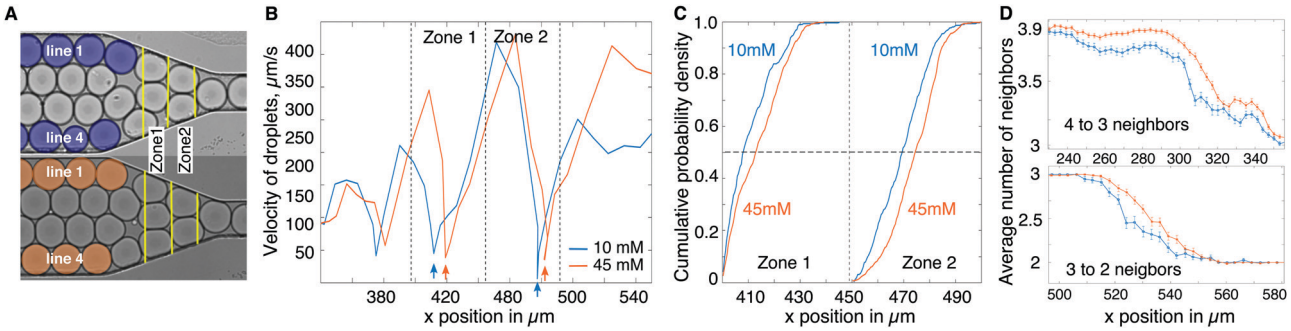

Fig. 5 Rearrangements and velocity distributions in the constriction – (A) image of droplets in the constriction for 10 mM (top, blue) and 45 mM (bottom, orange) SDS. The zones where the number of droplets decreases from 3 to 2 and from 2 to 1 are indicated with yellow lines and referred to as zone 1 and 2 respectively. (B) Typical velocity curves of individual droplets in lines 1 and 4 along the channel axis for 10 mM (blue) and 45 mM SDS (orange) emulsions. The velocity drops to a minimum value (indicated by an arrow) in zones 1 and 2 each time the droplets stall before a rearrangement. For each droplet trajectory we find the location of this minimal velocity to build panel (C). (C) Cumulative distributions of the minimum velocity location for lines 1 and 4. The 45 mM SDS droplets slow down farther into the constriction, as evidenced by the shift in distributions at 50% probability, by about 7 μm in zone 1 and 4 μm in zone 2. (D) Average number of neighbors per droplet along the channel for lines 1 and 4. For more attractive emulsions, the number of neighbors drops from 4 to 3 and then from 3 to 2 respectively 11 μm and 8.5 μm later in the constriction.

and 4 enter the constriction with 4 neighbors in a hexagonal lattice, and exit with 2 neighbors in the smaller channel. We measured the positions along the channel where droplets transition on average from 4 to 3 and from 3 to 2 neighbors respectively. We find that, for the more attractive emulsions, the transitions from 4 to 3 and from 3 to 2 neighbors are delayed by 11 μm and 8.5 μm respectively.

4 Discussion

Attractive interactions between particles are expected to affect their packing topology as well as their rheological and mechanical response to local mechanical perturbations. Below the jamming transition, previous work showed that attraction induced by depletion forces tuned significantly the structure of 3D packings and could mechanically stabilize them below the isostatic limit.[60] Above the jamming transition, one expects adhesive forces in packings of deformable spheres to change how droplet deformation and coordination numbers scale with the packing fraction.[64,65] To the best of our knowledge, this issue has been addressed neither in theoretical models nor in experimental systems.

In our experimental study, we provide a first step towards the understanding of the mechanical response of adhesive emulsions by introducing attractive interactions induced by depletion between oil droplets. We first evidence that such attraction forces are too low to induce any measurable effect in 2D static packings of droplets. Indeed, for both attraction forces, we recover the scaling laws predicted by Boromand *et al.*[64] for purely repulsive packings, with a critical packing fraction $\phi_c \approx 0.842$. However, using monodisperse emulsions, we uncovered distinct changes in their elasto-plastic response when the droplets are flowed through a 2D physical constriction. Note that recent numerical studies dealing with attractive soft sphere packings showed similarly that attractive packings with structures very similar to their repulsive counterpart (*e.g.* in the fact that the critical packing fraction is not significantly different) could have qualitatively different mechanical properties.[72] In our experiments, the first manifestation of attraction is an increase of the average deformation of the droplets in the constriction. The second one is the delay of topological rearrangements inside the constriction as attraction forces are increased. Depletion forces thus appear adequate to modulate the elasto-plastic response of emulsions in our system.

Such findings could be relevant for biological tissues in which adhesion controls to a large extent remodelling events that occur on timescales that are beyond those of cytoskeletal activity. In order to isolate the role of adhesion in biological processes, cellular tissues can indeed be mimicked with droplet assemblies connected by specific binders.[73–75] Within that framework, emulsions have been shown to exhibit similar mechanical properties and have for this reason been used to measure cellular forces both *in vitro*[76] and *in vivo*.[77,78] This reductionist approach could thus shed light on behavioral transitions in developing tissues upon adhesion modulation and will be the focus of future investigations.

Conflicts of interest

There are no conflicts to declare.

Acknowledgements

The authors thank Adèle Dramé-Maigné and Yannick Rondelez for providing flow focusing devices for the production of the emulsions, as well as Léa Pinon and Jacques Fattaccioli for allowing us to use the pressure emulsifier, they also thank Georges Debregeas and Zorana Zeravcic for fruitful discussions and acknowledge financial support from Agence Nationale de la Recherche (BOAT, ANR-17-CE30-0001).

References

1 A. J. Liu and S. R. Nagel, *Annu. Rev. Condens. Matter Phys.*, 2010, **1**, 347–369.
2 M. van Hecke, *J. Phys.: Condens. Matter*, 2009, **22**, 033101.
3 M. E. Cates, J. P. Wittmer, J.-P. Bouchaud and P. Claudin, *Phys. Rev. Lett.*, 1998, **81**, 1841–1844.
4 C. S. O'Hern, L. E. Silbert, A. J. Liu and S. R. Nagel, *Phys. Rev. E: Stat., Nonlinear, Soft Matter Phys.*, 2003, **68**, 011306.
5 P. Olsson and S. Teitel, *Phys. Rev. Lett.*, 2007, **99**, 178001.
6 J. Goyon, A. Colin, G. Ovarlez, A. Ajdari and L. Bocquet, *Nature*, 2008, **454**, 84.
7 C. S. O'Hern, S. A. Langer, A. J. Liu and S. R. Nagel, *Phys. Rev. Lett.*, 2002, **88**, 075507.
8 T. G. Mason, J. Bibette and D. A. Weitz, *Phys. Rev. Lett.*, 1995, **75**, 2051–2054.
9 M.-D. Lacasse, G. S. Grest, D. Levine, T. G. Mason and D. A. Weitz, *Phys. Rev. Lett.*, 1996, **76**, 3448–3451.
10 W. G. Ellenbroek, E. Somfai, M. van Hecke and W. van Saarloos, *Phys. Rev. Lett.*, 2006, **97**, 258001.
11 T. S. Majmudar, M. Sperl, S. Luding and R. P. Behringer, *Phys. Rev. Lett.*, 2007, **98**, 058001.
12 I. Jorjadze, L.-L. Pontani and J. Brujic, *Phys. Rev. Lett.*, 2013, **110**, 048302.
13 H. M. Jaeger, S. R. Nagel and R. P. Behringer, *Rev. Mod. Phys.*, 1996, **68**, 1259–1273.
14 J. Brujić, S. F. Edwards, I. Hopkinson and H. A. Makse, *Phys. A*, 2003, **327**, 201–212.
15 C. h. Liu, S. R. Nagel, D. A. Schecter, S. N. Coppersmith, S. Majumdar, O. Narayan and T. A. Witten, *Science*, 1995, **269**, 513–515.
16 M. E. Cates, J. P. Wittmer, J.-P. Bouchaud and P. Claudin, *Chaos*, 1999, **9**, 511–522.
17 T. S. Majmudar and R. P. Behringer, *Nature*, 2005, **435**, 1079–1082.
18 J. Zhou, S. Long, Q. Wang and A. D. Dinsmore, *Science*, 2006, **312**, 1631–1633.
19 D. T. Chen, Q. Wen, P. A. Janmey, J. C. Crocker and A. G. Yodh, *Annu. Rev. Condens. Matter Phys.*, 2010, **1**, 301–322.
20 K. Kamrin and G. Koval, *Phys. Rev. Lett.*, 2012, **108**, 178301.
21 L. Bocquet, A. Colin and A. Ajdari, *Phys. Rev. Lett.*, 2009, **103**, 036001.
22 K. W. Desmond and E. R. Weeks, *Phys. Rev. Lett.*, 2015, **115**, 098302.
23 D. Chen, K. W. Desmond and E. R. Weeks, *Phys. Rev. E: Stat., Nonlinear, Soft Matter Phys.*, 2015, **91**, 062306.
24 R. R. Hartley and R. P. Behringer, *Nature*, 2003, **421**, 928–931.
25 J. Lauridsen, G. Chanan and M. Dennin, *Phys. Rev. Lett.*, 2004, **93**, 018303.
26 A. Kabla, J. Scheibert and G. Debregeas, *J. Fluid Mech.*, 2007, **587**, 45–72.
27 B. Dollet and F. Graner, *J. Fluid Mech.*, 2007, **585**, 181–211.
28 B. Utter and R. P. Behringer, *Phys. Rev. Lett.*, 2008, **100**, 208302.
29 N. C. Keim and P. E. Arratia, *Phys. Rev. Lett.*, 2014, **112**, 028302.
30 N. C. Keim and P. E. Arratia, *Soft Matter*, 2015, **11**, 1539–1546.
31 J. Barés, D. Wang, D. Wang, T. Bertrand, C. S. O'Hern and R. P. Behringer, *Phys. Rev. E*, 2017, **96**, 052902.
32 J. Lauridsen, M. Twardos and M. Dennin, *Phys. Rev. Lett.*, 2002, **89**, 098303.
33 Y. Gai, C. M. Leong, W. Cai and S. K. Y. Tang, *Proc. Natl. Acad. Sci. U. S. A.*, 2016, **113**, 12082–12087.
34 A. Argon, *Acta Metall.*, 1979, **27**, 47–58.
35 D. J. Durian, *Phys. Rev. Lett.*, 1995, **75**, 4780–4783.
36 A. Kabla and G. Debrégeas, *Phys. Rev. Lett.*, 2003, **90**, 258303.
37 C. Maloney and A. Lematre, *Phys. Rev. Lett.*, 2004, **93**, 016001.
38 C. E. Maloney and A. Lematre, *Phys. Rev. E: Stat., Nonlinear, Soft Matter Phys.*, 2006, **74**, 016118.
39 V. Mansard, A. Colin, P. Chaudhuri and L. Bocquet, *Soft Matter*, 2013, **9**, 7489–7500.
40 M. L. Falk and J. S. Langer, *Phys. Rev. E: Stat. Phys., Plasmas, Fluids, Relat. Interdiscip. Top.*, 1998, **57**, 7192–7205.
41 G. Picard, A. Ajdari, F. Lequeux and L. Bocquet, *Eur. Phys. J. E: Soft Matter Biol. Phys.*, 2004, **15**, 371–381.
42 K. W. Desmond, P. J. Young, D. Chen and E. R. Weeks, *Soft Matter*, 2013, **9**, 3424–3436.
43 P. Hébraud, F. Lequeux, J. P. Munch and D. J. Pine, *Phys. Rev. Lett.*, 1997, **78**, 4657–4660.
44 P. Coussot, J. S. Raynaud, F. Bertrand, P. Moucheront, J. P. Guilbaud, H. T. Huynh, S. Jarny and D. Lesueur, *Phys. Rev. Lett.*, 2002, **88**, 218301.
45 L. Bécu, S. Manneville and A. Colin, *Phys. Rev. Lett.*, 2006, **96**, 138302.
46 P. Jop, V. Mansard, P. Chaudhuri, L. Bocquet and A. Colin, *Phys. Rev. Lett.*, 2012, **108**, 148301.
47 J. Lin, I. Jorjadze, L.-L. Pontani, M. Wyart and J. Brujic, *Phys. Rev. Lett.*, 2016, **117**, 208001.
48 M. Lundberg, K. Krishan, N. Xu, C. S. O'Hern and M. Dennin, *Phys. Rev. E: Stat., Nonlinear, Soft Matter Phys.*, 2008, **77**, 041505.
49 F. Graner, B. Dollet, C. Raufaste and P. Marmottant, *Eur. Phys. J. E: Soft Matter Biol. Phys.*, 2008, **25**, 349–369.
50 S. Cohen-Addad, R. Höhler and O. Pitois, *Annu. Rev. Fluid Mech.*, 2013, **45**, 241–267.
51 P. Marmottant, C. Raufaste and F. Graner, *Eur. Phys. J. E: Soft Matter Biol. Phys.*, 2008, **25**, 371–384.
52 D. Bi, J. H. Lopez, J. M. Schwarz and M. L. Manning, *Nat. Phys.*, 2015, **11**, 1074.
53 W. L. Bragg and J. F. Nye, *Proc. R. Soc. London, Ser. A*, 1947, **190**, 474–481.
54 P. Schall, I. Cohen, D. A. Weitz and F. Spaepen, *Science*, 2004, **305**, 1944–1948.
55 P. Schall, D. A. Weitz and F. Spaepen, *Science*, 2007, **318**, 1895–1899.
56 M. Arciniaga, C.-C. Kuo and M. Dennin, *Colloids Surf., A*, 2011, **382**, 36–41.
57 S. Arif, J.-C. Tsai and S. Hilgenfeldt, *J. Rheol.*, 2012, **56**, 485–499.
58 V. Trappe, V. Prasad, L. Cipelletti, P. N. Segre and D. A. Weitz, *Nature*, 2001, **411**, 772–775.
59 G. Lois, J. Blawzdziewicz and C. S. O'Hern, *Phys. Rev. Lett.*, 2008, **100**, 028001.

60 I. Jorjadze, L.-L. Pontani, K. A. Newhall and J. Brujić, *Proc. Natl. Acad. Sci. U. S. A.*, 2011, **108**, 4286–4291.
61 J. Bibette, T. G. Mason, H. Gang, D. A. Weitz and P. Poulin, *Langmuir*, 1993, **9**, 3352–3356.
62 P. Poulin, J. Bibette and D. Weitz, *Eur. Phys. J. B*, 1999, **7**, 277–281.
63 S. S. Datta, D. D. Gerrard, T. S. Rhodes, T. G. Mason and D. A. Weitz, *Phys. Rev. E: Stat., Nonlinear, Soft Matter Phys.*, 2011, **84**, 041404.
64 A. Boromand, A. Signoriello, J. Lowensohn, C. S. Orellana, E. R. Weeks, F. Ye, M. D. Shattuck and C. S. O'Hern, *Soft Matter*, 2019, **15**, 5854–5865.
65 A. Boromand, A. Signoriello, F. Ye, C. S. O'Hern and M. D. Shattuck, *Phys. Rev. Lett.*, 2018, **121**, 248003.
66 C. C. Ruiz, L. Diaz-Lopez and J. Aguiar, *J. Dispersion Sci. Technol.*, 2008, **29**, 266–273.
67 H. Khan, J. M. Seddon, R. V. Law, N. J. Brooks, E. Robles, J. T. Cabral and O. Ces, *J. Colloid Interface Sci.*, 2019, **538**, 75–82.
68 S. Asakura and F. Oosawa, *J. Polym. Sci.*, 1958, **33**, 183–192.
69 B. L. Bales, L. Messina, A. Vidal, M. Peric and O. R. Nascimento, *J. Phys. Chem. B*, 1998, **102**, 10347–10358.
70 B. Hammouda, *J. Res. Natl. Inst. Stand. Technol.*, 2013, **118**, 151–167.
71 G. Duplâtre, M. F. Ferreira Marques and M. da Graça Miguel, *J. Phys. Chem.*, 1996, **100**, 16608–16612.
72 D. J. Koeze and B. P. Tighe, *Phys. Rev. Lett.*, 2018, **121**, 188002.
73 L.-L. Pontani, I. Jorjadze, V. Viasnoff and J. Brujic, *Proc. Natl. Acad. Sci. U. S. A.*, 2012, **109**, 9839–9844.
74 L. Feng, L.-L. Pontani, R. Dreyfus, P. Chaikin and J. Brujic, *Soft Matter*, 2013, **9**, 9816.
75 L.-L. Pontani, I. Jorjadze and J. Brujic, *Biophys. J.*, 2016, **110**, 391–399.
76 D. Molino, S. Quignard, C. Gruget, F. Pincet, Y. Chen, M. Piel and J. Fattaccioli, *Sci. Rep.*, 2016, **6**, 29113.
77 O. Campàs, T. Mammoto, S. Hasso, R. A. Sperling, D. O'Connell, A. G. Bischof, R. Maas, D. A. Weitz, L. Mahadevan and D. E. Ingber, *Nat. Methods*, 2014, **11**, 183–189.
78 A. Mongera, P. Rowghanian, H. J. Gustafson, E. Shelton, D. A. Kealhofer, E. K. Carn, F. Serwane, A. A. Lucio, J. Giammona and O. Campàs, *Nature*, 2018, **561**, 401–405.

Appendix B

Article: Adhesion as a trigger of droplet polarization in flowing emulsions

Soft Matter

Accepted Manuscript

This article can be cited before page numbers have been issued, to do this please use: I. Golovkova, L. Montel, F. Pan, E. Wandersman, A. M. Prevost, T. Bertrand and L. Pontani, *Soft Matter*, 2021, DOI: 10.1039/D1SM00097G.

ROYAL SOCIETY OF CHEMISTRY

rsc.li/soft-matter-journal

View Article Online
DOI: 10.1039/D1SM00097G

Adhesion as a trigger of droplet polarization in flowing emulsions †

Iaroslava Golovkova,[a‡] Lorraine Montel,[a‡] Franck Pan,[b] Elie Wandersman,[a] Alexis M. Prevost,[a] Thibault Bertrand,[b] and Lea-Laetitia Pontani*[a]

Tissues are subjected to large external forces and undergo global deformations during morphogenesis. We use synthetic analogues of tissues to study the impact of cell-cell adhesion on the response of cohesive cellular assemblies under such stresses. In particular, we use biomimetic emulsions in which the droplets are functionalized in order to exhibit specific droplet-droplet adhesion. We flow these emulsions in microfluidic constrictions and study their response to this forced deformation via confocal microscopy. We find that the distributions of avalanche sizes are conserved between repulsive and adhesive droplets. However, adhesion locally impairs the rupture of droplet-droplet contacts, which in turn pulls on the rearranging droplets. As a result, adhesive droplets are a lot more deformed along the axis of elongation in the constriction. This finding could shed light on the origin of polarization processes during morphogenesis.

1 Introduction

During morphogenesis, cells both differentiate and self-assemble into tissues and organs with specific forms and functions. For instance, during gastrulation, the Drosophila embryo folds onto itself to produce the ventral furrow that eventually becomes the first tubular shape of the embryo, thus defining the inside-outside geometry of the future organism. This extensive remodeling of tissues is controlled by both biochemical pathways, through soluble morphogens[1–3], and biomechanical processes, through forces[4–6] and the regulation of cellular adhesion[7,8]. The behavior of tissues during morphogenesis is thus strongly determined by their mechanical response, which is controlled by a feedback loop between cellular adhesion and biochemical signaling through the cytoskeleton[9–13]. Figuring out the properties of the tissue from a materials standpoint is therefore of the utmost importance to fully understand the role of the various processes at play during morphogenesis.

The mechanical properties of tissues and their architecture depend on the properties of the individual cells but also on the adhesion energy between the cells and with the extracellular matrix. As a matter of fact, in the absence of interactions with the extracellular matrix, the level of cell-cell adhesion is directly related to the surface tension of cellular aggregates. As a result it was shown that the level of intercellular adhesion controls the shape and hierarchical organization of cells in aggregates *in vitro*[10,14–17]. These processes were described in the framework of the differential adhesion hypothesis[18], in which the cohesive cell aggregates are considered as fluids that tend to minimize their interface as a function of the relative strength of cellular adhesion. It was also shown that cell aggregates exhibit mechanical behaviors that depend on the adhesion between cells. For instance, adhesive cell aggregates spread on solid substrates like viscoelastic droplets at short times, but display distinct long time wetting properties when the adhesion is impaired[19]. In epithelial monolayers, the correlated rearrangements and cell deformations also indicate that the tissue behaves as a viscoelastic liquid[20]. Those experimental observations, together with theoretical frameworks[21], suggest that soft tissues can be described within a soft matter framework[22].

Following this idea, interfacial energy models derived from soap foams were shown to efficiently predict the highly organized cellular structure in organs such as the Drosophila eye[23]. The behavior of foams, in analogy with tissues, have thus been widely studied under various mechanical constraints. These studies revealed the importance of plastic rearrangements for yielding in those materials[24]. Other approaches consist in treating the tissues as fluid-like materials, leading to the modeling of morphogenetic movements based on hydrodynamic theories[25,26]. Similarly, descriptions borrowed from glassy materials have been recently implemented to describe the collective behavior of cells in developing tissues[27]. In this context, the jamming of cells, evidenced by a decrease of fluctuations in the topology of the tissue, directly tunes the material properties of tissues. In turn, it is believed that the jamming transition controls the tissue response to

[a] Sorbonne Université, CNRS, Institut de Biologie Paris-Seine (IBPS), Laboratoire Jean Perrin (LJP), F-75005, Paris, France. E-mail: lea-laetitia.pontani@sorbonne-universite.fr
[b] Department of Mathematics, Imperial College London, South Kensington Campus, London SW7 2AZ, England, UK.

† Electronic Supplementary Information (ESI) available: [details of any supplementary information available should be included here]. See DOI: 00.0000/00000000.

‡ These authors contributed equally to this work.

View Article Online
DOI: 10.1039/D1SM00097G

the large stresses during morphogenesis. Another approach aims to infer the fate of tissues from their static topologies. In this case, the shape of the cells and their packing topology were used to predict the fluidization of tissues[28–33].

Here, we propose to bridge the gap between biological systems and soft matter frameworks by using biomimetic emulsions to decipher the collective dynamics and material properties of tissues during remodeling. In particular, we address the impact of cell-cell adhesion on the mechanical properties of tissues by using functionalized adhesive emulsions. In our previous work, we showed that weakly attractive droplets displayed impaired plastic rearrangements under flow[34]. Here, we propose to directly mimic intercellular adhesion by introducing specific interactions between the droplets[35–37]. Such biomimetic systems have already been shown to reproduce the minimal adhesive and mechanical properties of tissues in static experiments[35]. Their specific interactions are here introduced through biotin-streptavidin-biotin bonds that are allowed to form between the surfaces of contacting droplets. The energy of those binders is comparable to the one of cadherin homophilic interactions in tissues[38]. Moreover, the fluidity of the droplets surface allows the binders to diffuse on the droplets surface and to aggregate into adhesion patches at each droplet-droplet contact. At equilibrium, the size of the patch can be roughly determined by the balance between the gain in adhesion energy and the loss in elastic energy due to the flattening of the droplet surface in the patch[35].

We study the response of these systems under mechanical stress. In order to impose a mechanical perturbation on the assembly of adhered droplets, we push them through a 2D microfluidic constriction (see Fig. 1A). We use a pressure-driven flow that mimics pressure build-up in growing tissues, as well as forces exerted by neighboring cells and tissues during development. This geometry thus forces rearrangements in the emulsions, allowing us to study their elasto-plastic response, but also aims to mimic the convergent extension of epithelial tissues that is essential during embryogenesis[39]. We find that adhesion does not affect the rearrangements topology and that the size of avalanches exhibit the same statistics for all experimental conditions. This observation is further confirmed in simulations that allow us to explore different droplet size polydispersities, deformabilities and adhesion energies. These simulations similarly evidence avalanche size statistics to be independent of adhesion. However, when exploring experimentally the individual T1 events, we find that the local dynamics are slowed down in adhesive emulsions as the binding patches prevent droplet-droplet separation during rearrangements. In turn, we observe that adhesive patches lead to large scale deformations across all droplets in the constriction. In addition to being more deformed, we find that the droplets are also more aligned with each other, which could be the signature of an adhesion-induced polarization process in elongating tissues.

2 Materials and Methods

2.1 Emulsion preparation

Oil in water emulsions were prepared using a pressure emulsifier, as described in[34]. After emulsification, the oil droplets were stabilized with phospholipids in order to make adhesive biomimetic emulsions, as shown in Fig.1B. Firstly, 9 mg of egg L-α-phosphatidylcholine (EPC) lipids and 1mg of DSPE-PEG(2000) biotinylated lipids (Avanti Polar Lipids) were dried under nitrogen and dissolved in 500 μL of dimethyl sulfoxide (DMSO, from Sigma Aldrich). This mixture was then added to 5 mL of high SDS aqueous buffer (5mM SDS, 10mM Tris, pH=7.5). The resulting solution was sonicated for 30 minutes. We then added 2mL of emulsion cream to the phospholipid containing buffer and left to incubate overnight at 4 °C. After incubation the emulsion was washed with 100 mL of high SDS buffer (5mM SDS, 10mM Tris) in a separating funnel and set for a second round of stabilization. During this second round, the SDS concentration in the aqueous phase is lowered in order to favor the repartition of lipids at the droplets surface, instead of SDS, while still keeping them from coalescing. The low SDS aqueous solution used for this last round therefore contains 1mM (instead of 5mM) SDS while the rest of the procedure for lipid dissolution remains unchanged. After this last incubation, the emulsion is washed again in 100 mL of low SDS buffer (1mM SDS, 10mM Tris) in a separating funnel. The resulting droplets display an average diameter of 35 μm (with a size polydispersity of 21%) and are stable over several weeks at 4 °C.

Before running the experiments, the droplets are functionalized with streptavidin Alexa Fluor 555-conjugated (Invitrogen). To this end, 200 μL of the emulsion cream is mixed with 3.6 μL of streptavidin (1 mg/mL) and 200 μL of low SDS buffer. The resulting solution was incubated for 1 hour at room temperature to allow the streptavidin to bind to the biotinylated lipids on the surface of the droplets. The emulsion was then washed twice in the 800 μL of low SDS buffer and once with 1 mL of a water/glycerol mixture (60:40 v:v) containing 1mM SDS, 10mM Tris, 10mM NaCl and 0.05 mg/mL casein to prevent non specific interactions between the droplets and the channel walls (β-casein from bovine milk, Sigma Aldrich). The water/glycerol mixture ensures that the optical index of the continuous phase matches better the one of the oil droplets for transparency, while salt favors adhesion by dampening electrostatic repulsion between the droplets[35].

2.2 Experimental set-up

The microfluidic channels are engineered following the techniques described in[34]. The channel consists of three sections: at the inlet the channel is first 1 mm wide over 5 mm length, then the width is reduced from 1 mm to 38 μm over a length of 5 mm, and then the channel remains 38 μm wide over 5 mm before the outlet (see Fig.1A). In order to maintain the droplets in a monolayer, the depth of the setup is adjusted to 30 μm, thus facilitating image analysis. The mean velocity profile in such channels was measured using tracer particles and follows the expected trend fixed by the channel geometry (see SI†).

After passivating the channel with a solution of 0.25 mg/mL casein for 40 minutes, the emulsion is flowed through the channel using a pressure pump (MFCS-8C Fluigent). After the droplets fill the channel, the pressure is decreased to stop the emulsion flow (P = 5 mbar) and the droplets are left overnight to allow the

View Article Online
DOI: 10.1039/D1SM00097G

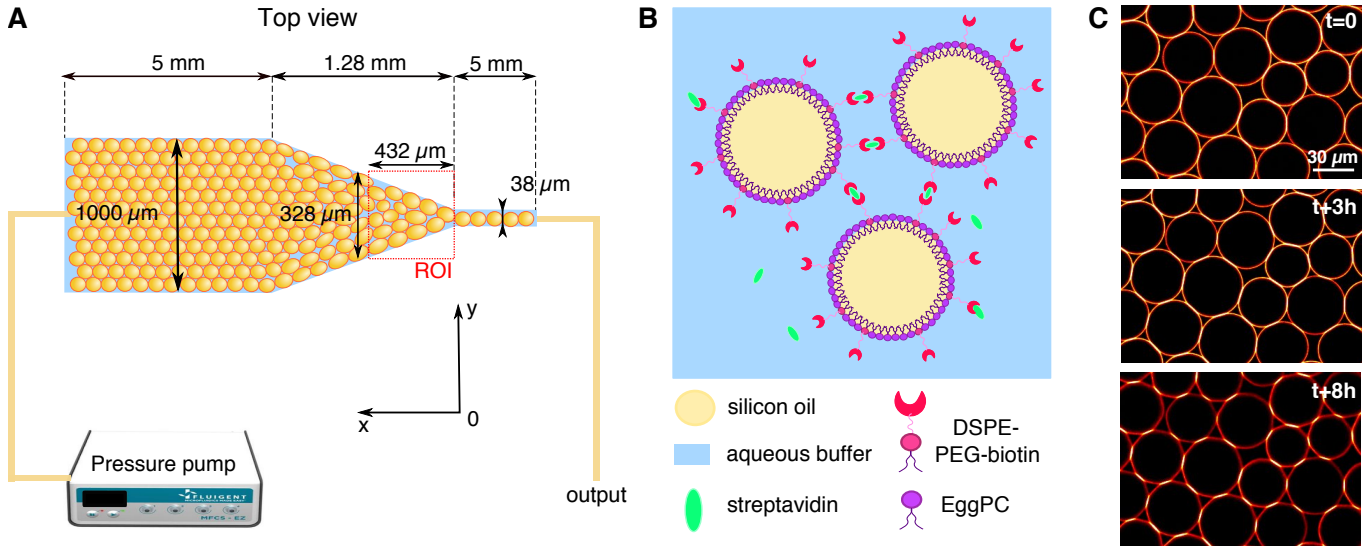

Fig. 1 Experimental setup — (A) The oil in water emulsion is pushed using a pressure pump (P = 15-60 mbar depending on adhesion) through the microfluidic channel that consists of three parts: a 1000 μm wide channel, a constriction, and 38 μm wide channel. The depth of the channel is 30 μm over the whole length, and the diameter of the droplets is ≈ 35 μm. We film the emulsion flow in the area of the constriction situated right before the beginning of the thin channel (see red dashed square for region of interest). (B) Schematic representation of biotin-streptavidin-biotin bonds forming between the contacting surfaces of the droplets stabilized with phospholipids. (C) Progressive formation of adhesive patches over time. The top confocal image shows that Alexa-555 streptavidin fluorescence is more homogeneously distributed over the surface of the droplets at the beginning of the experiment. Over time, biotin-streptavidin-biotin bonds form at the droplet-droplet contacts (middle image) until they enrich into clear adhesive patches with an increased fluorescence signal, allowing to isolate them through image analysis. Note that the formation of the patches depletes the fluorescence level on the free edge of the droplets making it appear more red over time.

droplets to pack and the adhesion patches to grow (see Fig.1C). The global packing fractions resulting from this process range from 83 to 91% for adhesive emulsions, and from 82 to 92% for non-adhesive ones. After the incubation phase, the emulsion is flowed in the channel under constant pressure (P = 15-60 mbar depending on adhesion). Once the flow is established, the average droplet velocity is stable during an experiment, except for sudden bursts that are due to rearrangements releasing stress in the emulsion (data not shown). The velocities measured at the center of the constriction, 200 μm away from the beginning of the thin channel, are 23 ± 12 $\mu m/s$ for adhesive emulsions and 32 ± 12 $\mu m/s$ for non-adhesive ones. The emulsion is imaged in the constriction area through confocal microscopy with a 20x objective (exposure time = 20 ms, frame rate = 15 fps, see Fig.2A).

2.3 Numerical Simulations

In order to explore a wide range of parameters, we develop a computational toy model for adhesive emulsions that is based on the deformable particle model (DPM) recently introduced by Boromand et al.[40,41]. In static 2D emulsions, particles deform in response to mechanical stresses to minimize their perimeter while keeping their area fixed. Modeling each of the N emulsion droplets as a deformable polygon with N_v circulo-line edges with width δ, our model relies on the minimization of the following potential energy:

$$U_{DP} = \gamma \sum_{m=1}^{N} \sum_{i=1}^{N_v} l_{m,i} + \frac{k}{2} \sum_{m=1}^{N} (a_m - a_{m0})^2 + U_{\text{int}} \qquad (1)$$

where $l_{m,i}$ is the length of the circulo-line between vertices i and $i+1$ and a_m is the area of droplet m. The first term in U_{DP} is proportional to the perimeter of the droplet with a proportionality constant equal to a line tension γ. The second term is a penalization term quadratic in the distance between the area of the droplet and a target area a_{m0} with compressibility coefficient k.

Finally, U_{int} represents the interaction potential energy between two droplets; it is composed of a repulsive term and an attractive term (see details in SI†). Upon contact, overlaps between interacting droplets are penalized by introducing a purely repulsive interaction potential U_r between all pairs of circulo-lines of different droplets. Upon contact, two droplets are also subjected to contact mediated adhesion. For instance, after the initial contact between a vertex of droplet i and a vertex or an edge of droplet j is made, droplets i and j are subject to an attractive force derived from the interaction potential U_a[42]. See supplementary information† for the detailed expressions of the repulsive and attractive energy terms.

Under flow conditions, we use the same constriction angle as in the experiments (see movie†). We flow the emulsion through the constriction by subjecting each particle vertex to a constant force in the direction of the channel. We use periodic boundary conditions along the axis of the microfluidic channel, i.e. that droplets exiting the constriction re-enter the channel ahead of the constriction. Provided these forces, we integrate the equations of motion for the vertices in the overdamped limit.

We perform simulations with $N = 128$ deformable droplets with $N_v = 16$ vertices per droplet. We vary the line tension γ and the adhesion strength k_a keeping all other parameters fixed for

View Article Online
DOI: 10.1039/D1SM00097G

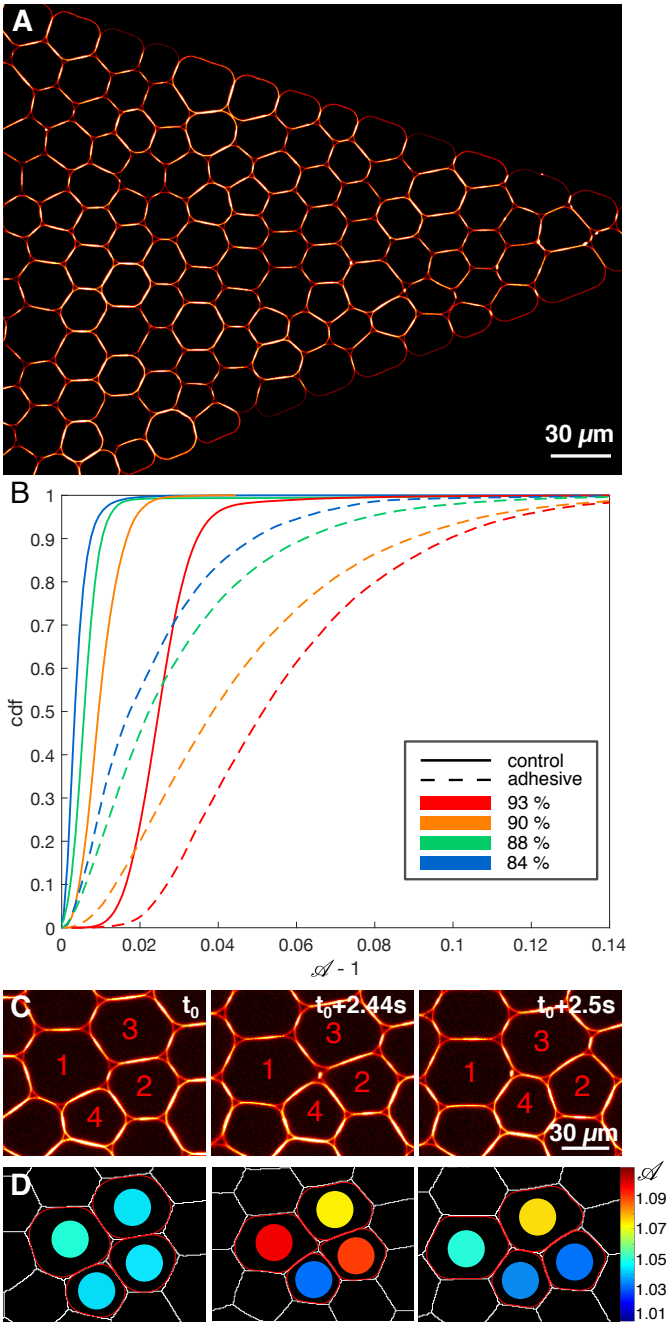

Fig. 2 Confocal imaging and analysis — (A) Confocal image of an adhesive emulsion in the constriction. (B) Cumulative distributions of deformation $\mathscr{A}$ - 1 for all droplets in the region of interest for adhesive (dashed lines) and non-adhesive control (solid lines) emulsions across packing fractions ranging from $\phi_l = 84$ to 93%. (C) Confocal images of four adhesive droplets undergoing a T1 event. Droplets 1 and 2 are first connected through an adhesive patch (left panel), are then pulled apart (middle panel) and are not neighbors anymore (right panel). In the meantime droplets 3 and 4 gain a contact at the end of the event. (D) Result of the image analysis performed on (C). Voronoi cells are drawn in white lines, droplet contours are shown in red and the color of the disc inside each droplet codes for its deformation $\mathscr{A}$.

monodisperse emulsions and polydisperse emulsions with 20% polydispersity (see in SI†). We place ourselves in the limit of non-overlapping, nearly incompressible emulsion droplets.

2.4 Data Analysis

2.4.1 Tesselation and tracking

Raw images are segmented using Ilastik[43]. The segmented images are then skeletonized and droplets are detected using Fiji. Droplets, as well as channel boundaries, are then indexed directly on the segmented image. A surface Voronoi tessellation is finally performed on these processed images to identify the Voronoi cells corresponding to each droplet.

A table of neighboring relationships between droplets and Voronoi cells is generated using the Region Adjacency Graphs from the Python Scikit-image package[44]. We then obtain the list of neighbors at each time for each droplet in the constriction and measure the size of droplet-droplet contacts as well as the length of the edge between neighboring Voronoi cells. The droplets are tracked with a custom Python tracking algorithm allowing us to compute instant velocities of droplets and Voronoi cells.

2.4.2 Deformation

We measure droplet deformations following the method used in[34]. To avoid artificial measurement noise due to finite image resolution, we fit successions of osculating arcs of circles around the droplet contours. The computed shape parameter $\mathscr{A} = p^2/4\pi a$, with p the perimeter and a the surface of the identified droplet, and local packing fraction ϕ_l are then calculated from this fitted contour, as shown in Fig.2D. Note that we exclude the droplets whose corresponding Voronoi cells touch the walls of the channel. In parallel, we also fit each droplet with an ellipse, and use its aspect ratio and orientation of the major axis to study elongation and alignment of the droplets in the constriction. Further details of the image analysis can be found in SI †.

2.4.3 T1 events detection

By tracking droplets and their neighborhood over time, we identify the formation or rupture of droplet-droplet contacts and edges between Voronoi cells. This allows us to identify individual T1 events by considering the neighborhood of droplet quadruplets as shown in Fig.2C. A typical T1 event involves 4 droplets that undergo the following sequence: droplets 1 and 2 are initially in contact, while droplets 3 and 4 are not touching and are distributed on each side of this contact; then droplets 1 and 2 are separated, allowing droplets 3 and 4 to come into contact. As seen in Fig.2C this particular type of rearrangement can be the basis of tissue elongation along the axis of the newly formed contact between cells 3 and 4. We then examine avalanche phenomena by considering T1 events that occur during a given time window and that are connected by neighboring droplets.

To do so we define an adimensional time $t = t^*\langle V\rangle/\langle R\rangle$ with t^* the elapsed time in seconds, $\langle V\rangle$ the mean flow velocity and $\langle R\rangle$ the mean radius of droplets that are both averaged over all droplets in all frames of each movie. T1 events whose cells were neighbors to each other within a specified time window (here, 0.4 in adimensional time) are grouped in a common avalanche event

View Article Online
DOI: 10.1039/D1SM00097G

(see SI and supplementary movie†). For simulation data, the T1 were similarly identified from the loss and gain of physical contact between quadruplets of droplets, and grouped in avalanches using the same adimensional time window. We quantify avalanche sizes by measuring the total number of droplets participating in the same avalanche.

During a rearrangement, we also measure the speed at which contacts between voronoi cells are shrinking before the actual neighbor exchange. To do so, we measure $\frac{\Delta l_e}{\Delta t}/\langle V \rangle$, where l_e is the contact length between neighboring Voronoi cells (see supplementary movie†), $\Delta l_e = l_e(\text{frame } n) - l_e(\text{frame } n+1)$ and Δt the time between two consecutive frames. We measure it for all the droplets involved in a T1 event during the adimensional time window $[t_0 - 10, t_0]$, t_0 being the exact moment of neighbor exchange.

3 Results

We inject and flow emulsions in a microfluidic constriction as depicted in Fig.1A (see also supplementary movie †). In the large channel the emulsion spans about 30 droplet diameters, and it progressively reduces to one droplet in the thin channel. We experimentally tested both non-adhesive and adhesive emulsions (see Materials and Methods). When the droplets are adhesive one expects their flow to be hindered and the emulsion to behave more elastically, whereas an assembly of repulsive droplets, for which rearrangements can be performed at lower energetic cost, should be more plastic. Indeed, when measuring the shape parameter $\mathscr{A}$ of all droplets in the constriction, we find that they are globally more deformed in the case of adhesive emulsions for all packing fractions (see Fig.2B), which is consistent with previous work[34].

In agreement with this global observation, much higher pressures need to be applied for adhesive emulsions to flow in the constriction compared to non-adhesive ones. On average, in our experimental conditions, one needs to apply about 15-20 mbar with the pressure controller for repulsive droplets, as opposed to 30 to 60 mbar for adhesive ones. At the macroscopic scale these two systems therefore exhibit very distinct material properties. We explore in what follows the microscopic origin of this difference in behavior.

3.1 Topology and local dynamics of rearrangements

We first study the properties of these two different kinds of emulsions by examining the topology of droplet rearrangements such as T1 events depicted in Fig.2C-D. Indeed, it was previously shown that the rearrangements of monodisperse droplets are correlated and ordered in space and time when going through a constriction[34,45]. In particular, T1 events are aligned along disclination planes that are regularly spaced. Here, we do not expect to see such patterns emerge in the constriction, even in the absence of adhesion, as our droplets exhibit a 21% size polydispersity. Instead, our experiments display a spatially heterogeneous and intermittent flow which is commonly observed in nature during avalanching. Indeed, a large variety of physical systems[46–56] generically exhibit intermittent dynamics which is characterized by a slow build-up and a rapid release of stress in the system when

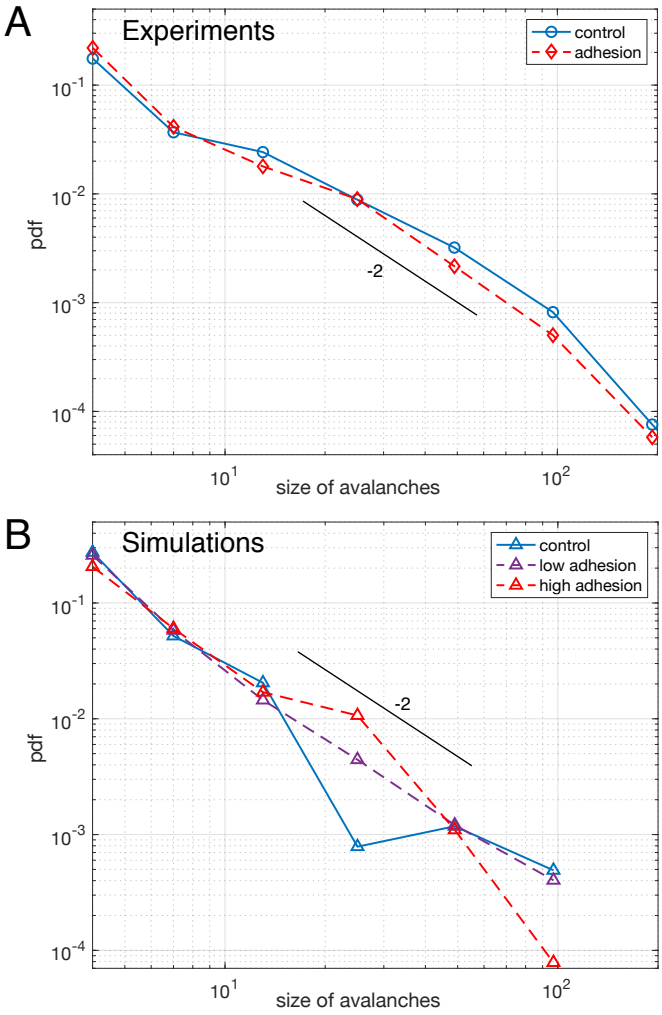

Fig. 3 Avalanche statistics for experimental data (A) and numerical simulations (B) - (A) Distributions of avalanche size for adhesive (red dashed line) and non-adhesive (blue solid line) emulsions cannot be distinguished. (B) Distributions of avalanche size for polydisperse packings of highly deformable droplets (lowest γ) without adhesion (blue solid line), with low adhesion (purple dashed line) and high adhesion (red dashed line), see SI†for values of k_a and γ. All curves are averaged over 5 repeats of simulations performed with the same parameters. The distributions are not significantly different between each other. The logarithmic binning as powers of two is used for the x-axis in both panels. The maximum cluster size that we measure corresponds to an avalanche over the entire field of view, indicating that the choice of time window does not artificially exclude large avalanches from the analysis. In both panels a line corresponding to a power law with exponent -2 was drawn as a guide to the eye.

View Article Online
DOI: 10.1039/D1SM00097G

subjected to a slow continuous loading. Few studies have looked at this intermittent dynamics at the local scale[46,57–60]. Here, having access to the whole dynamics during the emulsion flow, we examine the statistics of avalanche sizes through a measure of the local plastic rearrangements.

More specifically, we measure the size of the avalanches for different adhesion conditions. We define the avalanche size as the number of droplets participating in spatially and temporally connected rearrangements during a given time window. In particular, T1 events whose cells are neighbors at any point within the time window are grouped in the same avalanche. Under all experimental conditions, the avalanches sizes are distributed according to power-law distributions and are surprisingly indistinguishable with or without adhesion, as shown in Fig.3A. Although one would expect adhesion to give rise to longer range effects, large avalanches do not seem to prevail in adhesive emulsions. Moreover, in both conditions the distribution of avalanche sizes reasonably follows a power law with a -2 exponent, in agreement with previous results obtained for 2D granular packings[60].

To confirm this observation, we performed numerical simulations (see Materials and Methods), allowing us to systematically vary the adhesion energy, droplet deformability and polydispersity. We first examined packings with the same polydispersity as in our biomimetic emulsions. We find that adhesion does not affect significantly the distribution of avalanche sizes as shown in Fig.3B, which confirms our experimental findings. However, in the lowest deformability condition, a difference between monodisperse and polydisperse packings clearly exists (see SI†). Indeed, our results show that monodisperse packings exhibit an excess of large avalanches for all adhesion energies. This result is consistent with the idea that low deformability monodisperse particles exhibit a higher crystalline order leading to large rearrangements taking place along disclination planes[45,61].

While we could not find evidence of the effect of adhesion on the statistics of avalanches sizes, the consequences of adhesion can be evidenced locally by examining the dynamics of individual rearrangements. To do so, we have first measured the speed at which the length of the dislocating edge decreases during a T1 event. We find that the edge length shrinks more slowly for adhesive droplets for all edge lengths, as shown in Fig.4A. Here, the presence of adhesion helps stabilize short edges and slows down the dislocation process by adding a strong energetic barrier to the formation of the rosette preceding the actual neighbor exchange[62]. However, once the contacting droplets have been separated, the growth of a new edge takes place faster for adhesive droplets (data not shown). This is due to the additional accumulated pressure necessary to break the adhesive contact, which pushes the new droplets in contact more promptly.

In conclusion, avalanche size statistics in flowing emulsions is not affected by adhesion. In fact, the signature of adhesion only lies in the local dynamics of T1 events rather than in long range collective effects. We next study the impact of these local dynamics on droplet deformations.

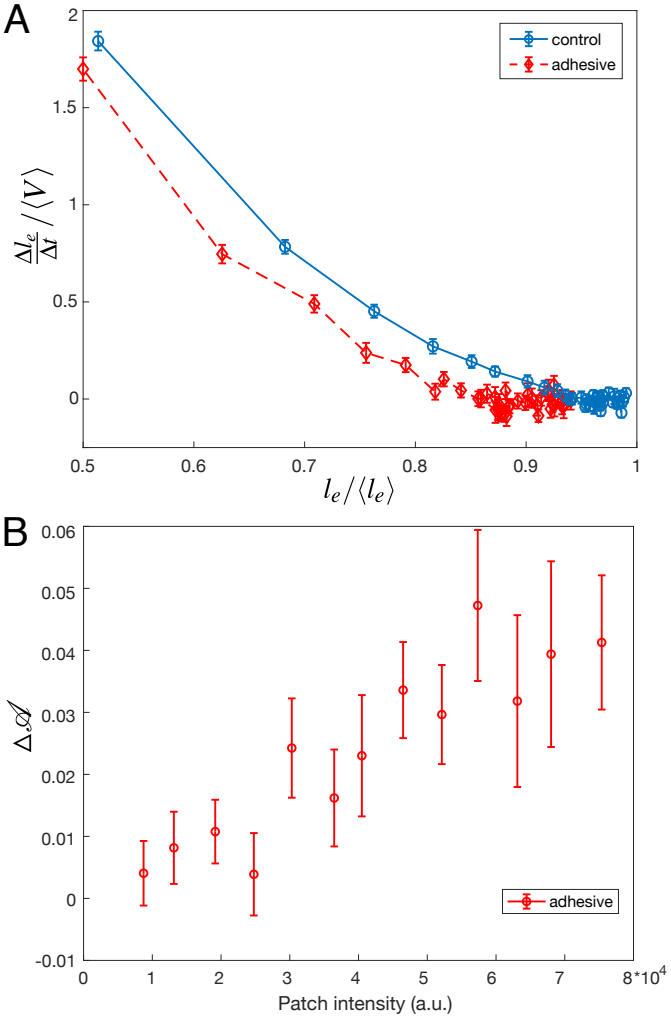

Fig. 4 Properties of individual rearrangements - (A) Rate of change of shrinking for dislocating edges of length l_e normalized by the average velocity of the flow $\langle V\rangle$ plotted as a function of l_e normalized by the global average edges length $\langle l_e\rangle$. For a given l_e, a dislocating edge length is always disappearing more slowly for adhesive emulsions. (B) Difference in droplet deformation $\Delta\mathscr{A}$ before and after they undergo a T1 event as a function of adhesive patch intensity. An increase of patch intensity, i.e. an increase in binding energy, corresponds to higher values of droplet deformation accumulated before a T1 event.

View Article Online
DOI: 10.1039/D1SM00097G

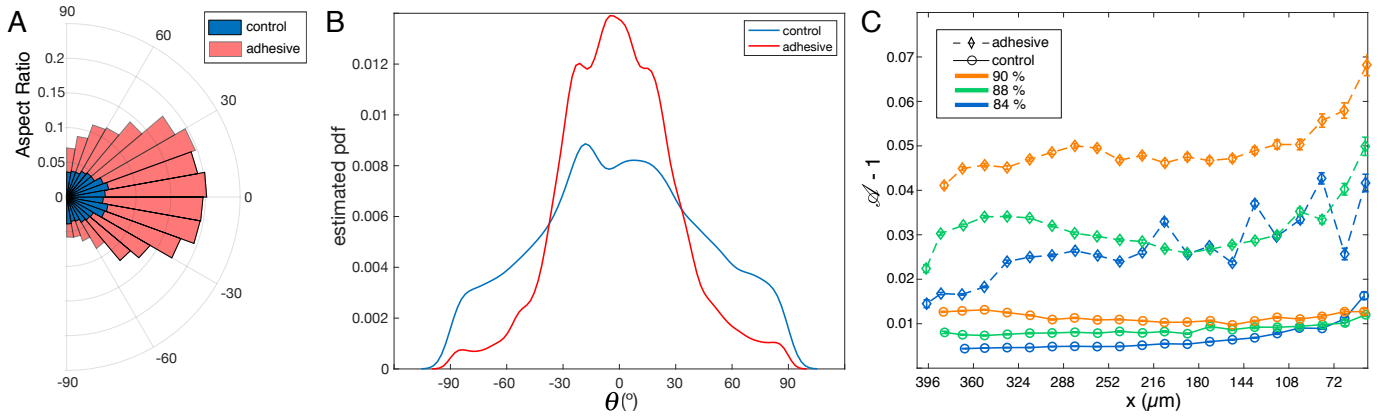

Fig. 5 Analysis of droplet deformation — (A) and (B) Analysis of the ellipses fitted to control (blue) and adhesive (pink) droplets in packings with average $\phi_l = 88\%$. (A) Mean aspect ratios as a function of ellipse orientation. The aspect ratios for adhesive droplets are significantly larger for all considered angles. (B) Distributions of ellipse orientations θ with respect to the x axis in the constriction. Adhesive emulsions yield a narrower distribution than control ones. (C) Average deformation $\mathscr{A}$-1 of the droplets along the x axis of the channel for the adhesive (diamonds) and control (circles) emulsions at various packing fractions. The deformation is averaged in 35 μm bins along the x axis, x=0 corresponding to the entry of the thin channel. The error bars correspond to the standard error of mean for the distribution of $\mathscr{A}$ obtained in each bin.

3.2 Droplet deformations

As a consequence of impaired rearrangements, the droplets should be more deformed during T1 events in adhesive emulsions. Indeed, the adhesion patches induce pulling forces on the droplets in addition to the compressive forces induced by the constriction geometry. To relate the locally slowed down rearrangements to increased deformations, we have examined the deformation of droplets involved in T1 events by measuring their shape parameter $\mathscr{A} = p^2/4\pi a$ over the course of the rearrangement. In particular, we quantify the difference between the level of deformation before and after a T1 by measuring $\Delta\mathscr{A} = \frac{\mathscr{A}_1^{t^-} + \mathscr{A}_2^{t^-}}{2} - \frac{\mathscr{A}_3^{t^+} + \mathscr{A}_4^{t^+}}{2}$, where $\mathscr{A}_1, \mathscr{A}_2$ are droplets that were in contact before a T1 event, and $\mathscr{A}_3, \mathscr{A}_4$ are droplets that became in contact after the T1 event, and t^- and t^+ are the frames just before and after the rearrangement, respectively. For non-adhesive emulsions, we find that the distribution of $\Delta\mathscr{A}$ is symmetric around zero, indicating that droplet deformations are identical before and after the rearrangements (see SI†). In contrast, we find that this distribution becomes asymmetric when droplets interact through specific binders. However, after detachment, the droplets do not exhibit any excess in deformation and thus behave like repulsive droplets. This makes sense because in our system adhesion is short range and dense adhesive patches form on the timescale of hours.

Considering this scenario, we finally relate the amount of excess deformation $\Delta\mathscr{A}$ during rearrangements to the binding energy between droplets. To do so, we plot $\Delta\mathscr{A}$ as a function of the streptavidin fluorescence intensity at the dislocating contact area and find that a higher intensity, meaning a higher binding energy, directly correlates with droplets that are more deformed prior to rearrangements (Fig.4B). This directly links deformation levels in the emulsion to binding energy between droplets.

To track the global effect of this local excess of deformation during rearrangements, we have fitted ellipses to all droplets in the field of view and measured the aspect ratio of the ellipses as well as the orientation of their major axis with respect to the horizontal x axis defined in Fig.1A. As shown in the polar plot in Fig.5A, the aspect ratio of the droplets is significantly higher for adhesive emulsions for the whole range of orientations. Moreover, the distribution of ellipse orientations is more peaked in the case of adhesive emulsions (Fig.5B).

In order to quantify droplets deformation independently of their orientation, we measure the shape parameter $\mathscr{A}$ for all droplets in all experiments. When plotted along the x axis, we observe that the shape parameter of adhesive droplets is much higher for all considered packing fractions (see Fig. 5C). In addition, this high deformation does not relax back to the values measured for non adhesive emulsions even far from the outlet (i.e. $\approx$10 droplet diameters away from the entry of the small channel). This indicates that the effects of adhesion on droplet deformations are long-ranged, which suggests that forces are transmitted more efficiently through the emulsion in the presence of adhesive patches.

4 Conclusion

Intuitively, cell-cell adhesion is expected to rigidify biological tissues, providing them with an elastic response to an applied force. In cellular aggregates, the level of cadherin expression has indeed been shown to control the wetting properties on 2D surfaces[19], while in developing tissues loss of cadherin function can induce a lowering of the yield stress[27]. This effect of adhesion on the bulk material properties of tissues is also observed indirectly in our biomimetic emulsions. Indeed, a much higher pressure is needed to induce flow in the case of adhesive emulsions. However, passed that threshold force, both repulsive and adhesive emulsions can flow and go through a constriction. We observed that the flow of emulsions under continuous load exhibits a spatially and temporally heterogeneous dynamics that are characteristic of yield-stress materials. Furthermore, our experiments and simulations both show that the avalanche size statistics is independent of adhesion but weakly dependent on the presence of crystalline order

View Article Online
DOI: 10.1039/D1SM00097G

in the spatial structure of the emulsions.

However, the way those rearrangements take place differs with or without adhesion. Indeed, adhesion prevents the detachment of bound droplets, leading to slowed down dynamics prior to the first droplet-droplet contact loss in T1 events. As a result, droplets exhibit larger deformations and they tend to align with the direction of tissue elongation. These long-range cell elongations could be the onset of symmetry breaking in tissues, thus inducing signaling pathways during morphogenesis. Indeed, tissue shape changes can be due to a combination of external forces as well as intrinsic forces. This is the case for the process of convergent extension that is very conserved across metazoans[39]. These intrinsic forces usually emerge from an anisotropy of contractility in individual cells[63] and recent studies highlighted the importance of in-plane anisotropy[64,65]. In this case, the cytoskeleton is remodeled and acto-myosin contractility can be increased at cell-cell junctions that are perpendicular to the extension axis[66,67]. Interestingly, a recent study also evidenced the importance of cell alignment to predict the fate of tissues and highlighted its impact for rapid morphogenetic movements such as the convergent extension of the drosophila germband[68].

In this context, our results suggest that adhesion could participate to morphogenetic processes by inherently making the cells anisotropic when tissues start to be elongated, thus providing a positive feedback loop between external forces and the intracellular response. Beyond these findings, our biomimetic approach paves the path to unraveling other biological mechanisms in the future, such as the role of the extracellular matrix or that of differential adhesion during morphogenetic processes.

Conflicts of interest

There are no conflicts to declare.

Acknowledgements

The authors thank Gladys Massiera and Laura Casanellas for fruitful discussions, as well as Jacques Fattaccioli for letting us use his pressure emulsifier. L.-L. Pontani also acknowledges financial support from Agence Nationale de la Recherche (BOAT, ANR-17-CE30-0001) as well as financial support from Emergence(s) Ville de Paris.

Notes and references

1 E. Kutejova, J. Briscoe and A. Kicheva, Current Opinion in Genetics & Development, 2009, **19**, 315–322.
2 H. Meinhardt, Cold Spring Harbor Perspectives in Biology, 2009, **1**, year.
3 O. Wartlick, A. Kicheva and M. González-Gaitán, Cold Spring Harbor Perspectives in Biology, 2009, **1**, year.
4 T. Mammoto, A. Mammoto and D. E. Ingber, Annual review of cell and developmental biology, 2013, **29**, 27–61.
5 C.-P. Heisenberg and Y. Bellaïche, Cell, 2013, **153**, 948–62.
6 R. Keller, Science, 2012, **338**, 201–203.
7 R. A. Foty and M. S. Steinberg, WIREs Developmental Biology, 2013, **2**, 631–645.
8 V. Barone and C.-P. Heisenberg, Current Opinion in Cell Biology, 2012, **24**, 148–153.
9 F. m. c. Graner and J. A. Glazier, Phys. Rev. Lett., 1992, **69**, 2013–2016.
10 M. Krieg, Y. Arboleda-Estudillo, P. H. Puech, J. Käfer, F. Graner, D. J. Müller and C. P. Heisenberg, Nature Cell Biology, 2008, **10**, 429–436.
11 G. B. Blanchard, A. J. Kabla, N. L. Schultz, L. C. Butler, B. Sanson, N. Gorfinkiel, L. Mahadevan and R. J. Adams, Nature Methods, 2009, **6**, 458–464.
12 H. Zhang and M. Labouesse, Journal of Cell Science, 2012, **125**, 4172–4172.
13 E. Farge and M. Labouesse, in Mechanotransduction in Development, Academic Press, 2011, vol. 95, ch. 8, pp. 243–265.
14 E. Schötz, R. D. Burdine, F. Jülicher, M. S. Steinberg, C. Heisenberg and R. A. Foty, HFSP Journal, 2008, **2**, 42–56.
15 R. Foty, C. Pfleger, G. Forgacs and M. Steinberg, Development, 1996, **122**, 1611–1620.
16 M. S. Steinberg and M. Takeichi, Proceedings of the National Academy of Sciences, 1994, **91**, 206–209.
17 S. F. G. Krens, C.-P. Heisenberg and M. Labouesse, in Cell Sorting in Development, Academic Press, 2011, vol. 95, ch. 6, pp. 189–213.
18 M. S. Steinberg, Journal of Experimental Zoology, 1970, **173**, 395–433.
19 S. Douezan, K. Guevorkian, R. Naouar, S. Dufour, D. Cuvelier and F. Brochard-Wyart, Proceedings of the National Academy of Sciences, 2011, **108**, 7315–7320.
20 S. Tlili, M. Durande, C. Gay, B. Ladoux, F. Graner and H. Delanoë-Ayari, Phys. Rev. Lett., 2020, **125**, 088102.
21 M. L. Manning, R. A. Foty, M. S. Steinberg and E.-M. Schoetz, Proceedings of the National Academy of Sciences, 2010, **107**, 12517–12522.
22 D. Gonzalez-Rodriguez, K. Guevorkian, S. Douezan and F. Brochard-Wyart, Science, 2012, **338**, 910–917.
23 S. Hilgenfeldt, S. Erisken and R. W. Carthew, Proceedings of the National Academy of Sciences, 2008, **105**, 907–911.
24 I. Cantat, S. Cohen-Addad, F. Elias, F. Graner, R. Höhler, O. Pitois, F. Rouyer, A. Saint-Jalmes, R. Flatman and S. Cox, Foams : Structure and Dynamics., Oxford University Press, Incorporated, 2013, p. 288.
25 M. Dicko, P. Saramito, G. B. Blanchard, C. M. Lye, B. Sanson and J. Étienne, PLOS Computational Biology, 2017, **13**, e1005443–.
26 S. J. Streichan, M. F. Lefebvre, N. Noll, E. F. Wieschaus and B. I. Shraiman, eLife, 2018, **7**, year.
27 A. Mongera, P. Rowghanian, H. Gustafson, E. Shelton, D. Kealhofer, E. Carn, F. Serwane, A. Lucio, J. Giammona and O. Camp'as, Nature, 2018, **561**, 401–405.
28 D. Bi, J. H. Lopez, J. M. Schwarz and M. Lisa Manning, Soft Matter, 2014, **10**, 1885–1890.
29 D. Bi, J. H. Lopez, J. M. Schwarz and M. L. Manning, Nature Physics, 2015, **11**, 1074–1079.

View Article Online
DOI: 10.1039/D1SM00097G

30 D. Bi, X. Yang, M. C. Marchetti and M. L. Manning, Phys. Rev. X, 2016, **6**, 021011.
31 M. Merkel and M. L. Manning, New Journal of Physics, 2018, **20**, 022002.
32 M. Merkel, K. Baumgarten, B. P. Tighe and M. L. Manning, Proceedings of the National Academy of Sciences, 2019, **116**, 6560–6568.
33 L. Yan and D. Bi, Physical Review X, 2019, **9**, 011029.
34 I. Golovkova, L. Montel, E. Wandersman, T. Bertrand, A. M. Prevost and L. L. Pontani, Soft Matter, 2020, **16**, 3294–3302.
35 L. L. Pontani, I. Jorjadze, V. Viasnoff and J. Brujic, Proceedings of the National Academy of Sciences, 2012, **109**, 9839–44.
36 L. Feng, L.-L. Pontani, R. Dreyfus, P. Chaikin and J. Brujic, Soft Matter, 2013, **9**, 9816.
37 L.-L. Pontani, I. Jorjadze and J. Brujic, Biophysical journal, 2016, **110**, 391–9.
38 P. Katsamba, K. Carroll, G. Ahlsen, F. Bahna, J. Vendome, S. Posy, M. Rajebhosale, S. Price, T. M. Jessell, A. Ben-Shaul, L. Shapiro and B. H. Honig, Proceedings of the National Academy of Sciences, 2009, **106**, 11594–11599.
39 A. Sutherland, R. Keller and A. Lesko, Seminars in Cell & Developmental Biology, 2020, **100**, 199–211.
40 A. Boromand, A. Signoriello, F. Ye, C. S. O'Hern and M. D. Shattuck, Phys. Rev. Lett., 2018, **121**, 248003.
41 A. Boromand, A. Signoriello, J. Lowensohn, C. S. Orellana, E. R. Weeks, F. Ye, M. D. Shattuck and C. S. O'Hern, Soft Matter, 2019, –.
42 P. Chaudhuri, L. Berthier and L. Bocquet, Phys. Rev. E, 2012, **85**, 021503.
43 S. Berg, D. Kutra, T. Kroeger, C. N. Straehle, B. X. Kausler, C. Haubold, M. Schiegg, J. Ales, T. Beier, M. Rudy, K. Eren, J. I. Cervantes, B. Xu, F. Beuttenmueller, A. Wolny, C. Zhang, U. Koethe, F. A. Hamprecht and A. Kreshuk, ilastik: interactive machine learning for (bio)image analysis.
44 S. Van der Walt, J. L. Schönberger, J. Nunez-Iglesias, F. Boulogne, J. D. Warner, N. Yager, E. Gouillart and T. Yu, PeerJ, 2014, **2**, e453.
45 Y. Gai, C. M. Leong, W. Cai and S. K. Y. Tang, Proceedings of the National Academy of Sciences, 2016, **113**, 12082–12087.
46 A. Le Bouil, A. Amon, S. McNamara and J. Crassous, Phys. Rev. Lett., 2014, **112**, 246001.
47 F. Dalton and D. Corcoran, Phys. Rev. E, 2001, **63**, 061312.
48 R. R. Hartley and R. P. Behringer, Nature, 2003, **421**, 928–931.
49 A. Baldassarri, F. Dalton, A. Petri, S. Zapperi, G. Pontuale and L. Pietronero, Phys. Rev. Lett., 2006, **96**, 118002.
50 A. Amon, V. B. Nguyen, A. Bruand, J. Crassous and E. Clément, Phys. Rev. Lett., 2012, **108**, 135502.
51 D. V. Denisov, K. A. Lőrincz, W. J. Wright, T. C. Hufnagel, A. Nawano, X. Gu, J. T. Uhl, K. A. Dahmen and P. Schall, Scientific Reports, 2017, **7**, 43376.
52 C. Maloney and A. Lemaître, Phys. Rev. Lett., 2004, **93**, 016001.
53 C. E. Maloney and M. O. Robbins, Phys. Rev. Lett., 2009, **102**, 225502.
54 M. Otsuki and H. Hayakawa, Phys. Rev. E, 2014, **90**, 042202.
55 K. A. Dahmen, Y. Ben-Zion and J. T. Uhl, Nature Physics, 2011, **7**, 554–557.
56 J. Lin, E. Lerner, A. Rosso and M. Wyart, Proceedings of the National Academy of Sciences, 2014, **111**, 14382–14387.
57 D. Howell, R. P. Behringer and C. Veje, Phys. Rev. Lett., 1999, **82**, 5241–5244.
58 A. Kabla, J. Scheibert and G. Debregeas, Journal of Fluid Mechanics, 2007, **587**, 45–72.
59 K. E. Daniels and N. W. Hayman, Journal of Geophysical Research: Solid Earth, 2008, **113**, year.
60 J. Barés, D. Wang, D. Wang, T. Bertrand, C. S. O'Hern and R. P. Behringer, Phys. Rev. E, 2017, **96**, 052902.
61 M. Zaiser, Advances in Physics, 2006, **55**, 185–245.
62 L. Yan and D. Bi, Phys. Rev. X, 2019, **9**, 011029.
63 A. C. Martin, M. Kaschube and E. F. Wieschaus, Nature, 2009, **457**, 495–499.
64 S. Chanet, C. J. Miller, E. D. Vaishnav, B. Ermentrout, L. A. Davidson and A. C. Martin, Nature Communications, 2017, **8**, 15014–.
65 K. Doubrovinski, J. Tchoufag and K. Mandadapu, Development (Cambridge, England), 2018, **145**, year.
66 A. C. Martin, Philosophical transactions of the Royal Society of London. Series B, Biological sciences, 2020, **375**, 20190551.
67 N. C. Heer and A. C. Martin, Development (Cambridge, England), 2017, **144**, 4249—4260.
68 X. Wang, M. Merkel, L. B. Sutter, G. Erdemci-Tandogan, M. L. Manning and K. E. Kasza, Proceedings of the National Academy of Sciences of the United States of America, 2020, **117**, 13541–13551.

Bibliography

[1] J. D. Amack and M. L. Manning. Knowing the boundaries: Extending the differential adhesion hypothesis in embryonic cell sorting. *Science*, 338(6104):212–215, 2012. [Cited on page 18.]

[2] A. Amon, V. B. Nguyen, A. Bruand, J. Crassous, and E. Clément. Hot spots in an athermal system. *Physical Review Letters*, 108(13):1–5, 2012. [Cited on pages 59 and 60.]

[3] S. Anava, A. Greenbaum, E. B. Jacob, Y. Hanein, and A. Ayali. The regulative role of neurite mechanical tension in network development. *Biophysical Journal*, 96(4):1661–1670, 2009. [Cited on page 73.]

[4] A. Argon. Plastic deformation in metallic glasses. *Acta Metallurgica*, 27(1):47–58, 1979. [Cited on page 59.]

[5] S. Asakura and F. Oosawa. Interaction between particles suspended in solutions of macromolecules. *Journal of Polymer Science*, 33(126):183–192, 1958. [Cited on pages 19 and 43.]

[6] S. J. Bachmann, M. Petitzon, and B. M. Mognetti. Bond formation kinetics affects self-assembly directed by ligand-receptor interactions. *Soft Matter*, 12(47):9585–9592, 2016. [Cited on page 21.]

[7] M. Badve and M. Barigou. Local description of foam flow, deformation and pressure drop in narrow constricted channels. *International Journal of Multiphase Flow*, 128:103279, 2020. [Cited on page 19.]

[8] J. Barés, D. Wang, D. Wang, T. Bertrand, C. S. O'Hern, and R. P. Behringer. Local and global avalanches in a two-dimensional sheared granular medium. *Physical Review E*, 96(5), 2017. [Cited on pages 60 and 61.]

[9] R. P. Behringer and B. Chakraborty. The physics of jamming for granular materials: A review. *Reports on Progress in Physics*, 82(1), 2019. [Cited on pages 15 and 16.]

[10] S. Berg, D. Kutra, T. Kroeger, C. N. Straehle, B. X. Kausler, C. Haubold, M. Schiegg, J. Ales, T. Beier, M. Rudy, K. Eren, J. I. Cervantes, B. Xu, F. Beuttenmueller, A. Wolny, C. Zhang, U. Koethe, F. A. Hamprecht, and A. Kreshuk. Ilastik: Interactive Machine Learning for (Bio)Image Analysis. *Nature Methods*, 16(12):1226–1232, 2019. [Cited on page 34.]

[11] C. Bertet, L. Sulak, and T. Lecuit. Myosin-dependent junction remodelling controls planar cell intercalation and axis elongation. *Nature*, 429(6992):667–671, 2004. [Cited on page 18.]

[12] D. Bi, J. H. Lopez, J. M. Schwarz, and M. L. Manning. A density-independent rigidity transition in biological tissues. *Nature Physics*, 11(12):1074–1079, 2015. [Cited on pages 16 and 17.]

[13] D. Bi, X. Yang, M. C. Marchetti, and M. L. Manning. Motility-driven glass and jamming transitions in biological tissues. *Physical Review X*, 6(2):1–13, 2016. [Cited on page 17.]

[14] J. Bibette, F. Leal-Calderon, V. Schmitt, and P. Poulin. *Emulsion Science*, volume 181 of *Springer Tracts in Modern Physics*. Springer Berlin Heidelberg, Berlin, Heidelberg, 2002. [Cited on page 26.]

[15] J. Bibette, D. Roux, and B. Pouligny. Creaming of emulsions: the role of depletion forces induced by surfactant. *Journal de Physique II*, 2(3):401–424, mar 1992. [Cited on page 43.]

[16] T. M. Birshtein and E. B. Zhulina. Scaling theory of supermolecular structures in block copolymer-solvent systems: 2. Supercrystalline structures. *Polymer*, 31(7):1312–1320, 1988. [Cited on page 44.]

[17] G. B. Blanchard, A. J. Kabla, N. L. Schultz, L. C. Butler, B. Sanson, N. Gorfinkiel, L. Mahadevan, and R. J. Adams. Tissue tectonics: Morphogenetic strain rates, cell shape change and intercalation. *Nature Methods*, 6(6):458–464, 2009. [Cited on page 7.]

[18] A. Boromand, A. Signoriello, J. Lowensohn, C. S. Orellana, E. R. Weeks, F. Ye, M. D. Shattuck, and C. S. O'Hern. The role of deformability in determining the structural and mechanical properties of bubbles and emulsions. *Soft Matter*, 15(29):5854–5865, 2019. [Cited on pages 36, 45, 47, 56, 61, and 86.]

[19] A. Boromand, A. Signoriello, F. Ye, C. S. O'Hern, and M. D. Shattuck. Jamming of Deformable Polygons. *Physical Review Letters*, 121(24):248003, 2018. [Cited on pages 36, 45, and 61.]

[20] N. Bourouina, J. Husson, F. Waharte, R. B. Pansu, and N. Henry. Formation of specific receptor-ligand bonds between liquid interfaces. *Soft Matter*, 7(19):9130–9139, 2011. [Cited on page 20.]

[21] D. Bray. Axonal growth in response to experimentally applied mechanical tension. *Developmental Biology*, 102(2):379–389, apr 1984. [Cited on page 72.]

[22] M. A. Breau, I. Bonnet, J. Stoufflet, J. Xie, S. De Castro, and S. Schneider-Maunoury. Extrinsic mechanical forces mediate retrograde axon extension in a developing neuronal circuit. *Nature Communications*, 8(1), 2017. [Cited on pages 74, 75, and 76.]

[23] G. W. Brodland. The Differential Interfacial Tension Hypothesis (DITH): A comprehensive theory for the self-rearrangement of embryonic cells and tissues. *Journal of Biomechanical Engineering*, 124(2):188–197, 2002. [Cited on page 12.]

[24] N. Brodu, J. A. Dijksman, and R. P. Behringer. Spanning the scales of granular materials through microscopic force imaging. *Nature Communications*, 6, 2015. [Cited on page 19.]

[25] J. Brujic. Experimental Study of Stress Transmission Through Particulate Matter. *Physica A*, (February), 2004. [Cited on page 26.]

[26] J. Brujic, S. F. Edwards, I. Hopkinson, and H. A. Makse. Measuring the distribution of interdroplet forces in a compressed emulsion system. *Physica A: Statistical Mechanics and its Applications*, 327(3-4):201–212, 2003. [Cited on page 50.]

[27] E. Calvo-Ochoa and C. A. Byrd-Jacobs. The Olfactory System of Zebrafish as a Model for the Study of Neurotoxicity and Injury: Implications for Neuroplasticity and Disease. *International Journal of Molecular Sciences*, 20(7), 2019. [Cited on page 73.]

[28] O. Campàs, T. Mammoto, S. Hasso, R. A. Sperling, D. O'Connell, A. G. Bischof, R. Maas, D. A. Weitz, L. Mahadevan, and D. E. Ingber. Quantifying cell-generated mechanical forces within living embryonic tissues. *Nature Methods*, 11(2):183–189, feb 2014. [Cited on pages 76, 77, and 89.]

[29] I. Cantat, S. Cohen-Addad, F. Elias, R. Hohler, O. Pitois, F. Rouyer, and A. Saint-Jalmes. *Foams: Structure and Dynamics*. Oxford University Press, 2018. [Cited on page 19.]

[30] M. E. Cates, J. P. Wittmer, J. P. Bouchaud, and P. Claudin. Jamming, force chains, and fragile matter. *Physical Review Letters*, 81(9):1841–1844, 1998. [Cited on page 50.]

[31] D. Chen, K. W. Desmond, and E. R. Weeks. Experimental observation of local rearrangements in dense quasi-two-dimensional emulsion flow. *Physical Review E - Statistical, Nonlinear, and Soft Matter Physics*, 91(6):1–9, 2015. [Cited on pages 36, 49, 50, 52, and 64.]

[32] D. Chen, D. Semwogerere, J. Sato, V. Breedveld, and E. R. Weeks. Microscopic structural relaxation in a sheared supercooled colloidal liquid. *Physical Review E - Statistical, Nonlinear, and Soft Matter Physics*, 81(1):1–13, 2010. [Cited on page 19.]

[33] Y. S. Chu, W. A. Thomas, O. Eder, F. Pincet, E. Perez, J. P. Thiery, and S. Dufour. Force measurements in E-cadherin-mediated cell doublets reveal rapid adhesion strengthened by actin cytoskeleton remodeling through Rac and Cdc42. *Journal of Cell Biology*, 167(6):1183–1194, 2004. [Cited on pages 8, 11, and 22.]

[34] P. Chugh, A. G. Clark, M. B. Smith, D. A. Cassani, K. Dierkes, A. Ragab, P. P. Roux, G. Charras, G. Salbreux, and E. K. Paluch. Actin cortex architecture regulates cell surface tension. *Nature Cell Biology*, 19(6):689–697, 2017. [Cited on page 8.]

[35] V. Conte, J. J. Muñoz, and M. Miodownik. A 3D finite element model of ventral furrow invagination in the Drosophila melanogaster embryo. *Journal of the Mechanical Behavior of Biomedical Materials*, 1(2):188–198, 2008. [Cited on page 6.]

[36] V. Conte, F. Ulrich, B. Baum, J. Muñoz, J. Veldhuis, W. Brodland, and M. Miodownik. A biomechanical analysis of ventral furrow formation in the Drosophila melanogaster embryo. *PloS one*, 7(4), 2012. [Cited on page 6.]

[37] S. S. Datta, D. D. Gerrard, T. S. Rhodes, T. G. Mason, and D. A. Weitz. Rheology of attractive emulsions. *Physical Review E - Statistical, Nonlinear, and Soft Matter Physics*, 84(4):3–8, 2011. [Cited on pages 44 and 47.]

[38] L. A. Davidson. Mechanical design in embryos: Mechanical signalling, robustness and developmental defects. *Philosophical Transactions of the Royal Society B: Biological Sciences*, 372(1720), 2017. [Cited on page 7.]

[39] K. W. Desmond, P. J. Young, D. Chen, and E. R. Weeks. Experimental study of forces between quasi-two-dimensional emulsion droplets near jamming. *Soft Matter*, 9(12):3424–3436, 2013. [Cited on page 45.]

[40] N. Desprat, W. Supatto, P. A. Pouille, E. Beaurepaire, and E. Farge. Tissue Deformation Modulates Twist Expression to Determine Anterior Midgut Differentiation in Drosophila Embryos. *Developmental Cell*, 15(3):470–477, 2008. [Cited on page 7.]

[41] S. Douezan and F. Brochard-Wyart. Dewetting of cellular monolayers. *European Physical Journal E*, 35(5):0–5, 2012. [Cited on page 18.]

[42] S. Douezan, K. Guevorkian, R. Naouar, S. Dufour, D. Cuvelier, and F. Brochard-Wyart. Spreading dynamics and wetting transition of cellular aggregates. *Proceedings of the National Academy of Sciences of the United States of America*, 108(18):7315–7320, 2011. [Cited on page 18.]

[43] M. Duda, N. J. Kirkland, N. Khalilgharibi, M. Tozluoglu, A. C. Yuen, N. Carpi, A. Bove, M. Piel, G. Charras, B. Baum, and Y. Mao. Polarization of Myosin II Refines Tissue Material Properties to Buffer Mechanical Stress. *Developmental Cell*, 48(2):245–260.e7, 2019. [Cited on page 18.]

[44] B. Dumat, L. Montel, L. Pinon, P. Matton, L. Cattiaux, J. Fattaccioli, and J. M. Mallet. Mannose-Coated Fluorescent Lipid Microparticles for Specific Cellular Targeting and Internalization via Glycoreceptor-Induced Phagocytosis. *ACS Applied Bio Materials*, 2(11):5118–5126, 2019. [Cited on page 20.]

[45] W. Engl, B. Arasi, L. L. Yap, J. P. Thiery, and V. Viasnoff. Actin dynamics modulate mechanosensitive immobilization of E-cadherin at adherens junctions. *Nature Cell Biology*, 16(6):584–591, 2014. [Cited on page 24.]

[46] G. Erdemci-Tandogan and M. L. Manning. Effect of cellular rearrangement time delays on the rheology of vertex models for confluent tissues. *bioRxiv*, 2021. [Cited on page 63.]

[47] M. L. Falk and J. S. Langer. Dynamics of viscoplastic deformation in amorphous solids. *Physical Review E*, 57(6):7192–7205, jun 1998. [Cited on page 60.]

[48] E. Farge. Mechanical Induction of Twist in the Drosophila Foregut/Stomodeal Primordium. *Current Biology*, 13(16):1365–1377, aug 2003. [Cited on page 7.]

[49] E. Farge. *Mechanotransduction in Development*, volume 95. Elsevier Inc., 1 edition, 2011. [Cited on page 7.]

[50] J. Fattaccioli, J. Baudry, N. Henry, F. Brochard-Wyart, and J. Bibette. Specific wetting probed with biomimetic emulsion droplets. *Soft Matter*, 4(12):2434–2440, 2008. [Cited on page 20.]

[51] L. Feng, L.-L. Pontani, R. Dreyfus, P. Chaikin, and J. Brujic. Specificity, flexibility and valence of DNA bonds guide emulsion architecture. *Soft Matter*, 9(41):9816–9823, 2013. [Cited on pages 20, 21, and 22.]

[52] G. Forgacs, R. A. Foty, Y. Shafrir, and M. S. Steinberg. Viscoelastic properties of living embryonic tissues: A quantitative study. *Biophysical Journal*, 74(5):2227–2234, 1998. [Cited on page 13.]

[53] R. A. Foty, G. Forgacs, C. M. Pfleger, and M. S. Steinberg. Liquid properties of embryonic tissues: Measurement of interfacial tensions. *Physical Review Letters*, 72(14):2298–2301, apr 1994. [Cited on pages 13 and 89.]

[54] R. A. Foty, C. M. Pfleger, G. Forgacs, and M. S. Steinberg. Surface tensions of embryonic tissues predict their mutual envelopment behavior. *Development*, 122(5):1611–1620, 1996. [Cited on page 13.]

[55] R. A. Foty and M. S. Steinberg. Cadherin-mediated cell-cell adhesion and tissue segregation in relation to malignancy. *International Journal of Developmental Biology*, 48(5-6):397–409, 2004. [Cited on page 12.]

[56] R. A. Foty and M. S. Steinberg. The differential adhesion hypothesis: A direct evaluation. *Developmental Biology*, 278(1):255–263, 2005. [Cited on page 12.]

[57] C. Frantz, K. M. Stewart, and V. M. Weaver. The extracellular matrix at a glance. *Journal of Cell Science*, 123(24):4195–4200, 2010. [Cited on page 9.]

[58] Y. Gai, C. M. Leong, W. Cai, and S. K. Tang. Spatiotemporal periodicity of dislocation dynamics in a two-dimensional microfluidic crystal flowing in a tapered channel. *Proceedings of the National Academy of Sciences of the United States of America*, 113(43):12082–12087, 2016. [Cited on pages 52, 53, and 62.]

[59] B. Gallois and R. Candelier. FastTrack: an open-source software for tracking varying numbers of deformable objects. *arXiv*, pages 1–29, 2020. [Cited on page 35.]

[60] G. Gangatharan, S. Schneider-Maunoury, and M. A. Breau. Role of mechanical cues in shaping neuronal morphology and connectivity. *Biology of the Cell*, 110(6):125–136, 2018. [Cited on pages 71, 72, 73, and 75.]

[61] C. Garcin and A. Straube. Microtubules in cell migration. *Essays in Biochemistry*, 63(5):509–520, oct 2019. [Cited on page 8.]

[62] J. A. Glazier and F. Graner. Simulation of the differential adhesion driven rearrangement of biological cells. *Physical Review E*, 47(3):2128–2154, 1993. [Cited on page 12.]

[63] I. Golovkova, L. Montel, F. Pan, E. Wandersman, A. M. Prevost, T. Bertrand, and L.-L. Pontani. Adhesion as a trigger of droplet polarization in flowing emulsions. *Soft Matter*, 1:1–285, 2021. [Cited on page 61.]

[64] D. Gonzalez-Rodriguez, K. Guevorkian, S. Douezan, and F. Brochard-Wyart. Soft matter models of developing tissues and tumors. *Science*, 338(6109):910–917, 2012. [Cited on pages 11, 13, 14, 18, 19, and 89.]

[65] K. Guevorkian, M.-J. Colbert, M. Durth, S. Dufour, and F. m. ç. Brochard-Wyart. Aspiration of Biological Viscoelastic Drops. *Phys. Rev. Lett.*, 104(21):218101, may 2010. [Cited on page 13.]

[66] B. Gumbiner and K. Simons. A functional assay for proteins involved in establishing and epithelial occluding barrier: Identification of a uvomorulin-like polypeptide. *Journal of Cell Biology*, 102(2):457–468, 1986. [Cited on page 9.]

[67] M. Hadorn, E. Boenzli, K. T. Sørensen, H. Fellermann, P. E. Hotz, and M. M. Hanczyc. Specific and reversible DNA-directed self-assembly of oil-in-water emulsion droplets. *Proceedings of the National Academy of Sciences of the United States of America*, 109(50):20320–20325, 2012. [Cited on page 21.]

[68] J. M. Halbleib and W. J. Nelson. Cadherins in development: Cell adhesion, sorting, and tissue morphogenesis. *Genes and Development*, 20(23):3199–3214, 2006. [Cited on pages 8 and 9.]

[69] A. Hartsock and W. J. Nelson. Adherens and tight junctions: Structure, function and connections to the actin cytoskeleton. *Biochimica et Biophysica Acta - Biomembranes*, 1778(3):660–669, 2008. [Cited on page 22.]

[70] T. Hayashi and R. W. Carthew. Surface mechanics mediate pattern formation in the developing retina. *Nature*, 431(7009):647–652, 2004. [Cited on page 18.]

[71] J. Heasman, D. Ginsberg, B. Geiger, K. Goldstone, T. Pratt, C. Yoshida-Noro, and C. Wylie. A functional test for maternally inherited cadherin in Xenopus shows its importance in cell adhesion at the blastula stage. *Development*, 120(1):49–57, 1994. [Cited on page 9.]

[72] N. C. Heer and A. C. Martin. Tension, contraction and tissue morphogenesis. *Development (Cambridge)*, 144(23):4249–4260, 2017. [Cited on page 68.]

[73] C. P. Heisenberg and Y. Bellaïche. XForces in tissue morphogenesis and patterning. *Cell*, 153(5):948, 2013. [Cited on page 7.]

[74] S. Henkes, Y. Fily, and M. C. Marchetti. Active jamming: Self-propelled soft particles at high density. *Physical Review E - Statistical, Nonlinear, and Soft Matter Physics*, 84(4):84–87, 2011. [Cited on page 17.]

[75] S. Herculano-Houzel. The human brain in numbers: A linearly scaled-up primate brain. *Frontiers in Human Neuroscience*, 3(NOV):1–11, 2009. [Cited on page 71.]

[76] S. Hilgenfeldt, S. Erisken, and R. W. Carthew. Physical modeling of cell geometric order in an epithelial tissue. *Proceedings of the National Academy of Sciences of the United States of America*, 105(3):907–911, 2008. [Cited on page 19.]

[77] A. Huang, X. Zhang, R. Li, and Y. Chi. *Memristor Neural Network Design*. InTech, apr 2018. [Cited on page 71.]

[78] O. Ilina, P. G. Gritsenko, S. Syga, J. Lippoldt, C. A. La Porta, O. Chepizhko, S. Grosser, M. Vullings, G. J. Bakker, J. Starruß, P. Bult, S. Zapperi, J. A. Käs, A. Deutsch, and P. Friedl. Cell–cell adhesion and 3D matrix confinement determine jamming transitions in breast cancer invasion. *Nature Cell Biology*, 22(9):1103–1115, 2020. [Cited on page 18.]

[79] T. Iskratsch, H. Wolfenson, and M. P. Sheetz. Appreciating force and shape-the rise of mechanotransduction in cell biology. *Nature Reviews Molecular Cell Biology*, 15(12):825–833, 2014. [Cited on page 7.]

[80] C. Jamora and E. Fuchs. Intercellular adhesion, signalling and the cytoskeleton. *Nature Cell Biology*, 4(4):101–108, 2002. [Cited on page 10.]

[81] M. E. Janik, D. Hoja-Lukowicz, and M. Przybylo. Cadherins and their Role in Malignant Transformation: Implications for Skin Cancer Progression. In M. Blumenberg, editor, *Human Skin Cancer, Potential Biomarkers and Therapeutic Targets*, chapter 5. InTech, Rijeka, oct 2016. [Cited on page 9.]

[82] I. Jorjadze, L.-L. Pontani, and J. Brujic. Microscopic approach to the nonlinear elasticity of compressed emulsions. *Physical Review Letters*, 110(4):1–5, 2013. [Cited on page 19.]

[83] I. Jorjadze, L.-L. Pontani, K. A. Newhall, and J. Brujic. Attractive emulsion droplets probe the phase diagram of jammed granular matter. *Proceedings of the National Academy of Sciences of the United States of America*, 108(11):4286–4291, 2011. [Cited on pages 23, 44, 45, and 47.]

[84] S. M. Joscelyne and G. Trägårdh. Membrane emulsification - A literature review. *Journal of Membrane Science*, 169(1):107–117, 2000. [Cited on page 26.]

[85] A. Kabla, J. Scheibert, and G. Debregeas. Quasi-static rheology of foams. Part 2. Continuous shear flow. *Journal of Fluid Mechanics*, 587:45–72, 2007. [Cited on page 19.]

[86] N. G. Kan, M. P. Stemmler, D. Junghans, B. Kanzler, W. N. de Vries, M. Dominis, and R. Kemler. Gene replacement reveals a specific role for E-cadherin in the formation of a functional trophectoderm. *Development*, 134(1):31–41, 2007. [Cited on page 9.]

[87] G. Katgert and M. Van Hecke. Jamming and geometry of two-dimensional foams. *Epl*, 92(3), 2010. [Cited on page 45.]

[88] P. Katsamba, K. Carroll, G. Ahlsen, F. Bahna, J. Vendome, S. Posy, M. Rajebhosale, S. Price, T. M. Jessell, A. Ben-Shaul, L. Shapiro, and B. H. Honig. Linking molecular affinity and cellular specificity in cadherin-mediated adhesion. *Proceedings of the National Academy of Sciences of the United States of America*, 106(28):11594–11599, 2009. [Cited on page 8.]

[89] T. Kawakatsu, G. Trägårdh, Y. Kikuchi, M. Nakajima, H. Komori, and T. Yonemoto. Effect of microchannel structure on droplet size during crossflow microchannel emulsification. *Journal of Surfactants and Detergents*, 3(3):295–302, 2000. [Cited on page 26.]

[90] H. Khan, J. M. Seddon, R. V. Law, N. J. Brooks, E. Robles, J. T. Cabral, and O. Ces. Effect of glycerol with sodium chloride on the Krafft point of sodium dodecyl sulfate using surface tension. *Journal of Colloid and Interface Science*, 538:75–82, 2019. [Cited on page 44.]

[91] H. Khan, J. M. Seddon, R. V. Law, N. J. Brooks, E. Robles, J. T. Cabral, and O. Ces. Effect of glycerol with sodium chloride on the Krafft point of sodium dodecyl sulfate using surface tension. *Journal of Colloid and Interface Science*, 538:75–82, 2019. [Cited on page 44.]

[92] S. Kim, M. Pochitaloff, G. Stooke-Vaughan, and O. Campàs. Embryonic tissues as active foams. *bioRxiv*, pages 1–33, 2020. [Cited on page 17.]

[93] G. H. Koenderink, Z. Dogic, F. Nakamura, P. M. Bendix, F. C. MacKintosh, J. H. Hartwig, T. P. Stossel, and D. A. Weitz. An active biopolymer network controlled by molecular motors. *Proceedings of the National Academy of Sciences of the United States of America*, 106(36):15192–15197, 2009. [Cited on page 18.]

[94] A. L. Kolodkin and M. Tessier-Lavigne. Mechanisms and Molecules of Neuronal Wiring: A Primer. *Cold Spring Harbor Perspectives in Biology*, 3(6):a001727–a001727, jun 2011. [Cited on page 72.]

[95] D. E. Koser, A. J. Thompson, S. K. Foster, A. Dwivedy, E. K. Pillai, G. K. Sheridan, H. Svoboda, M. Viana, L. D. F. Costa, J. Guck, C. E. Holt, and K. Franze. Mechanosensing is critical for axon growth in the developing brain. *Nature Neuroscience*, 19(12):1592–1598, 2016. [Cited on page 73.]

[96] M. Krieg, Y. Arboleda-Estudillo, P. H. Puech, J. Käfer, F. Graner, D. J. Müller, and C. P. Heisenberg. Tensile forces govern germ-layer organization in zebrafish. *Nature Cell Biology*, 10(4):429–436, 2008. [Cited on pages 7 and 12.]

[97] M. Krieg, G. Fläschner, D. Alsteens, B. M. Gaub, W. H. Roos, G. J. L. Wuite, H. E. Gaub, C. Gerber, Y. F. Dufrêne, and D. J. Müller. Atomic force microscopy-based mechanobiology. *Nature Reviews Physics*, 1(1):41–57, jan 2019. [Cited on page 13.]

[98] E. Kutejova, J. Briscoe, and A. Kicheva. Temporal dynamics of patterning by morphogen gradients. *Current Opinion in Genetics and Development*, 19(4):315–322, 2009. [Cited on page 6.]

[99] P. Lamoureux, S. R. Heidemann, N. R. Martzke, and K. E. Miller. Growth and elongation within and along the axon. *Developmental Neurobiology*, 70(3):135–149, 2010. [Cited on page 72.]

[100] E. Lawson-Keister and M. L. Manning. Jamming and arrest of cell motion in biological tissues. *arXiv*, feb 2021. [Cited on pages 15 and 18.]

[101] A. Le Bouil, A. Amon, S. McNamara, and J. Crassous. Emergence of cooperativity in plasticity of soft glassy materials. *Physical Review Letters*, 112(24):1–5, 2014. [Cited on page 59.]

[102] T. Lecuit and P. F. Lenne. Cell surface mechanics and the control of cell shape, tissue patterns and morphogenesis. *Nature Reviews Molecular Cell Biology*, 8(8):633–644, 2007. [Cited on pages 9 and 11.]

[103] F. T. Lewis. The correlation between cell division and the shapes and sizes of prismatic cells in the epidermis of cucumis. *The Anatomical Record*, 38(3):341–376, may 1928. [Cited on page 19.]

[104] H. Lodish, A. Berk, P. Matsudaria, C. A. Kaiser, M. Krieger, M. P. Scott, L. Zipursky, and J. Darnell. *Molecular Cell Biology*. W.H. Freeman and Company, 5 edition, 2003. [Cited on page 28.]

[105] L. A. Lowery and D. V. Vactor. The trip of the tip: understanding the growth cone machinery. *Nature Reviews Molecular Cell Biology*, 10(5):332–343, may 2009. [Cited on page 72.]

[106] J. L. Maître, H. Berthoumieux, S. F. G. Krens, G. Salbreux, F. Jülicher, E. Paluch, and C. P. Heisenberg. Adhesion functions in cell sorting by mechanically coupling the cortices of adhering cells. *Science*, 338(6104):253–256, 2012. [Cited on page 24.]

[107] J. L. Maître and C. P. Heisenberg. Three functions of cadherins in cell adhesion. *Current Biology*, 23(14):R626–R633, 2013. [Cited on page 18.]

[108] C. E. Maloney and A. Lemaître. Amorphous systems in athermal, quasistatic shear. *Physical Review E - Statistical, Nonlinear, and Soft Matter Physics*, 74(1):1–22, 2006. [Cited on page 60.]

[109] T. Mammoto, A. Mammoto, and D. E. Ingber. Mechanobiology and developmental control. *Annual Review of Cell and Developmental Biology*, 29:27–61, 2013. [Cited on page 7.]

[110] M. L. Manning, R. A. Foty, M. S. Steinberg, and E. M. Schoetz. Coaction of intercellular adhesion and cortical tension specifies tissue surface tension. *Proceedings of the National Academy of Sciences of the United States of America*, 107(28):12517–12522, 2010. [Cited on page 12.]

[111] P. Marmottant, A. Mgharbel, J. Käfer, B. Audren, J. P. Rieu, J. C. Vial, B. Van Der Sanden, A. F. Marée, F. Graner, and H. Delanoë-Ayari. The role of fluctuations and stress on the effective viscosity of cell aggregates (Proceedings of the National Academy of Sciences of the United States of America (2009) 106, (17271-17275) DOI: 10.1073/pnas.0902085106). *Proceedings of the National Academy of Sciences of the United States of America*, 106(45):19204, 2009. [Cited on pages 13 and 17.]

[112] A. C. Martin. Self-organized cytoskeletal alignment during Drosophila mesoderm invagination . *Philosophical Transactions of the Royal Society B: Biological Sciences*, 375(1809):20190551, 2020. [Cited on page 68.]

[113] T. G. Mason, J. Bibette, and D. A. Weitz. Elasticity of Compressed Emulsions. *Physical Review Letters*, 75(10):2051–2054, sep 1995. [Cited on page 44.]

[114] T. G. Mason, A. Krall, J. Bibette, H. Gang, and D. A. Weitz. Encyclopedia of Emulsion Technology: Volume 4. P, Becher, Ed. Marcel Dekker, Inc., New York, 1996. *Journal of Dispersion Science and Technology*, 18(4):459–460, jun 1997. [Cited on page 44.]

[115] J. C. Maxwell. XLV. On reciprocal figures and diagrams of forces. *The London, Edinburgh, and Dublin Philosophical Magazine and Journal of Science*, 27(182):250–261, apr 1864. [Cited on page 16.]

[116] R. M. Mège, J. Gavard, and M. Lambert. Regulation of cell-cell junctions by the cytoskeleton. *Current Opinion in Cell Biology*, 18(5):541–548, 2006. [Cited on page 8.]

[117] R. M. Mège and N. Ishiyama. Integration of cadherin adhesion and cytoskeleton at adherens junctions. *Cold Spring Harbor Perspectives in Biology*, 9(5), 2017. [Cited on page 8.]

[118] H. Meinhardt. Models for the generation and interpretation of gradients. *Cold Spring Harbor perspectives in biology*, 1(4), 2009. [Cited on page 6.]

[119] M. Merkel and M. L. Manning. A geometrically controlled rigidity transition in a model for confluent 3D tissues. *arXiv*, 2017. [Cited on page 16.]

[120] S. Meunier and I. Vernos. Microtubule assembly during mitosis - from distinct origins to distinct functions? *Journal of Cell Science*, 125(12):2805–2814, 2012. [Cited on page 8.]

[121] A. Mgharbel, H. Delanoë-Ayari, and J. P. Rieu. Measuring accurately liquid and tissue surface tension with a compression plate tensiometer. *HFSP Journal*, 3(3):213–221, 2009. [Cited on page 13.]

[122] C. T. Mierke. Initiation of a neoplasm or tumor. In *Physics of Cancer, Volume 1: Interplay between tumor biology, inflammation and cell mechanics*. IOP Publishing, 2018. [Cited on page 17.]

[123] M.-C. Miguel, A. Vespignani, S. Zapperi, J. Weiss, and J.-R. Grasso. Intermittent dislocation flow in viscoplastic deformation. *Nature*, 410(6829):667–671, apr 2001. [Cited on page 59.]

[124] N. Miyasaka, A. A. Wanner, J. Li, J. Mack-Bucher, C. Genoud, Y. Yoshihara, and R. W. Friedrich. Functional development of the olfactory system in zebrafish. *Mechanisms of Development*, 130(6-8):336–346, 2013. [Cited on page 74.]

[125] D. Molino, S. Quignard, C. Gruget, F. Pincet, Y. Chen, M. Piel, and J. Fattaccioli. On-chip quantitative measurement of mechanical stresses during cell migration with emulsion droplets. *Scientific Reports*, 6:1–11, 2016. [Cited on page 20.]

[126] O. Mondain-Monval, F. Leal-Calderon, J. Phillip, and J. Bibette. Depletion forces in the presence of electrostatic double layer repulsion. *Physical Review Letters*, 75(18):3364–3367, 1995. [Cited on page 28.]

[127] A. Mongera, P. Rowghanian, H. J. Gustafson, E. Shelton, D. A. Kealhofer, E. K. Carn, F. Serwane, A. A. Lucio, J. Giammona, and O. Campàs. A fluid-to-solid jamming transition underlies vertebrate body axis elongation. *Nature*, 561(7723):401–405, 2018. [Cited on pages 18, 20, 66, 76, 77, 78, 79, 80, 89, and 90.]

[128] W. J. Nelson, D. J. Dickinson, and W. I. Weis. *Roles of cadherins and catenins in cell-cell adhesion and epithelial cell polarity*, volume 116. Elsevier Inc., 1 edition, 2013. [Cited on page 8.]

[129] K. A. Newhall, L.-L. Pontani, I. Jorjadze, S. Hilgenfeldt, and J. Brujic. Size-topology relations in packings of grains, emulsions, foams, and biological cells. *Physical Review Letters*, 108(26), 2012. [Cited on pages 19 and 57.]

[130] D. H. Oh, P. Balakrishnan, Y. K. Oh, D. D. Kim, C. S. Yong, and H. G. Choi. Effect of process parameters on nanoemulsion droplet size and distribution in SPG membrane emulsification. *International Journal of Pharmaceutics*, 404(1-2):191–197, 2011. [Cited on page 28.]

[131] C. S. O'Hern, L. E. Silbert, A. J. Liu, and S. R. Nagel. Jamming at zero temperature and zero applied stress: The epitome of disorder. *Physical Review E - Statistical Physics, Plasmas, Fluids, and Related Interdisciplinary Topics*, 68(1):19, 2003. [Cited on page 15.]

[132] P. Panorchan, M. S. Thompson, K. J. Davis, Y. Tseng, K. Konstantopoulos, and D. Wirtz. Single-molecule analysis of cadherin-mediated cell-cell adhesion. *Journal of Cell Science*, 119(1):66–74, 2006. [Cited on page 21.]

[133] J.-A. Park, J. H. Kim, D. Bi, J. A. Mitchel, N. T. Qazvini, K. Tantisira, C. Y. Park, M. McGill, S.-h. Kim, B. Gweon, J. Notbohm, R. Steward Jr, S. Burger, S. H. Randell, A. T. Kho, D. T. Tambe, C. Hardin, S. A. Shore, E. Israel, D. A. Weitz, D. J. Tschumperlin, E. P. Henske, S. T. Weiss, M. L. Manning, J. P. Butler, J. M. Drazen, and J. J. Fredberg. Unjamming and cell shape in the asthmatic airway epithelium. *Nature Materials*, 14(10):1040–1048, oct 2015. [Cited on page 16.]

[134] H. M. Phillips and M. S. Steinberg. Equilibrium measurements of embryonic chick cell adhesiveness. I. Shape equilibrium in centrifugal fields. *Proceedings of the National Academy of Sciences of the United States of America*, 64(1):121–127, 1969. [Cited on page 13.]

[135] H. M. Phillips and M. S. Steinberg. Embryonic tissues as elasticoviscous liquids. I. Rapid and slow shape changes in centrifuged cell aggregates. *Journal of Cell Science*, Vol. 30:1–20, 1978. [Cited on page 19.]

[136] L. Pinon. Functionalized emulsion droplets and microfluidic traps to study B cell polarization and mechanics. *PhD manuscript*, 2021. [Cited on page 20.]

[137] L. Pinon, L. Montel, O. Mesdjian, M. Bernard, A. Michel, C. Ménager, and J. Fattaccioli. Kinetically Enhanced Fabrication of Homogeneous Biomimetic and Functional Emulsion Droplets. *Langmuir*, 34(50):15319–15326, 2018. [Cited on page 28.]

[138] W. J. Polacheck and C. S. Chen. Measuring cell-generated forces: A guide to the available tools. *Nature Methods*, 13(5):415–423, 2016. [Cited on page 13.]

[139] L.-L. Pontani, M. F. Haase, I. Raczkowska, and J. Brujic. Immiscible lipids control the morphology of patchy emulsions. *Soft Matter*, 9(29):7150–7157, 2013. [Cited on page 22.]

[140] L.-L. Pontani, I. Jorjadze, and J. Brujic. Cis and Trans Cooperativity of E-Cadherin Mediates Adhesion in Biomimetic Lipid Droplets. *Biophysical Journal*, 110(2):391–399, 2016. [Cited on pages 20, 21, and 23.]

[141] L.-L. Pontani, I. Jorjadze, V. Viasnoff, and J. Brujic. Biomimetic emulsions reveal the effect of mechanical forces on cell-cell adhesion. *Proceedings of the National Academy of Sciences of the United States of America*, 109(25):9839–9844, 2012. [Cited on pages 18, 20, 21, 22, 23, 27, 29, and 58.]

[142] V. Ravaine, J. Bibette, and N. Henry. Wetting of liquid droplets on living cells. *Journal of Colloid and Interface Science*, 255(2):270–273, 2002. [Cited on page 20.]

[143] R. Rens, M. Vahabi, A. J. Licup, F. C. MacKintosh, and A. Sharma. Nonlinear mechanics of athermal branched biopolymer networks. *Journal of Physical Chemistry B*, 120(26):5831–5841, 2016. [Cited on page 18.]

[144] P. Roca-Cusachs, V. Conte, and X. Trepat. Quantifying forces in cell biology. *Nature Cell Biology*, 19(7):742–751, jul 2017. [Cited on page 13.]

[145] C. C. Ruiz, L. Díaz-López, and J. Aguiar. Micellization of sodium dodecyl sulfate in glycerol aqueous mixtures. *Journal of Dispersion Science and Technology*, 29(2):266–273, 2008. [Cited on page 44.]

[146] M. Sadati, N. Taheri Qazvini, R. Krishnan, C. Y. Park, and J. J. Fredberg. Collective migration and cell jamming. *Differentiation*, 86(3):121–125, 2013. [Cited on page 15.]

[147] P. Sahu, D. M. Sussman, M. Rübsam, A. F. Mertz, V. Horsley, E. R. Dufresne, C. M. Niessen, M. C. Marchetti, M. L. Manning, and J. M. Schwarz. Small-scale demixing in confluent biological tissues. *Soft Matter*, 16(13):3325–3337, 2020. [Cited on page 18.]

[148] P. Schall, D. A. Weitz, and F. Spaepen. Structural rearrangements that govern flow in colloidal glasses. *Science*, 318(5858):1895–1899, 2007. [Cited on page 19.]

[149] O. Schmalhofer, S. Brabletz, and T. Brabletz. E-cadherin, β-catenin, and ZEB1 in malignant progression of cancer. *Cancer and Metastasis Reviews*, 28(1-2):151–166, 2009. [Cited on page 9.]

[150] R. Schmidt, U. Strähle, and S. Scholpp. Neurogenesis in zebrafish - from embryo to adult. *Neural Development*, 8(1):1–13, 2013. [Cited on page 73.]

[151] E. M. Schötz, R. D. Burdine, F. Jülicher, M. S. Steinberg, C. P. Heisenberg, and R. A. Foty. Quantitative differences in tissue surface tension influence zebrafish germ layer positioning. *HFSP Journal*, 2(1):42–56, 2008. [Cited on pages 11, 12, and 14.]

[152] M. S. Steinberg. Does differential adhesion govern self-assembly processes in histogenesis? Equilibrium configurations and the emergence of a hierarchy among populations of embryonic cells. *Journal of Experimental Zoology*, 173(4):395–433, 1970. [Cited on page 12.]

[153] T. V. Stirbat, A. Mgharbel, S. Bodennec, K. Ferri, H. C. Mertani, J. P. Rieu, and H. Delanoë-Ayari. Fine Tuning of Tissues' Viscosity and Surface Tension through Contractility Suggests a New Role for α-Catenin. *PLoS ONE*, 8(2), 2013. [Cited on pages 12 and 13.]

[154] E. T. Stoeckli. Understanding axon guidance: Are we nearly there yet? *Development (Cambridge)*, 145(10), 2018. [Cited on page 72.]

[155] C. Storm, J. J. Pastore, F. C. MacKintosh, T. C. Lubensky, and P. A. Janmey. Nonlinear elasticity in biological gels. *Nature*, 435(7039):191–194, 2005. [Cited on page 18.]

[156] T. Strunz, K. Oroszlan, R. Schäfer, and H. J. Güntherodt. Dynamic force spectroscopy of single DNA molecules. *Proceedings of the National Academy of Sciences of the United States of America*, 96(20):11277–11282, 1999. [Cited on page 62.]

[157] K. Sugimura, P. F. Lenne, and F. Graner. Measuring forces and stresses in situ in living tissues. *Development (Cambridge)*, 143(2):186–196, 2016. [Cited on page 13.]

[158] M. Tada and C. P. Heisenberg. Convergent extension: Using collective cell migration and cell intercalation to shape embryos. *Development (Cambridge)*, 139(21):3897–3904, 2012. [Cited on page 6.]

[159] Takeichi Masatoshi. The cadherins: Cell-cell adhesion molecules controlling animal morphogenesis. *Development*, 102(4):639–655, 1988. [Cited on page 9.]

[160] R. J. Tetley and Y. Mao. The same but different: Cell intercalation as a driver of tissue deformation and fluidity. *Philosophical Transactions of the Royal Society B: Biological Sciences*, 373(1759), 2018. [Cited on page 16.]

[161] J. P. Thiery, W. Engl, V. Viasnoff, and S. Dufour. Biochemical and biophysical origins of cadherin selectivity and adhesion strength. *Current Opinion in Cell Biology*, 24(5):614–619, 2012. [Cited on page 8.]

[162] S. Tlili, J. Yin, J. F. Rupprecht, M. A. Mendieta-Serrano, G. Weissbart, N. Verma, X. Teng, Y. Toyama, J. Prost, and T. E. Saunders. Shaping the zebrafish myotome by intertissue friction and active stress. *Proceedings of the National Academy of Sciences of the United States of America*, 116(51):25430–25439, 2019. [Cited on page 10.]

[163] P. L. Townes and J. Holtfreter. Directed movements and selective adhesion of embryonic amphibian cells. *Journal of Experimental Zoology*, 128(1):53–120, feb 1955. [Cited on page 11.]

[164] V. Trappe, V. Prasad, L. Cipelletti, P. N. Segre, and D. A. Weitz. Jamming phase diagram for attractive particles. *Nature*, 411(6839):772–775, 2001. [Cited on page 17.]

[165] S. A. Van Der Meulen, G. Helms, and M. Dogterom. Solid colloids with surface-mobile linkers. *Journal of Physics Condensed Matter*, 27(23), 2015. [Cited on page 21.]

[166] X. Wang, M. Merkel, L. B. Sutter, G. Erdemci-Tandogan, M. L. Manning, and K. E. Kasza. Anisotropy links cell shapes to tissue flow during convergent extension. *Proceedings of the National Academy of Sciences of the United States of America*, 117(24):13541–13551, 2020. [Cited on pages 16, 18, 66, and 68.]

[167] O. Wartlick, A. Kicheva, and M. González-Gaitán. Morphogen gradient formation. *Cold Spring Harbor perspectives in biology*, 1(3):1–22, 2009. [Cited on page 6.]

[168] C. Wiebe and G. W. Brodland. Tensile properties of embryonic epithelia measured using a novel instrument. *Journal of Biomechanics*, 38(10):2087–2094, 2005. [Cited on page 13.]

[169] S. Yamada and W. J. Nelson. Localized zones of Rho and Rac activities drive initiation and expansion of epithelial cell-cell adhesion. *Journal of Cell Biology*, 178(3):517–527, 2007. [Cited on page 18.]

[170] L. Yan and D. Bi. Multicellular Rosettes Drive Fluid-solid Transition in Epithelial Tissues. *Physical Review X*, 9(1):11029, 2019. [Cited on page 16.]

[171] C. Yuan, A. Chen, P. Kolb, and V. T. Moy. Energy landscape of streptavidin-biotin complexes measured by atomic force microscopy. *Biochemistry*, 39(33):10219–10223, 2000. [Cited on page 21.]

[172] M. Zaiser. Scale invariance in plastic flow of crystalline solids. *Advances in Physics*, 55(1-2):185–245, 2006. [Cited on pages 59 and 62.]

[173] J. A. Zallen and E. Wieschaus. Patterned Gene Expression Directs Bipolar Planar Polarity in Drosophila that eliminate dorsal or ventral cell types (Irvine and Wieschaus, 1994). Instead, the patterning of cell fates along the A-P axis, perpendicular to the direction of cell. *Developmental Cell*, 6:343–355, 2004. [Cited on page 18.]

[174] H. Zhang and M. Labouesse. Signalling through mechanical inputs - a coordinated process. *Journal of Cell Science*, 125(17):4172–4172, 2012. [Cited on page 7.]

[175] L. Zhang, S. Cai, Z. Hu, and J. Zhang. A comparison between bridges and force-chains in photoelastic disk packing. *Soft Matter*, 10(1):109–114, 2014. [Cited on page 50.]

[176] Y. Zhang, A. McMullen, L.-L. Pontani, X. He, R. Sha, N. C. Seeman, J. Brujic, and P. M. Chaikin. Sequential self-assembly of DNA functionalized droplets. *Nature Communications*, 8(1):1–7, 2017. [Cited on page 21.]